Relativistic Many-Electron Calculations for $L_{2,3}$ X-ray Absorption Spectra of $3d$ Transition Metal Compounds

(3d 遷移金属化合物における $L_{2,3}$ X 線吸収スペクトルの相対論多電子計算)

Hidekazu Ikeno

池野 豪一

2007

Relativistic Many-Electron Calculations for $L_{2,3}$ X-ray Absorption Spectra of $3d$ Transition Metal Compounds

($3d$ 遷移金属化合物における $L_{2,3}$ X線吸収スペクトルの相対論多電子計算)

Hidekazu Ikeno

池野 豪一

2007

Contents

Chapter 1

General Introduction

In this thesis, a new theoretical approach for the analysis of the multiplet structure appears in x-ray absorption spectra (XAS) will be introduced. we focused on the NEXAFS (near edge x-ray absorption fine structure) region at $L_{2,3}$-edge of $3d$ transition metal (TM) compounds, which corresponds to the excitation of core $2p$ electron to unoccupied $3d$ levels. The purpose of this thesis is to establish a new theoretical method to analyze $3d$ TM $L_{2,3}$-edge NEXAFS spectra of a variety kind of advanced materials which has reliable predictive power and less ambiguity, and apply that method to analysis of TM $L_{2,3}$-edge NEXAFS in advanced materials. In this chapter, we briefly discuss the x-ray absorption process, and describe the importance of purpose and the background of this work.

X-ray absorption spectroscopy is a powerful technique for the characterization of certain atoms in materials and has widely used in the materials science[1, 2]. The most important feature of this technique is that one obtains element specific information, since it measures the excitation of a core electron of selected element. In x-ray absorption process, a core electron interact with a photon and is excited into unoccupied state. Hence a x-ray absorption spectrum (XAS) reflects the electronic structure of unoccupied state, which is sensitive to the local environment of selected element.

The oscillatory structure in the x-ray absorption spectrum just above an x-ray absorption edge is called XAFS (x-ray absorption near edge structure). A XAFS spectrum can be divided into two part. NEXAFS (near edge x-ray absorption fine structure) corresponds to the first 30-50 eV region from absorption edge. XANES (x-ray absorption near edge structure) is a synonym of NEXAFS.

Rest of spectrum is called EXAFS (extended x-ray absorption fine structure). In NEXAFS region can be ascribed to the electron transition to bounded state, hence is sensitive to chemical environment of selected element such as charge states, chemical bonding, spin state etc[3, 4]. On the other hand, the excited electrons has large kinetic energy in EXAFS region and moves around inside a material. Therefore it can reveal the local coordination of specific element such as coordination number and bond length quantitatively. XAFS can be applied not only to crystalline sample, but also nano-crystalline, amorphous material or liquid samples. Recent development of third generation synchrotron source enables NEXAFS measurement of small amount of elements in samples, such as ultra dilute dopants/segregants, ultra thin films, surface adsorbants, etc[5–7]. In order to extract the information about local environment of probe atoms in such materials, reliable theoretical tools which have predictive performance and free from adjustable parameters are indispensable.

There have been two different kinds of approaches used to compute NEXAFS theoretically. One is called the multiple scattering approach, which basically computes the scattering phenomena of the excited electron associated with the x-ray absorption. This approach is a standard technique to analyze EXAFS[8–10]. The other approach is a density functional calculation under periodic boundary condition. Most of K-edge NEXAFS, which is ascribed to the electric-dipole transition from $1s$ to unoccupied np orbitals, can be well reproduced by using a reliable band structure calculation and a large supercell with inclusion of a core-hole[11–13].

In $3d$ TM $L_{2,3}$-edge NEXAFS, one-electron approximation breaks down. Sharp peaks at the thresholds of L_3-edge and L_2-edge NEXAFS of $3d$ transition metals are attributed to electric-dipole transitions from the $2p_{3/2}$ and $2p_{1/2}$ core states to the unoccupied $3d$ levels. Within the one-electron approximation, the final states in both edges have equivalent shape and their intensity ratio (branching ratio) should follow the statistical value 2:1 expected from the ratio of the initial states. It is sometimes misunderstood that the $L_{2,3}$-edge NEXAFS of $3d$ transition-metal compounds can be obtained simply by overlaying the spectrum by the one electron calculations with proper L_3-L_2 splitting and L_3/L_2 intensity ratio. However, the observed branching ratio is generally far from this ideal value, and the spectral shapes of L_3-edge and L_2-edge are completely different, which are mainly due to the strong correlations among the $2p$ core hole and the $3d$ electrons[14, 15]. That can be rephrased in the terminology of atomic physics as "multiplet effects".

Multiplet structures of isolated atoms were well studied both by experiment and theory[16]. Crystal field effects and contribution of the ligand orbitals as a result of covalent bonding have been parametrized to compute the multiplet structures of many transition-metal compounds. Impurity Anderson model[17] and crystal field atomic multiplet program[18–21] are typical examples. Although they have been successful in reproducing experimental spectra, they use a number of adjustable parameters. The number of parameters increases significantly when the TM ion is located in a low symmetry site. It has little predictive performance of the multiplet structures *a priori*. A first principles calculation beyond one-electron approximation to take account many-electron interactions is therefore desirable. In order to treat the electronic transition from a core orbital, relativistic effects should also be considered.

A new method to perform such many-electron calculations in the first principles manner has been developed in present author's group[22]. First principles molecular orbital calculations were made using model clusters. Electronic correlations among $2p$ and $3d$ electrons were rigorously calculated by taking Slater determinants of all electronic configurations made by these molecular orbitals. In the quantum chemistry terminology, this is the "configuration interactions (CI)" calculation using MO by density functional calculations. Experimental spectra from three compounds having different d-electron numbers and coordination numbers, i.e., $SrTiO_3$, NiO and CaF_2, were successfully reproduced by this method.

In this thesis, we have extended this method for the analysis of chemical states and local environment of TM atoms in solid state materials.

In chapter 3, this method is applied to Fe $L_{2,3}$-edge NEXAFS for three kinds of iron oxides with different formal charges, i.e., FeO (Fe(II)), $LaFeO_3$ (Fe(III)), and $SrFeO_3$ (Fe(IV)). The usefulness of the method for the for the chemical state analysis of iron compounds is confirmed. In chapter 4, the electronic structures of three kinds of nickel oxides, i.e., NiO, $LiNiO_2$, and NiO_2 (Li-extracted $LiNiO_2$) are investigated by Ni $L_{2,3}$ NEXAFS. $LiNiO_2$ and NiO_2 are both important in lithium-ion batteries as cathode materials[23–25]. Changes in the electronic structure due to lithium extraction such as valency and spin-state of nickel ions are therefore very interesting, not only from a fundamental viewpoint, but also for development of new materials. The difference of spectral shapes due to the difference of spin configuration at initial states is discussed. The origin

of satellite peaks are also discussed in detail.

In chapter 5, the local environment of Mn atoms doped in wide-gap semiconductors, i.e., ZnO, GaN and spinel Ga_2O_3 are investigated. Semiconductors doped with dilute magnetic elements, now referred to as diluted magnetic semiconductors (DMS), have been extensively studied in order to archive DMSs with room temperature ferromagnetism to be used for new spin-electronic devices[26–28]. Recently many reports claimed their success of room temperature ferromagnetism in wide-gap matters[29–32]. However, mechanism behind the ferromagnetism is still controversial. For the detailed understanding of the magnetic properties, it is essential to know the environment of the doped transition elements on an atomic scale. In order to identify the chemical and physical states of Mn atoms in semiconductors, Mn $L_{2,3}$-edge NEXAFS is adopted combined with first principles many-electron calculations. To obtain better reproductions of experimental spectra by theory, a new computational method with increasing approximation level is introduced. By using the new method, one can recognize not only chemical states, but also coordination number of Mn atoms.

In chapter 6, another theoretical method which can explicitly deal with the interactions among all electrons including inner-shell electrons, is introduced to obtain more better agreement with experiment and theory. The relativistic correction of electron-electron interactions[33–35] are also included. This method is applied to the TM $L_{2,3}$-edge NEXAFS of four TM mono-oxides, i.e, CoO, FeO, MnO and TiO. The energy separation between L_3-edge and L_2-edge can be improved by this method, which is important for light transition elements since large overlap between L_3- and L_2-edge exist. The effects of relativistic correction term on the spectral shapes and branching ratio are thoroughly discussed.

References

[1] D. C. Koningsberger and R. Prins, eds., *X-Ray Absorption: Principles, Applications, Techniques of EXAFS, SEXAFS and XANES*, Chemical Analysis: A Series of Monographs on Analytical Chemistry and Its Applications (John Wiley & Sons, Inc., New York, 1988).

[2] J. Kawai, *Encyclopedia of Analytical Chemistry* (John Wiley & Sons, Inc., Chichester, 2000), chap. Absorption Techniques in X-ray Spectrometry, pp. 13288–13315.

[3] J. Stöhr, *NEXAFS Spectroscopy*, Springer Series in Surface Sciences (Springer Verlag, Berlin, 1992).

[4] J. G. Chen, Surf. Sci. Rep. **30**, 1 (1997).

[5] I. Tanaka, T. Mizoguchi, M. Matsui, S. Yoshioka, H. Adachi, T. Yamamoto, T. Okajima, M. Umesaki, W. Y. Ching, Y. Inoue, et al., Nat. Mater. **2**, 541 (2003).

[6] P. Gambardella, S. S. Dhesi, S. Gardonio, C. Grazioli, P. Ohresser, and C. Carbone, Phys. Rev. Lett. **88**, 047202 (2002).

[7] S.-J. Hwang and J.-H. Choy, J. Phys. Chem. B **107**, 5791 (2003).

[8] J. J. Rehr and R. C. Albers, Rev. Mod. Phys. **72**, 621 (2000).

[9] A. Filipponi, a. Di Cicco, and C. R. Natoli, Phys. Rev. B **52**, 15122 (1995).

[10] A. Filipponi and a. Di Cicco, Phys. Rev. B **52**, 15135 (1995).

[11] S.-D. Mo and W. Y. Ching, Phys. Rev. B **62**, 7901 (2000).

[12] T. Mizoguchi, I. Tanaka, S. Yoshioka, M. Kunisu, T. Yamamoto, and W. Y. Ching, Phys. Rev. B **70**, 045103 (2004).

[13] I. Tanaka, T. Mizoguchi, and T. Yamamoto, J. Am. Ceram. Soc. **88**, 2013 (2005).

[14] B. T. Thole and G. van der Laan, Phys. Rev. B **38**, 3158 (1988).

[15] F. M. F. de Groot, Z. W. Hu, M. F. Lopez, G. Kaindl, F. Guillot, and M. Tronc, J. Chem. Phys. **101**, 6570 (1994).

[16] G. Herzberg, *Atomic spectra and atomic structure* (Dover publications, New York, 1944), 2nd ed.

[17] A. Kotani, J. Electron Spectrosc. Relat. Phenom. **100**, 75 (1999).

[18] F. M. F. de Groot, J. Electron Spectrosc. Relat. Phenom. **67**, 529 (1994).

[19] F. de Groot, Chem. Rev. **101**, 1779 (2001).

[20] F. de Groot, Coord. Chem. Rev. **249**, 31 (2005).

[21] R. D. Cowan, *The theory of atomic structure and spectra* (University of California Press, Berkeley, 1981).

[22] K. Ogasawara, T. Iwata, Y. Koyama, T. Ishii, I. Tanaka, and H. Adachi, Phys. Rev. B **64**, 115413 (2001).

[23] T. Ohzuku, A. Ueda, and M. Nagayama, J. Electrochem. Soc. **140**, 1862 (1993).

[24] M. Broussely, P. Biensan, and B. Simon, Electrochim. Acta **45**, 3 (1999).

[25] M. S. Whittingham, Chem. Rev. **104**, 4271 (2004).

[26] W. Prellier, A. Fouchet, and B. Mercey, J. Phys.: Condens. Matter **15**, R1583 (2003).

[27] S. J. Pearton, C. R. Abernathy, M. E. Overberg, G. T. Thaler, D. P. Norton, N. Theodoropoulou, A. F. Hebard, Y. D. Park, F. Ren, J. Kim, et al., J. Appl. Phys. **93**, 1 (2003).

[28] C. Liu, F. Yun, and H. Morkoç, J. Mater. Sci.: Mater. Electron. **16**, 555 (2005).

[29] P. Sharma, A. Gupta, K. V. Rao, F. J. Owens, R. Sharma, R. Ahuja, J. M. O. Guillen, B. Johansson, and G. A. Gehring, Nat. Mater. **2**, 673 (2003).

[30] R. Janisch, P. Gopal, and N. A. Spaldin, J. Phys.: Condens. Matter **17**, R657 (2005).

[31] S. Sonoda, S. Shimizu, T. Sasaki, Y. Yamamoto, and H. Hori, J. Cryst. Growth **237-239**, 1358 (2002).

[32] H. Hayashi, R. Huang, H. Ikeno, F. Oba, S. Yoshioka, I. Tanaka, and S. Sonoda, Appl. Phys. Lett. **89**, 181903 (2006).

[33] G. Breit, Phys. Rev. **34**, 375 (1929).

[34] J. Sucher, Phys. Rev. A **22**, 348 (1980).

[35] M. H. Mittleman, Phys. Rev. A **24**, 1167 (1981).

Chapter 2

Relativistic Many-Electron Theory

2.1 One Electron Dirac Equation

The wave equation for electrons, which consistent with both the principles of quantum mechanics and the theory of special relativity, is formulated by Paul Dirac (See Chapter XI of Ref. [1]). The Dirac equation of an electron in the potential from external field $v_{ext}(r)$, which does not explicitly depend on time, is given by,

$$h_D \phi = \varepsilon \phi, \tag{2.1}$$

$$h_D = c\boldsymbol{\alpha} \cdot \boldsymbol{p} + c^2 \beta + v_{ext}(r) \tag{2.2}$$

in atomic unit. Here, c is velocity of light, $\boldsymbol{\alpha}$ and β are linear operators act on the one-electron wave function, which must satisfy anti-commutation relations

$$\{\alpha_i, \alpha_j\} = \alpha_i \alpha_j + \alpha_j \alpha_i = 2\delta_{ij}, \tag{2.3}$$

where α_i is β for $i = 0$ and $\alpha_x, \alpha_y, \alpha_z$ for $i = 1, 2, 3$, respectively. When looking for matrix expressions of α_i and β, they must be, at least, four dimensional. A conventional (but not unique) expression of Dirac matrices, α_i and β, are defined as

$$\alpha_i = \begin{pmatrix} 0 & \sigma_i \\ \sigma_i & 0 \end{pmatrix}, \quad \beta = \begin{pmatrix} I_{2\times2} & 0 \\ 0 & -I_{2\times2} \end{pmatrix}, \quad (i = x, y, z), \tag{2.4}$$

where $I_{2\times2}$ is two dimensional unit matrix, and σ_i are the Pauli spin matrices

$$\sigma_x = \begin{pmatrix} 0 & 1 \\ 1 & 0 \end{pmatrix}, \quad \sigma_y = \begin{pmatrix} 0 & -i \\ i & 0 \end{pmatrix}, \quad \sigma_z = \begin{pmatrix} 1 & 0 \\ 0 & -1 \end{pmatrix}. \tag{2.5}$$

Notice that the Dirac equation (2.1) can only describe the motion of spin 1/2 particles.

Since the Dirac Hamiltonian holds 4×4 matrices, the eigenfunctions $\{\phi\}$ must be a four component vector

$$\phi = \begin{pmatrix} \phi_1 \\ \phi_2 \\ \phi_3 \\ \phi_4 \end{pmatrix}. \tag{2.6}$$

Therefore, the wavefunction contains the four degrees of freedom: two of them are associated with the group of eigenstates with positive and negative energy, and each group holds two degrees of freedom corresponding to the probability amplitude for up-spin and down-spin along with specified direction. The positive energy states, which are dominated by ϕ_1 and ϕ_2 components, describe electron states, while the negative energy states dominated by ϕ_3 and ϕ_4, describe the positron – the anti-particle of electron – states.

As described in the following section, the existence of negative energy states gives rise to some difficulties solving relativistic many-electron wave equations.

2.2 Relativistic Many-Electron Hamiltonians

2.2.1 Dirac-Coulomb Hamiltonian

The theory of special relativity requires that the relativistic wave equation has to be invariant under the Lorentz transformation. The one-electron Dirac equation satisfy this condition, hence it can exactly describe the relativistic motion of single electron or positron. Unfortunately, we do not have such relativistic equations for many-electron system.

An approximate relativistic Hamiltonian used for many years is formulated in analogy to the standard non-relativistic theory. By combining the instantaneous Coulomb interaction, $V_{ee}(i,j) =$

$1/r_{ij}$, with the Dirac's one-electron theory yield the Dirac-Coulomb Hamiltonian

$$H_{DC} = \sum_{i=1}^{N} h_D(i) + \sum_{i=1}^{N} \sum_{j<i} \frac{1}{r_{ij}}. \tag{2.7}$$

Here $h_D(i)$ is the one-particle Dirac operator acting on i th electron or positron described in (2.2). There are several problems for this Hamiltonian. First of all, the associated equation

$$H_{DC}\Psi = E\Psi \tag{2.8}$$

is not Lorentz invariant. Therefore Dirac-Coulomb Hamiltonian is not an appropriate for relativistic theory, though this Hamiltonian could be a good guess for atoms and molecules composed of lighter elements, since the electron-electron interaction is expected not to be modified significantly by the introduction of special relativity.

The other problem, now known as "Brown-Ravenhill disease", is that when $n > 1$, the Dirac-Coulomb Hamiltonian H_{DC} or eq. (2.8) has no eigenfunction corresponding to bounded state. This problem was first pointed out by Brown and Ravenhill [2]. This is because any normalizable product eigenfunctions $u^{(0)}$ of

$$H_{DC}^{(0)} = \sum_{i=1}^{n} h_D(i) \tag{2.9}$$

are degenerate with a continuum of wave functions in which one or more electrons are in negative-energy continuum eigenstates $v^{(0)}$ of h_D, and the electron-electron interactions V_{ee} leads to "dissolving" $u^{(0)}$ into the continuum states (thus, this phenomena is sometimes called as "continuum dissolution"). More detailed explanation has been given by Sucher [3].

The difficulties associated to the H_{DC} come from the fact that H_{DC} corresponds to the use of Dirac's one-particle theory. When there are more than two interacting electrons, Dirac's one-electron theory breaks down and it is required to introduce quantum electrodynamics (QED). QED is the relativistic quantum field theory which describes the interactions of electrons positrons and photons with each other and with external static potential. The Hamiltonian of QED (H_{QED}) also includes the interactions of these particles with external electromagnetic field which are defined in terms of the vector potential $A(r)$. The operator H_{QED} acts in a Fock space (which is the direct sum of the tensor products of single particle Hilbert spaces) including arbitrary large number

of electrons, positrons and photons. It is known that one can automatically avoid the "Brown-Ravenhill disease" if Fock space Hamiltonian is used (so, this problem is somewhat artifact) [4]. However, H_{QED} is too complicated to use for numerical calculation, since this Hamiltonian only conserves the total charge in the system, and not conserve the number of electrons, positrons or photons separately. Even the ground state with zero charge, i.e., the vacuum state, the eigenstate of H_{QED} is a mixture of arbitrary number of electron-positron pair states and is rather complicated state.

2.2.2   No-pair Hamiltonians

In order to calculate the relativistic many-electron wave functions of molecules or solid state materials, we need a more simple Hamiltonian which refers to a definite number $N(>0)$ of electrons, but zero positrons and photons, and has bound state eigenfunctions. Such Hamiltonian was derived from the Hamiltonian of QED by several authors [3–6].

It is possible to divide the H_{QED} into two part: the one is the "pair part" H^{pair}, which involves the creation or annihilation of virtual electron-positron pairs or photons, and the other is "no-pair part" H^{np}, as

$$H_{QED} = H^{np}_{QED} + H^{pair}_{QED}. \tag{2.10}$$

The operator H^{np} commutes with the electron and positron number operators N_e and N_p, as well as with the photon number operators N_{ph}. Now we can look for the eigenstates of H^{np} with definite number of these particles. In particular, we are interested in the $N_e = N, N_p = N_{ph} = 0$ case, i.e., the eigenvalue problem is defined as

$$N_e \Psi = N\Psi, \quad N_p \Psi = N_{ph}\Psi = 0, \tag{2.11}$$

and

$$H^{np}_{QED}\Psi = E\Psi. \tag{2.12}$$

The eigenvalue problem described above is defined in the subspace of Fock space spanned by the products of electronic states of one-electron Dirac's operator. It can easily be converted into a wave equation in a configuration space corresponding to the many-electron Dirac-spinor $\psi =$

$\psi(r_1, ..., r_N)$

$$H^+\psi = E\psi, \tag{2.13}$$

where

$$H^+ = \sum_{i=1}^{N} \Lambda_i^+ h_D(i)\Lambda_i^+ + \sum_{i=1}^{N}\sum_{j<i} \Lambda_i^+ \Lambda_j^+ V_{ee}(i,j)\Lambda_j^+ \Lambda_i^+. \tag{2.14}$$

Here, Λ_i^+ denotes the projection operator onto the positive energy eigenstates (electronic states) of one-particle Dirac Hamiltonian $h_D(i)$ defined in (2.2), or more general basis set which are the eigenfunctions of a one-particle operator written as

$$h_D'(i) = c\boldsymbol{\alpha} \cdot \boldsymbol{p} + c^2\beta + v_{ext}(r_i) + U_{eff}(i), \tag{2.15}$$

where $U_{eff}(i)$ is an arbitrary potential such as approximated potential of electron-electron interactions. Because of the presence of Λ_i^+ operators, the Hamiltonian H^+ has normalizable, bound-state solutions.

When taking the instantaneous Coulomb interaction for V_{ee} in (2.14), this Hamiltonian is called 'no-pair' Dirac-Coulomb Hamiltonian. This Hamiltonian is obtained by simply dropping the pair part H_{pair} which create or annihilate virtual electron-positron pairs and photons from H_{QED}. The 'no-pair' Dirac-Coulomb Hamiltonian is not Lorentz invariant, as described in previous section, and misses the order α^2 (α is the fine structure constant) contribution of H_{pair}, hence is correct only to the order of α^0.

Normally, the H_{pair} is treated by the perturbation theory. The leading term of the exchange between virtual photons and electrons is given as, in Coulomb gauge ($\nabla \cdot \boldsymbol{A} = 0$, where $\boldsymbol{A}$ denotes vector potential),

$$B(i,j) = -\frac{1}{2r_{ij}}\left\{\boldsymbol{\alpha}_i \cdot \boldsymbol{\alpha}_j + \frac{(\boldsymbol{\alpha}_i \cdot \boldsymbol{r}_{ij})(\boldsymbol{\alpha}_j \cdot \boldsymbol{r}_{ij})}{r_{ij}^2}\right\}. \tag{2.16}$$

This formula is first derived by Breit [7, 8] an is now known as frequency-independent Breit operator. In physically meaning, the Breit operator contains the magnetic interactions introduced via the orbital and spin motions, and the retardation effect in the limit of small velocities. By adding Breit operator $B(i,j)$ to the zeroth-order 'no-pair' Dirac Coulomb Hamiltonian, we get the 'no-pair' Dirac-Coulomb-Breit Hamiltonian which is correct to the order of α^2. Though the 'no-pair' Dirac-Coulomb-Breit Hamiltonian is still an approximated, it provides best description of

Lorentz invariance in relativistic interaction, and increases the accuracy of calculated fine structure splitting and electron bonding energy of inner electrons [9, 10].

It is worth noting that the 'no-pair' Hamiltonian (2.14) and hence the eigenvalues are depend on the choice of projection operators Λ_i^+, though the differences between different choices are at least the order to α^3. More detailed discussion about that is found in ref. [11].

2.3 Relativistic Configuration Interaction Method

Starting from 'no-pair' Hamiltonian, almost all method in quantum chemistry formulated for non-relativistic many-electron problem, such as Hartree-Fock method, configuration interaction method (CI), coupled-cluster method (CC), multi-configuration self-consistent-field method (MCSCF) and many-body perturbation theory (MBPT), can be extended in straightforward manner [12–19].

In present work, the configuration interaction method was adopted, since ground state and excited states many-electron eigenvalues and eigenfunctions can be obtained simultaneously. It is convenient for the calculations of transition probabilities for $L_{2,3}$-edge NEXAFS spectra.

2.3.1 Relativistic One-Electron Calculations

In order to calculate the eigenvalues and eigenfunctions of H^+ given in (2.14), a finite orthonormal basis set of one-electron states are chosen. The positive energy eigenstates $\{\phi_i | i = 1, 2, ..., m\}$ of one-particle Dirac operator h_D' in (2.15) are used so that

$$\Lambda_i^+ \phi_i = \phi_i, \quad (i = 1, 2, ..., m). \tag{2.17}$$

Then, we look for the approximated wave functions in the 'finite Fock space', which is a direct sum of all finite N-electron Hilbert space ($N < m$) that are spanned by N-electron Slater determinants constructed from the given m orthonormal one-electron states $\{\phi_i\}$.

In most case, Dirac-Hartree-Fock method, the relativistic version of Hartree-Fock method, is used to calculate $\{\phi_i\}$. In this method, the dynamic electron correlation effects are not include in the equation: these effects are taken into account through CI. The alternative choice is using the solutions of Dirac-Kohn-Sham equation, which is the one-particle Dirac equation derived from

relativistic density functional theory [20–22]. In the Dirac-Kohn-Sham equation, the electron correlation effects are approximately included through the exchange-correlation potential whose exact formalism has not known yet. Therefore, the correction of electron correlation effects are taken into account through CI based on Dirac-Kohn-Sham orbitals. The latter approach was adopted in the present work.

2.3.2 Variational Collapse

In the one-electron calculation, we usually expand the one-electron wave functions with a finite basis set and replacing the Hamiltonian to matrix representation. However, spurious unphysical solutions occur, when diagonalizing that Hamiltonian matrix, with zero or near zero kinetic energy, which often lie deeper energy than expected values. Moreover, there is no systematic variation of the eigenvalues with increasing number of basis, and do not form the upper bound to the exact eigenvalues [23]. This problem is called "variational collapse" or "finite basis set disease", which is serious problem in practical viewpoint [24, 25].

Such difficulty comes from the fact that the energy spectrum of one-electron Dirac operator is neither bounded below nor bounded above. Therefore, the conventional Rayleigh-Ritz variational method breaks down, since it is only justified for the Hamiltonian with semi-bounded energy spectrum. Various approaches have been proposed to avoid variational collapse: for instance, transforming Dirac operator [26, 27], using the special basis set [25, 28–30], or imposing the certain relations between large and small components [31, 32]. Other feasible approaches have also been proposed based on applying the modified variational method [33, 34] or applying Rayleigh-Ritz variational method to the inverse Hamiltonian operator H^{-1} [35].

In the present work, four-component molecular orbitals (MO) for electron states are calculated within the relativistic density functional scheme. Numerically generated four-component atomic orbitals (AO) are used as basis functions for these MO. In order to avoid the variational collapse, only the AO corresponding to the elecrton states are selected for basis function of MO.

2.3.3 Configuration Interaction

Once proper one-electron states $\{\phi_i | i = 1, 2, ..., m\}$ are obtained, a N-electron wave function can be expressed as a linear combination of N-electron Slater determinants. The most general N-electron state is given by

$$\Psi(r_1, ..., r_N) = \sum_{p_1, ..., p_N} C(p_1, ..., p_N) \Phi_{p_1, ..., p_N}(r_1, ..., r_N) \equiv \sum_p C_p \Phi_p, \qquad (2.18)$$

where $\Phi_p \equiv \Phi_{p_1, ..., p_N}(r_1, ..., r_N)$ are the Slater determinants constructed from $p_1, ..., p_N$-th one-electron states expressed as

$$\Phi_{p_1, ..., p_N}(r_1, ..., r_N) = \frac{1}{\sqrt{N!}} \begin{vmatrix} \phi_{p_1}(r_1) & \phi_{p_1}(r_2) & \cdots & \phi_{p_1}(r_N) \\ \phi_{p_2}(r_1) & \phi_{p_2}(r_2) & \cdots & \phi_{p_2}(r_N) \\ \vdots & \vdots & \ddots & \vdots \\ \phi_{p_N}(r_1) & \phi_{p_N}(r_2) & \cdots & \phi_{p_N}(r_N) \end{vmatrix}, \qquad (2.19)$$

and the sum in (2.18) runs over the all possible N-combinations from m index of one-electron states.

In principle, we can determine the $_NC_m$ number of coefficients $C_p = C(p_1, ..., p_N)$ in (2.18) for 'no-pair' Hamiltonian H^+ given in (2.14) by using the standard Rayleigh-Ritz variational method, since H^+ have bounded eigenvalues. This method is called "full-CI", whose solutions give the best description of many-electron states for given finite basis set $\{\phi_i | i = 1, 2, ..., m\}$.

At first, the matrix elements of one-particle and two-particle operators in H^+ are constructed as

$$h_{ij} = \int \phi_i^*(r) h_D(r) \phi_j(r) d^3 r, \qquad (2.20)$$

$$V_{ij,kl} = \iint \phi_i^*(r_1) \phi_j^*(r_2) V_{ee}(1, 2) \phi_k(r_1) \phi_l(r_2) d^3 r_1 d^3 r_2, \qquad (2.21)$$

where

$$V_{ee}(1, 2) = \frac{1}{r_{12}} \qquad (2.22)$$

for 'no-pair' Dirac-Coulomb Hamiltonian, and

$$V_{ee}(1, 2) = \frac{1}{r_{12}} + B(1, 2) \qquad (2.23)$$

for 'no-pair' Dirac-Coulomb-Breit Hamiltonian. Then the Hamiltonian matrix elements are evaluated as

$$
\begin{aligned}
H_{pq}^{+} &= \langle \Phi_p | H^+ | \Phi_q \rangle \\
&= \sum_{i=1}^{m} \sum_{j=1}^{m} h_{ij} \langle \Phi_p | a_i^\dagger a_j | \Phi_q \rangle + \frac{1}{2} \sum_{i=1}^{m} \sum_{j=1}^{m} \sum_{k=1}^{m} \sum_{l=1}^{m} V_{ij,kl} \langle \Phi_p | a_i^\dagger a_j^\dagger a_k a_l | \Phi_q \rangle
\end{aligned} \tag{2.24}
$$

where a_i and $a_i^\dagger$ denote the creation and annihilation operator for an electron in the one-electron orbital ϕ_i respectively, which satisfy the following anti-commutation relations

$$
\left\{ a_i, a_j \right\} = \left\{ a_i^\dagger, a_j^\dagger \right\} = 0, \quad \left\{ a_i, a_j^\dagger \right\} = \delta_{ij}. \tag{2.25}
$$

The coefficient C_p is obtained by diagonalizing this Hamiltonian matrix as an eigenvector with a corresponding eigenvalue. However, this calculation is only possible if both the number of electrons N and the basis size m are small. Otherwise the number $_NC_m$ of Slater determinants and corresponding coefficients becomes too large. Let consider a Mn isolated atom described as 25 electrons are in 36 ($1s - 4p$) atomic orbitals. Even in such simple case, we have to deal with the $_{36}C_{25} \cong 6 \times 10^8$ determinants. It is possible to significantly reduce this number by using the symmetry of system about 1 or 2 order, but the remaining numbers are still prohibitively large. Therefore the "full-CI" method is only applicable to the very limited system.

Practically, CI calculations are carried out with restricted electronic configurations to reduce the number of variational parameters C_p. A standard method is the limited CI approach, which truncate the expansion after the n-ple excitation configuration from Hartree-Fock or density functional ground state determinant. The different levels of truncation corresponding to $n = 2, 3, 4$, called CI singles-doubles (CISD), CI singles-doubles-triples (CISDT) and CI singles-doubles-triples-quadruples (CISDTQ) methods, respectively, are commonly used.

The truncation of electronic configurations can be done by another criterion. The restricted active space (RAS) CI formalism is a method of specifying the configurations to include in a truncated CI by dividing the orbitals into subsets and imposing restrictions on the allowed configurations based upon occupations within those subsets [36]. In RAS-CI calculation, the one-electron orbitals $\{\phi_i\}$ are divided into any or all of the following 5 subsets:

- frozen core — all orbitals are occupied

- RAS I — at least N_1 of those orbitals are occupied

- RAS II — no restrictions for the occupation number

- RAS III — at most N_3 of those orbitals are occupied

- (deleted) virtual — all orbitals are always unoccupied

The first subset consists of the inner shell orbitals, which interact only weakly with the other orbitals, and are considered to be frozen, i.e., always occupied in any allowed electronic configuration. The following three subsets, denoted RAS I, II, III, includes the orbitals believed to be particularly important to the system under investigation (I sometimes use in this thesis the term "active space" involving all RAS I, II, III). The Slater determinants are limited by requiring a minimum of N_1 electrons in RAS I and a maximum of N_3 electrons in RAS III. There are no restriction on the number of electrons in RAS II. The last subset denoted (deleted) virtual includes only the very highest ling orbitals, which contribute very weakly to the system and may safely be deleted from consideration. When RAS I and RAS III do not hold any orbitals, such classification of orbitals is called complete active space (CAS).

Further reduction of computational costs is achieved by taking the hybrid method of density functional theory (DFT) and CI calculations. In this approach, electronic correlations among particularly important orbitals are taken account by CI scheme, while correlations among other orbitals are approximately treated within the framework of DFT[37, 38].

The effective 'no-pair' Hamiltonian for selected n electrons can be described as

$$H_{eff} = \sum_{i=1}^{n} \Lambda_i^+ h_{D,eff}(i)\Lambda_i^+ + \sum_{i=1}^{n}\sum_{j<i} \Lambda_i^+ \Lambda_j^+ V_{ee}(i,j)\Lambda_j^+ \Lambda_i^+,$$

$$h_{D,eff}(i) = c\alpha_i \cdot p + c^2\beta_i + v_{ext}(r_i) + v_0(r_i). \tag{2.26}$$

Here the $v_0(r_i)$ denote the approximated exchange correlation potential from the other $N - n$ electrons. The Hamiltonian matrix elements are evaluated using eq. (2.24), where sums only over the selected orbitals. Therefore we only need to calculate one-particle and two-particle matrix elements (2.21), (2.20) among selected orbitals, which leads to the significant reduction of computational time. However, the quality of obtained eigenstates are depend on the exchange-correlation

potentials used in calculations. Such potential dependence can be reduced by taking the increasing number of selected orbitals n, and minimized by taking all N orbitals for CI.

2.4 Theory of Transition Metal $L_{2,3}$-edge NEXAFS

In quantum mechanics, the interaction between a electron and photons (electromagnetic field) are treated as a perturbation. The photo-absorption coefficient μ, or photo absorption cross section (PACS) σ_{abs}, is the ratio between the photon energy flux absorbed in the core electron excitation process and the energy flux of incident photons. According to the "Fermi's Golden Rule", σ_{abs} can be described by

$$\sigma_{abs}(\omega) = \frac{4\pi^2\hbar\alpha}{m_e^2\omega}\sum_f \left|\left\langle \Psi_f \left| \sum_{j=1}^{N} exp(i\mathbf{k}\cdot\mathbf{r}_j)\,(\mathbf{\varepsilon}\cdot\mathbf{p}_j) \right| \Psi_i \right\rangle\right|^2 \delta(E_f - E_i - \hbar\omega) \tag{2.27}$$

where Ψ_f and Ψ_i are N-electron wave functions at final state and initial state, respectively. E_f and E_i are total energy of corresponding states. $\hbar\omega, \mathbf{k}$ and $\mathbf{\varepsilon}$ are energy, wave number vector and unit vector of polarization direction of x-ray (a photon). $\mathbf{p}_j$ is the momentum operator of j th electron. In x-ray absorption spectroscopy, the wave length of incident x-ray is much larger than atomic distance, i.e., $\mathbf{k}\cdot\mathbf{r} \ll 1$ and $exp(i\mathbf{k}\cdot\mathbf{r}) \approx 1$. Thus the transition matrix (bra-ket) in (2.27) can be evaluated in good approximation as

$$\left\langle \Psi_f \left| \sum_{j=1}^{N} exp(i\mathbf{k}\cdot\mathbf{r}_j)\,(\mathbf{\varepsilon}\cdot\mathbf{p}_j) \right| \Psi_i \right\rangle \cong \frac{im_e}{\hbar}(E_f - E_i)\left\langle \Psi_f \left| \mathbf{\varepsilon}\cdot\sum_{j=1}^{N} \mathbf{r}_j \right| \Psi_i \right\rangle, \tag{2.28}$$

which is corresponds to electric dipole transition. The commutation relations, $[H, \mathbf{r}_j] = -i(\hbar/m_e)\mathbf{p}_j$ are used to obtain (2.28). The quadrupole transitions or higher order transition are some hundred times weaker then the dipole transitions and can be neglected in most cases. Integrating (2.27) with $\hbar\omega$ under electric dipole approximation, one can obtain

$$\int \sigma_{abs}d(\hbar\omega) = \sum_f \frac{4\pi^2\alpha}{\hbar}(E_f - E_i)\left|\left\langle \Psi_f \left| \mathbf{\varepsilon}\cdot\sum_{j=1}^{N} \mathbf{r}_j \right| \Psi_i \right\rangle\right|^2. \tag{2.29}$$

In atomic physics, the oscillator strength of the electric dipole transition is defined as

$$I_{if} = \frac{2m_e}{\hbar^2}(E_f - E_i)\left|\left\langle \Psi_f \left| \mathbf{\varepsilon}\cdot\sum_{k=1}^{n} \mathbf{r}_k \right| \Psi_i \right\rangle\right|^2. \tag{2.30}$$

When using polycrystalline samples or irradiating unpolarized x-ray, we measure spectra averaged over the all directions. In such case, oscillator strength is given by

$$I_{if} = \frac{2m_e}{3\hbar^2}(E_f - E_i)\left| \left\langle \Psi_f \left| \sum_{k=1}^{n} r_k \right| \Psi_i \right\rangle \right|^2. \tag{2.31}$$

The multiplet structures of TM $L_{2,3}$-edge NEXAFS can be calculated by configuration interaction method. TM $L_{2,3}$-edge spectra can be mainly ascribed to the transition from $(\text{TM-}2p)^6(\text{TM-}3d)^{n_d}$ configuration to $(\text{TM-}2p)^5(\text{TM-}3d)^{n_d+1}$ configuration where n_d is the number of $3d$ electrons in a TM atom. Minor contributions because of electric dipole transitions from $2p$ to ns ($n = 4, 5, ...$) are negligible. The other configurations having two or more holes on TM-$2p$ are not considered since many-electron energies of such configurations much higher and do not interact with these two configurations described above. Using RAS-CI terminology, TM-$2p$ orbitals are classified to "RAS I" space with $N_1 = 5$, while TM-$3d$ orbitals are classified to "RAS II" space.

The oscillator strengths are evaluated by eq. (2.30). Using (2.18), the bra-ket in (2.29) can be expanded as

$$\left\langle \Psi_f \left| \boldsymbol{\varepsilon} \cdot \sum_{k=1}^{n} r_k \right| \Psi_i \right\rangle = \sum_p \sum_q C_{fp}^* C_{iq} \left\langle \Phi_p \left| \boldsymbol{\varepsilon} \cdot \sum_{k=1}^{n} r_k \right| \Phi_q \right\rangle$$

$$= \sum_p \sum_q C_{fp}^* C_{iq} \sum_{k=1}^{m} \sum_{l=1}^{m} d_{kl} \langle \Phi_p | a_k^\dagger a_l | \Phi_q \rangle, \tag{2.32}$$

where d_{kl} denote the dipole transition matrix element between one-electron states given by

$$d_{kl} = \int \phi_k^*(r)(\boldsymbol{\varepsilon} \cdot r)\phi_l(r)d^3r. \tag{2.33}$$

As described by de Groot *et al.* [39], each peak in a experimental $L_{2,3}$-edge NEXAFS spectrum has its own characteristic broadening. The broadening factor of each peak is determined by variety of phenomena such as the core-hole lifetime broadening, the Coster-Kronig Auger broadening, and the solid-state (dispersional and vibrational) broadening, which is currently too complicated to estimate nonempirically. Therefore, in present work, the curves obtained by the simple Gaussian or Lorentzian broadening are shown for easy comparison of experimental results.

References

[1] P. A. M. Dirac, *The principles of quantum mechanics*, The international series of monographs on physics (Oxford University Press, New York, 1981), 4th ed.

[2] G. E. Brown and D. G. Ravenhall, Proc. R. Soc. London Ser. A **208**, 552 (1951).

[3] J. Sucher, Phys. Scr. **36**, 271 (1987).

[4] J. Sucher, Phys. Rev. A **22**, 348 (1980).

[5] M. H. Mittleman, Phys. Rev. A **5**, 2395 (1972).

[6] M. H. Mittleman, Phys. Rev. A **24**, 1167 (1981).

[7] G. Breit, Phys. Rev. **34**, 375 (1929).

[8] G. Breit, Phys. Rev. **39**, 616 (1932).

[9] M. H. Chen, B. Crasemann, and H. Mark, Phys. Rev. A **25**, 391 (1982).

[10] K.-N. Huang, Y.-K. Kim, K. T. Cheng, and J. P. Desclaux, Phys. Rev. Lett. **48**, 1245 (1982).

[11] W. Kutzelnigg, Phys. Scr. **36**, 416 (1987).

[12] M. H. Chen, K. T. Cheng, and W. R. Johnson, Phys. Rev. A **47**, 3692 (1993).

[13] K. T. Cheng, M. H. Chen, W. R. Johnson, and J. Sapirstein, Phys. Rev. A **50**, 247 (1994).

[14] L. Visscher, T. Saue, W. C. Nieuwpoort, K. Faegri, and O. Gropen, J. Chem. Phys. **99**, 6704 (1993).

[15] E. Eliav, U. Kaldor, and Y. Ishikawa, Phys. Rev. A **49**, 1724 (1994).

[16] A. Landau, E. Eliav, L. Visscher, and U. Kaldor, Int. J. Mol. Sci. **3**, 498 (2002).

[17] C. M. Marian, M. R. A. Blomberg, and P. E. M. Siegbahn, J. Chem. Phys. **91**, 3589 (1989).

[18] J. K. Laerdahl, K. Faegri, L. Visscher, and T. Saue, J. Chem. Phys. **109**, 10806 (1998).

[19] M. J. Vilkas, K. Koc, and Y. Ishikawa, Chem. Phys. Lett. **296**, 68 (1998).

[20] A. K. Rajagopal and J. Callaway, Phys. Rev. B **7**, 1912 (1973).

[21] A. H. MacDonald and S. H. Vosko, J. Phys. C: Solid State Phys. **12**, 2977 (1979).

[22] E. Engel and R. M. Dreizler, *Density Functional Theory II: Relativistic and Time Dependent Extensions* (Springer-Verlag, Berlin, 1996), vol. 181 of *Topics in Current Chemistry*, pp. 1–80.

[23] H. Wallmeier and W. Kutzelnigg, Phys. Rev. A **28**, 3092 (1983).

[24] W. H. E. Schwarz and H. Wallmeier, Mol. Phys. **46**, 1045 (1982).

[25] W. Kutzelnigg, Int. J. Quantum Chem. **25**, 107 (1984).

[26] H. Wallmeier and W. Kutzelnigg, Chem. Phys. Lett. **78**, 341 (1981).

[27] W. E. Baylis and S. J. Peel, Phys. Rev. A **28**, 2552 (1983).

[28] G. W. F. Drake and S. P. Goldman, Phys. Rev. A **23**, 2093 (1981).

[29] W. Kutzelnigg, Chem. Phys. **225**, 203 (1997).

[30] W. R. Johnson, S. A. Blundell, and J. Sapirstein, Phys. Rev. A **37**, 307 (1988).

[31] J. D. Talman, Phys. Rev. Lett. **57**, 1091 (1986).

[32] A. Kołakowska, J. Phys. B: At., Mol. Opt. Phys. **29**, 4515 (1996).

[33] P. Falsaperla, G. Fonte, and J. Z. Chen, Phys. Rev. A **56**, 1240 (1997).

[34] J. Dolbeault, M. J. Esteban, and E. Séré, Int. J. Quantum Chem. **93**, 149 (2003).

[35] R. N. Hill and C. Krauthauser, Phys. Rev. Lett. **72**, 2151 (1994).

[36] J. Olsen, B. O. Roos, P. Jørgensen, and H. J. A. Jensen, J. Chem. Phys. **89**, 2185 (1988).

[37] K. Ogasawara, T. Ishii, I. Tanaka, and H. Adachi, Phys. Rev. B **61**, 143 (2000).

[38] K. Ogasawara, T. Iwata, Y. Koyama, T. Ishii, I. Tanaka, and H. Adachi, Phys. Rev. B **64**, 115413 (2001).

[39] F. M. F. de Groot, J. C. Fuggle, B. T. Thole, and G. A. Sawatzky, Phys. Rev. B **41**, 928 (1990).

Chapter 3

First Principles Calculations of Fe $L_{2,3}$-edge NEXAFS of Iron Oxides

3.1 Introduction

Many oxides of $3d$ transition elements have been widely used in modern technology. Since $3d$ electrons play central roles in them, experimental characterization of the $3d$ electrons is very important. Near edge x-ray absorption fine structures (NEXAFS) as well as electron energy loss near edge structures (ELNES) provides detailed information on electronic states near the Fermi energy. It monitors electronic transitions from a core orbital to unoccupied states that are allowed by electric dipole transition rule. The $3d$ states can therefore be analyzed directly using either $L_{2,3}$-edge or $M_{2,3}$ edge NEXAFS and ELNES. $3d$ elements has $L_{2,3}$-edge in a few 100 eV region, which is desirable for soft x-ray experiments as well as for ELNES. As a matter of facts, there have been a number of experimental $L_{2,3}$ NEXAFS are available for major $3d$-metal compounds. Their chemical shifts, spectral shape as well as the ratio between L_2 and L_3 spectra, i.e., branching ratio have been systematically investigated. The most primitive way to analyze the spectra is a so-called finger printing technique. A measured spectrum is identified by comparison with reference spectra obtained for standard materials. However, the finger printing technique is obviously not useful for new systems in which atomic/electronic structures are not analogous to preexisting compounds. A

good theoretical tool to analyze the experimental spectra is therefore mandatory. If one can obtain reliable theoretical spectrum for a given atomic arrangements and electronic states, the theoretical spectrum can be used as a new finger print.

A popular method to compute theoretical $L_{2,3}$-edge NEXAFS is the crystal field multiplet calculation [1–4] in which crystal field effects are incorporated into an atomic multiplet program using group theoretical formalism. Crystal field effects are included with parameters and they are determined so as to best fit to experimental spectra. A number of compounds have been investigated through this approach, and the parameters have been determined for many ions with different valence states and coordination environment. Although this method has been successful for reproducing many experimental spectra, the major drawback can be found in the method that uses empirical parameters. With the decrease of the symmetry of ligand field, the number of empirical parameters increases, thereby giving rise to the ambiguity of the computational results. Entirely first principles method is therefore strongly required. In 2001, a novel method to perform such a non-empirical calculation has been reported by the present author's group [5]. Totally relativistic first principles molecular orbital (MO) calculations were made. Then configuration interaction (CI) calculations were performed by using those MO. They have succeeded in reproducing experimental spectra from several compounds having different d-electron numbers and coordination numbers. In the present study, we have extended this method to three kinds of iron oxides with different formal charges, i.e., FeO (Fe(II)), $LaFeO_3$ (Fe(III)), and $SrFeO_3$ (Fe(IV)). The usefulness of the method for the iron compounds with different formal d-electron numbers is confirmed. Configuration analysis has been made to analyze the origin of peaks that appear in the spectra.

3.2   Computational procedure

For the calculation of theoretical Fe $L_{2,3}$-edge NEXAFS, model clusters of $(FeO_6)^{m-}$ that are composed of an Fe ion and six nearest neighbor O ions were used. The total number of electrons in the cluster was obtained from formal charges, thus $m = 10, 9, 8$ for FeO (Fe(II)), $LaFeO_3$ (Fe(III)), and $SrFeO_3$ (Fe(IV)) respectively. All cluster models were made to show octahedral (O_h) symmetry for simplicity even when real crystals exhibit slight distortion from the cubic symmetry. The Fe-O

bond lengths were 216.0, 195.0 and 192.5 pm for FeO, LaFeO$_3$, and SrFeO$_3$, respectively. In order to take account effective Madelung potential, point charges were put at the external atomic sites.

Fully relativistic molecular orbital (MO) calculations were carried out by solving Dirac equations with density functional theory using relativistic SCAT code [6]. In this code, four-component relativistic molecular orbitals are expressed as linear combination of atomic orbitals (LCAO). The numerically generated four-component relativistic atomic orbitals ($1s$ to $4p$ for Fe and $1s$ to $2p$ for O) were used as basis functions.

After one electron calculations of relativistic MO, configuration interaction (CI) calculations were performed. In present calculation, only Fe $2p$ orbitals and MO mainly composed of Fe $3d$ orbitals were considered explicitly. An effective many-electron Hamiltonian is given by (2.26) where v_{ext} is the electrostatic potential from nuclei, and v_0 is the potential from other electrons. The Coulomb interaction and exchange-correlation interaction among the selected n electrons are considered explicitly, while those interactions between the selected n electrons and other $N - n$ electrons are included in v_0 within the conventional local density approximation scheme. The explicit form of v_0 was derived by Watanabe and Kamimura [7].

As basis functions to diagonalize the many-electron Hamiltonians described in Eq., all the possible Slater determinants corresponding to the ground state (GS) configuration and the excited state (ES) configuration including a core hole were constructed. The many-electron wave functions are then expressed as linear combination of those Slater determinants. In the case of FeO (Fe(II)), the GS configuration is $(2p)^6(\phi_{3d})^6$, and the ES configuration is $(2p)^5(\phi_{3d})^7$ where ϕ_{3d} denotes the MO mainly composed of Fe $3d$ orbitals. The possible electronic configurations for GS are 210 ($=_6 C_6 \times_{10} C_6$) and those of ES are 720 ($=_6 C_5 \times_{10} C_7$). Thus 930 of Slater determinants were used as basis functions. For LaFeO (Fe(III)), the GS configuration is $(2p)^6(\phi_{3d})^5$, and the ES configuration is $(2p)^5(\phi_{3d})^6$. The possible electronic configurations for GS are 252 ($=_6 C_6 \times_{10} C_5$) and those of ES are 1260 ($=_6 C_5 \times_{10} C_6$). 1512 of Slater determinants were therefore used as basis functions. Regarding SrFeO (Fe(VI)), the GS configuration is $(2p)^6(\phi_{3d})^4$, and the ES configuration is $(2p)^5(\phi_{3d})^5$. The possible electronic configurations for GS are 210 ($=_6 C_6 \times_{10} C_4$) and those of ES are 1512 ($=_6 C_5 \times_{10} C_5$). The number of Slater determinants used as basis functions was 1722. The matrix elements of H between two Slater determinants were calculated

using eq. (2.24). After diagonalizing the Hamiltonian matirx, oscillator strength of the electric dipole transition averaged over all directions were calculated using eq. (2.31).

3.3 Results and Discussion

Calculations were made for FeO (Fe(II)), $LaFeO_3$ (Fe(III)), and $SrFeO_3$ (Fe(IV)). With the increase of the formal charge of transition elements, the covalent bonding between Fe-$3d$ and O-$2p$ is known to increase in general. Figure 1 shows contour maps of t_{2g} molecular orbitals in three clusters obtained by non-spin polarized and non-relativistic calculations. The O-$2p$ component in t_{2g} is found to increase with the increase of the formal charge of Fe. As a matter of fact, atomic orbital population of O-$2p$ is 2%, 7% and 18% in t_{2g} for FeO, $LaFeO_3$, and $SrFeO_3$, respectively. The atomic orbital population of O-$2p$ is greater for e_g orbital. They are 9%, 16% and 23% for FeO, $LaFeO_3$, and $SrFeO_3$, respectively. CI calculations using the molecular orbitals instead of atomic orbitals enable inclusion of the O-$2p$ orbital contributions through the covalency.

Using relativistic molecular orbitals, CI calculations were thoroughly made. Computed oscillator strengths given by Eq. (2.31) were shown with bars in Fig. 2. They were broadened by Gaussian functions of FWHM = 1.0 eV to make theoretical $L_{2,3}$-edge NEXAFS. They are compared with experimental spectra in Fig. 3.2. Best fitting with experimental spectra can be found when absolute transition energy of the theoretical spectra is shifted by -6.4 eV. The error may be ascribed to underestimation of correlation effects in the present theoretical method as discussed by Ogasawara et al. [8, 9] When all theoretical spectra are shifted for the same amount, they can reproduce three experimental spectra to the details. Chemical shifts of each compound as defined by the relative position of the most prominent peak are also well reproduced. As compared with FeO, it is +2.2 eV for both $LaFeO_3$ and $SrFeO_3$.

Fig. 3.3 shows contributions of four configurations to many electron eigenvalues. Although only a part of these components significantly contribute for the oscillator strength, the diagram is quite useful. The L_3 absorption can be divided into two parts with different number of electrons in t_{2g} and e_g orbitals. Therefore, the width of the L_3 absorption is primarily determined by the difference in the averaged energy of two configurations, which is given by the excitation energy
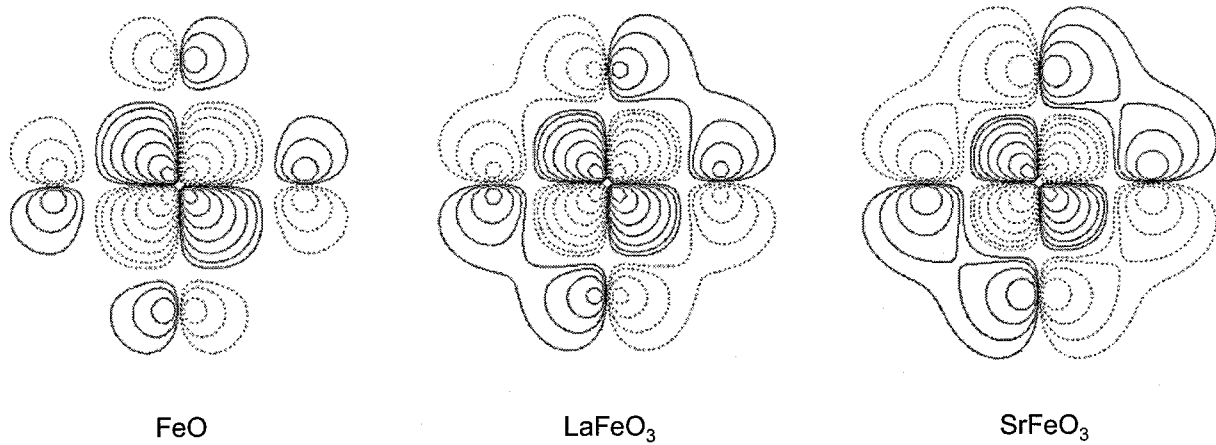
FeO   LaFeO$_3$ SrFeO$_3$

Figure 3.1: Contour map of t_{2g} molecular orbital in $(FeO_6)^{m-}$ cluster obtained by non-relativistic and non-spin polarized calculation. Solid and dotted curved are for positive and negative values, respectively.

from t_{2g} to e_g. The energy is called $10Dq$ or Δ_O when a metal ion is octahedrally coordinated. Theoretical Δ_O for three clusters as estimated by the difference in one-electron eigenvalues was 1.1, 1.8 and 1.8 eV for FeO, LaFeO$_3$, and SrFeO$_3$, respectively. The larger Δ_O by 39% explains why the L_3 of LaFeO$_3$, and SrFeO$_3$ show a tail toward high energy in the region at around 714 eV. FeO does not show such a tail.

No overlap between L_3 and L_2 can be found for FeO. A small overlap can be found for both LaFeO$_3$ and SrFeO$_3$. The magnitude of the overlap can be primarily determined by the magnitude of the splitting between $2p_{1/2}$ and $2p_{3/2}$. However, the magnitude of splitting is not dependent on valence state of ions. As a matter of fact, the splitting for Fe-$2p$ levels in three clusters is the same as 12.5 eV by the present relativistic calculation. The origin of the overlap between L_3 and L_2 in LaFeO$_3$ and SrFeO$_3$ cannot be explained by the difference in the splitting of Fe-$2p$ levels. The overlap can be explained by the difference in Δ_O, which is the same origin as the tail in the L_3 spectrum toward high energy in LaFeO$_3$ and SrFeO$_3$.

Measurement and interpretation of Fe-$L_{2,3}$ spectra of LaFeO$_3$ and SrFeO$_3$ have been made by Abbate, de Groot and coworkers in 1992 [10]. They have concluded that the presence of a ligand hole as denoted by $\underline{L}$ play a major role in determining the spectrum of SrFeO$_3$. Using
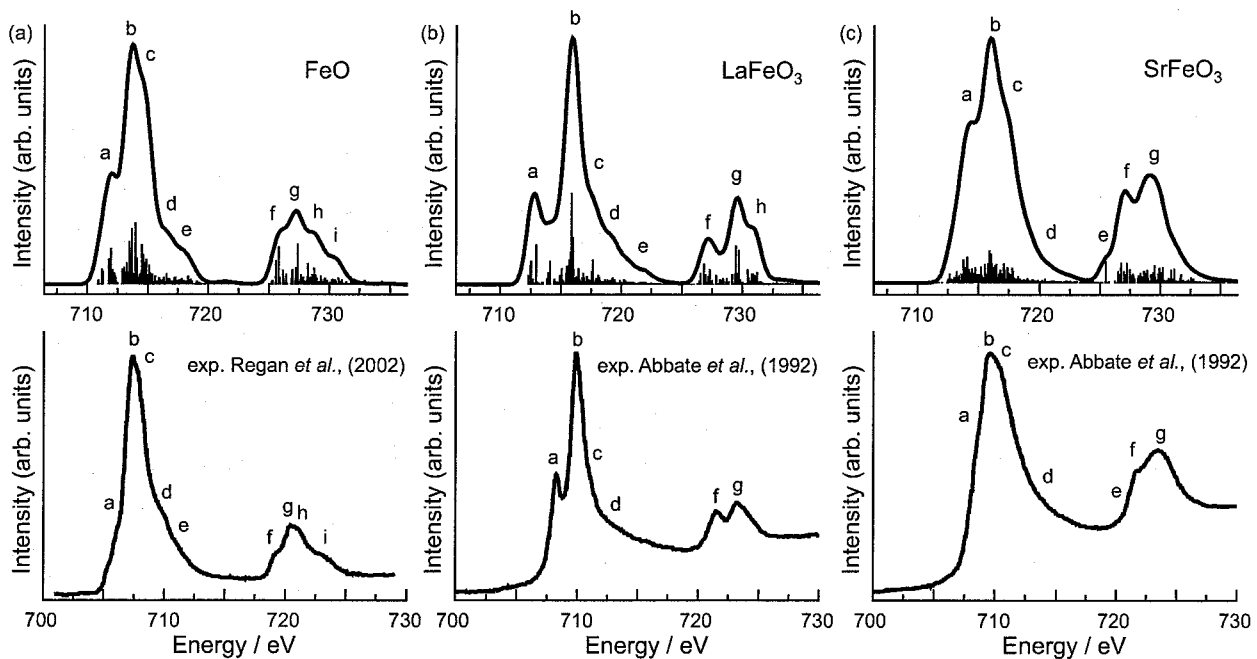
Figure 3.2: Theoretical Fe $L_{2,3}$-edge NEXAFS in (a) FeO, (b) LaFeO$_3$ and (c) SrFeO$_3$ (upper panel), and corresponding experimental NEXAFS spectra. Bars in the upper panel show oscillator strength with many-electron eigenvalues before the Gaussian broadening. Experimental NEXAFS spectra are adapted with permission from Refs. [10] and [11]. Copyrighted (2006) American Physical Society.
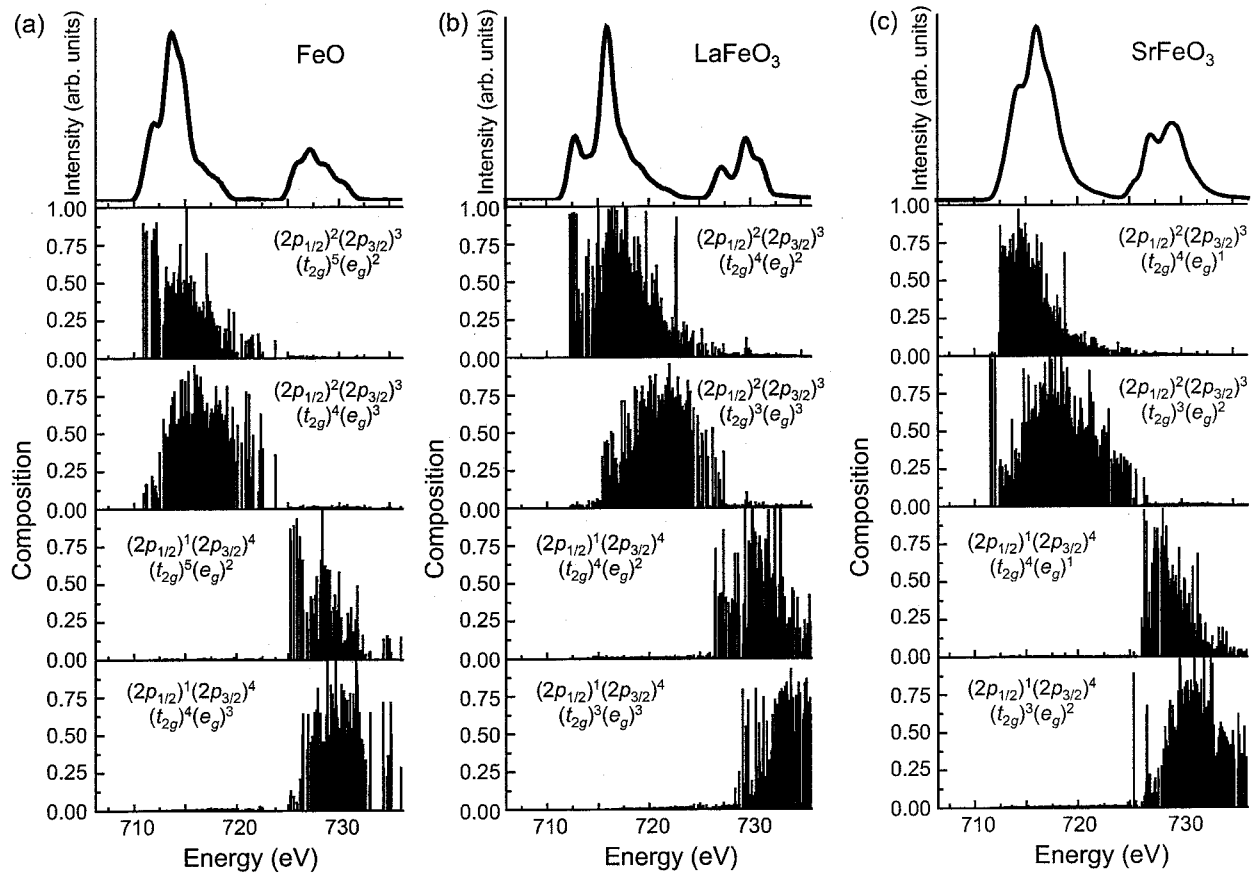
Figure 3.3: Configuration analysis of many-electron wave functions at the final states of the Fe $L_{2,3}$-edge NEXAFS.

the crystal field multiplet method, they claimed that the calculation taking $3d^4$ as a ground state cannot reproduce the experimental spectrum. They have proposed that the use of $3d^5\underline{L}$ as a ground state configuration of SrFeO3 is essential. In the present calculation, however, the experimental spectrum can be satisfactorily reproduced by the calculation by taking ϕ_{3d}^4 as a ground state, where ϕ_{3d} is the molecular orbital mainly composed of Fe-$3d$. It is true that significant admixture of O-$2p$ and Fe-$3d$ takes place especially for Fe(IV). There should be non-negligible contribution of the ligand hole to the Fe-$L_{2,3}$ spectrum. However, the major part of the contribution can be included by the CI calculations using the molecular orbitals instead of atomic orbitals. Using the computational method in this study, the major part of the ligand hole effect on the $L_{2,3}$ spectrum can be included without information on the covalency a priori. Thus the present method should be more useful for analysis of new kind of materials in which little information is available.

3.4 Summary

First principles calculation of Fe-$L_{2,3}$ NEXAFS of FeO, LaFeO3 and SrFeO3 have been made by CI calculations using fully relativistic four components wave functions. Relativistic MO calculations were carried out by solving Dirac equations with density functional theory. CI calculations were made using the molecular orbitals instead of atomic orbitals, which enables inclusion of the O-$2p$ orbital contributions through covalency. Then the oscillator strength of the electric dipole transition was computed. Experimental NEXAFS spectra of three compounds were satisfactorily reproduced by the theoretical spectra obtained for $(FeO_6)^{m-}$ clusters in octahedral symmetry. Chemical shifts between compounds were quantitatively reproduced as well. Configuration analysis was systematically made in order to analyze the origin of differences in spectral shapes.

References

[1] F. M. F. de Groot, J. C. Fuggle, B. T. Thole, and G. A. Sawatzky, Phys. Rev. B **41**, 928 (1990).

[2] F. M. F. de Groot, J. C. Fuggle, B. T. Thole, and G. A. Sawatzky, Phys. Rev. B **42**, 5459 (1990).

[3] F. M. F. de Groot, J. Electron Spectrosc. Relat. Phenom. **67**, 529 (1994).

[4] B. T. Thole and G. van der Laan, Phys. Rev. B **38**, 3158 (1988).

[5] K. Ogasawara, T. Iwata, Y. Koyama, T. Ishii, I. Tanaka, and H. Adachi, Phys. Rev. B **64**, 115413 (2001).

[6] A. Rósen, D. E. Ellis, H. Adachi, and F. W. Averill, J. Chem. Phys. **65**, 3629 (1976).

[7] S. Watanabe and H. Kamimura, Mater. Sci. Eng. B **3**, 313 (1989).

[8] K. Ogasawara, T. Ishii, I. Tanaka, and H. Adachi, Phys. Rev. B **61**, 143 (2000).

[9] K. Ogasawara, T. Miyamae, I. Tanaka, and H. Adachi, Mater. Trans. **43**, 1435 (2002).

[10] M. Abbate, F. M. F. Degroot, J. C. Fuggle, A. Fujimori, O. Strebel, F. Lopez, M. Domke, G. Kaindl, G. A. Sawatzky, M. Takano, et al., Phys. Rev. B **46**, 4511 (1992).

[11] T. J. Regan, H. Ohldag, C. Stamm, F. Nolting, J. Lüning, J. Stöhr, and R. L. White, Phys. Rev. B **64**, 214422 (2001).

Chapter 4

Ni $L_{2,3}$-edge NEXAFS/ELNES for LiNiO$_2$ and Related Compounds

4.1 Introduction

Lithium-ion batteries have been in wide use in the past decade because of their good properties, i.e., high voltage, high energy density both by volume and weight, long cycle-life, etc [1–3]. The most popular material for the positive electrode of the lithium-ion batteries is LiCoO$_2$. Many transition-metal oxides with larger capacity and less materials cost have been studied to replace LiCoO$_2$, e.g., LiNiO$_2$, LiMn$_2$O$_4$ and LiFePO$_4$. Recently, their derivatives containing two or more transition-metal elements, e.g., LiCo$_x$Ni$_{1-x}$O$_2$, LiNi$_{1/2}$Mn$_{1/2}$O$_2$, LiCo$_{1/3}$Ni$_{1/3}$Mn$_{1/3}$O$_2$, became attractive because of their improved properties. In order to design such oxides with multiple transition-metal elements, it is desirable to find out the redox center associated with lithium insertion and extraction.

Both near edge x-ray absorption fine structure (NEXAFS) and electron energy-loss near-edge structure (ELNES) are powerful techniques to observe electronic structures of selected elements. When measured using transmission electron microscopy, ELNES is identical to NEXAFS. We will hereafter refer only to NEXAFS. However, the same discussion can be made for ELNES. $L_{2,3}$-edge NEXAFS of a 3d transition metal element mainly corresponds to electric dipole transition from its 2p core levels to 3d orbitals. Minor contributions because of electric dipole transitions

35

from $2p$ to $ns(n = 4, 5, ...)$ and the electric quadrupole transition are negligible. Hence, the spectra directly reflect electronic structure of the $3d$ orbitals of the selected element. In spite of its potential usefulness, the $L_{2,3}$-edge is less used than the K-edge. One of the reasons is the difficulty of interpreting the measured spectra.

$L_{2,3}$ NEXAFS of $3d$ transition-metal compounds show widely spread multiplet structures. Strong correlation among spatially localized 3d electrons and that between the core-hole and the excited electron entirely changes the spectral shape. Therefore, one-electron calculations are useless for $L_{2,3}$ NEXAFS, in general. Recently, theoretical methods to explicitly include correlation between the core hole and the excited electron have been reported in several authors [4, 5]. However, none of them computed the multiplet structures because of the strong correlation among 3d electrons.

This group of the author has reported that the multiplet structures of $3d$ TM $L_{2,3}$ NEXAFS can be well reproduced by the hybrid method of density fundamental theory and configuration interaction method (DFT-CI) [6]. As demonstrated in previous chapter of this thesis, the spectral difference due to the chamical state of Fe $L_{2,3}$-edge NEXAFS of three iron oxides were well reproduced by this method. In this chapter, this method is applied to the Ni $L_{2,3}$ NEXAFS of three kinds of nickel oxides, i.e., NiO, LiNiO$_2$, and NiO$_2$ (Li-extracted LiNiO$_2$) and the change in the electronic structure of nickel ions due to lithium extraction is discussed. We also show a method to investigate the origin of satellite peaks in the spectra in terms of symmetry and electronic configurations.

4.2 Computational Procedure

The crystal structures of the three compounds are known by experiments [7, 8]. Ni ions are coordinated by six O ions. The model clusters of NiO_6^{m-}, which are composed of a Ni ion and six nearest-neighbor O ions, were used. The total number of electrons in the cluster was obtained from formal charges, thus m=10, 9, and 8 for NiO (Ni(II)), LiNiO$_2$ (Ni(III)), and NiO$_2$ (Ni(IV)), respectively. The cluster model of NiO shows O_h symmetry, while those of LiNiO$_2$ and NiO$_2$ show D_{3d} symmetry. The Ni-O bond lengths were 0.2090, 0.1967, and 0.1861 nm in NiO, LiNiO$_2$, and

NiO_2, respectively. In order to take account of effective Madelung potential, an array of point charges was set at the external atomic sites in the calculations.

Fully relativistic MO calculations were carried out by solving Dirac equations with the local density approximation (LDA) using the code that was originally described in Ref. [9]. Recently the code has been modified and successful in calculations of optical spectra of many laser crystals[10, 11]. In this code, four-component relativistic molecular orbitals are expressed as linear combination of AO (LCAO). The numerically generated four-component relativistic AO (1s to 4p for Ni and 1s to 2p for O) were used as basis functions for MO. After one-electron calculations of relativistic MO, we made many-electron calculations. Only Ni $2p$ orbitals and MO mainly composed of Ni $3d$ orbitals (as will be described by ϕ_{3d}, or by t_{2g} and e_g) were considered explicitly for the many-electron calculation. The effective many-electron Hamiltonian given in (2.26) was used. The explicit form of v_0 was derived by Watanabe and Kamimura [12].

The many-electron wave functions were expanded by Slater determinants constructed from selected 16 MO (6 Ni-$2p$ + 10 MO mainly composed of Ni 3d). Ni $L_{2,3}$ NEXAFS of NiO [Ni(II)] is due to the transitions from $(2p)^6(\phi_{3d})^8$ to $(2p)^5(\phi_{3d})^9$, where (ϕ_{3d}) denotes the MO mainly composed of Ni $3d$ orbitals. The number of possible Slater determinants for $(2p)^6(\phi_{3d})^8$ is 45 ($=_6 C_6 \times_{10} C_8$) and that for $(2p)^5(\phi_{3d})^9$ is 60 ($=_6 C_5 \times_{10} C_9$). Thus 105 Slater determinants were used as bases for many-electron wave functions. For $LiNiO_2$ [Ni(III)] $L_{2,3}$ NEXAFS corresponds to the transitions from $(2p)^6(\phi_{3d})^7$ to $(2p)^5(\phi_{3d})^8$. The number of Slater determinants for $(2p)^6(\phi_{3d})^7$ is 120 ($=_6 C_6 \times_{10} C_7$) and that for $(2p)^5(\phi_{3d})^8$ is 270 ($=_6 C_5 \times_{10} C_8$). Therefore, there were 390 Slater determinants used. In the case of NiO_2 [Ni(IV)] $L_{2,3}$ NEXAFS corresponds to the transitions from $(2p)^6(\phi_{3d})^6$ to $(2p)^5(\phi_{3d})^7$. The number of determinants is 210 ($=_6 C_6 \times_{10} C_6$) for $(2p)^6(\phi_{3d})^6$ and 720 ($=_6 C_5 \times_{10} C_7$) for $(2p)^5(\phi_{3d})^7$, thus, 930 in total.

After diagonalizing many-electron Hamiltonian matrix, the oscillator strengths of the electric dipole transition averaged over all directions were evaluated using eq. (2.31). This procedure was pointed out to overestimate the absolute transition energy typically by $< 1\%$ [6]. In Ref. [6], the transition energy was corrected by taking the orbital energy difference between single-electron orbitals for the Slater's transition state as a reference. We have adopted the same procedure in the present study.

4.3   Results and Discussion

4.3.1   Initial states

First, we made relativistic molecular-orbital calculations within LDA. The MO obtained by LDA calculations were used as components of Slater determinants in the many-electron calculations. It is generally accepted that the magnitude of covalent bonding between the $3d$ orbital of the transition element and $2p$ orbital of oxygen increases with the increase of the formal charge of the transition element. In order to quantify the trend, Mulliken's population analysis [13] has been made. We found that the atomic-orbital population of O-$2p$ is 3.3%, 7.2%, and 17.6% in t_{2g} for NiO, LiNiO$_2$, and NiO$_2$, respectively. The population is greater in e_g than in t_{2g}, i.e., 14.3%, 30.3%, and 34.8% for NiO, LiNiO$_2$ and NiO$_2$, respectively. The substantial mixing of O-$2p$ in these compounds clearly implies the superiority of using MO instead of AO as components of Slater determinants. Contribution of covalency can be thereby included automatically without implementation of any other scheme. It should be noted that the expressions t_{2g} and e_g are not rigorously right within the relativistic theory (see Fig. 4.1). Instead, the representations of the double group, such as $e_{5/2g}$ and $g_{3/2g}$, should be employed. They are equivalent to $\gamma_{7g}(\gamma_7^+)$ and $\gamma_{8g}(\gamma_8^+)$ using the Bethe symbol. Furthermore, t_{2g} and e_g orbitals split because of the trigonal distortion of the crystal field, since the point group symmetry of the cluster models for LiNiO$_2$ and NiO$_2$ is reduced to D_{3d} symmetry from O_h symmetry. However, the energy splitting in t_{2g} and e_g orbitals because of relativistic effects and trigonal distortion is one-tenth the order of the energy splitting between t_{2g} and e_g, i.e., $10Dq$. Therefore, the expressions t_{2g} and e_g will be adopted in the following part of this thesis for simplicity.

Using the relativistic MO, many-electron calculations were carried out. First, we show the result for the initial states. Considering the orthonormality of the Slater determinants, the composition of the p th Slater determinant in the i th eigenstate is simply given by $|C_{ip}|^2$ where C_{ip} is a expansion. The contributions from several configurations are listed in Table 4.1. In the one-electron scheme, the initial configuration of NiO can be described as 100% $(2p_{1/2})^2(2p_{3/2})^4(t_{2g})^6(e_g)^2$. The result of many-electron calculation shows that the $(2p_{1/2})^2(2p_{3/2})^4(t_{2g})^6(e_g)^2$ contribution is 96.7% for the initial state of NiO. Although we will take account of all configurations for the
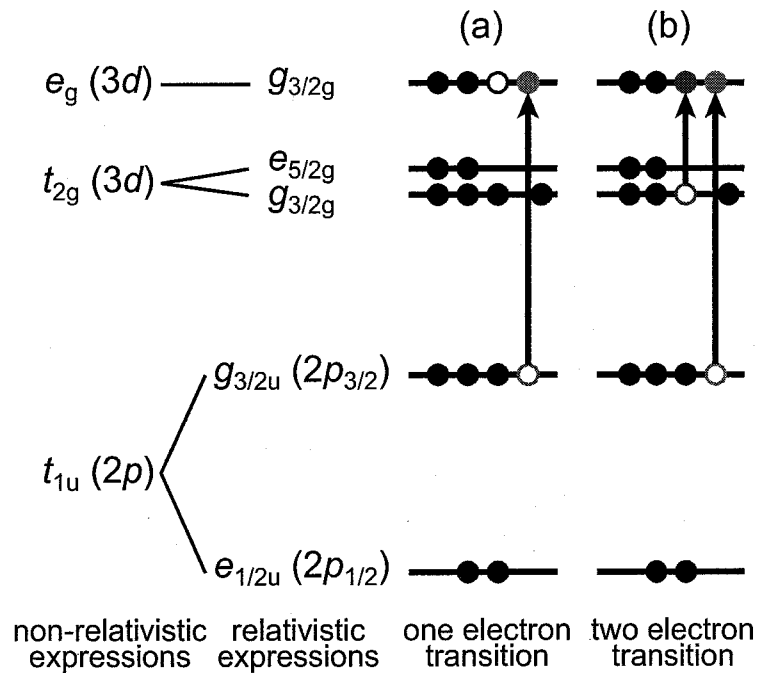
Figure 4.1: Schematic one-electron view of eigenvalues of NiO_6^{10-} in O_h symmetry and two ways for the electronic transition from $2p_{3/2}(g_{3/2u})$ to $e_g(g_{3/2g})$.

NEXAFS calculations to describe the initial state, the $(2p_{1/2})^2(2p_{3/2})^4(t_{2g})^6(e_g)^2$ configuration is found to be predominant, which agrees well with our intuition. Similar many-electron calculations were made for $LiNiO_2$ and NiO_2 imposing several spin configurations. It should be noted that more than 95% of the initial states in all cases are composed of the dominant configuration.

4.3.2 Many-Electron eigenstates and theoretical NEXAFS

NiO

Figure 4.1 schematically shows a one-electron view of eigenvalues of the NiO_6^{10-} cluster and the electronic transition from $2p_{3/2}$ to e_g ($g_{3/2g}$ in the relativistic expression). Since the t_{2g} orbitals also include $g_{3/2g}$ representation when translated into the relativistic expression, two kinds of transitions as shown in Fig. 4.1 need to be considered for L_3 NEXAFS. Their final configurations are $(2p_{1/2})^2(2p_{3/2})^3(t_{2g})^6(e_g)^3$ and $(2p_{1/2})^2(2p_{3/2})^3(t_{2g})^5(e_g)^4$, respectively. A

	$(2p_{1/2})^2(2p_{3/2})^4(t_{2g})^6(e_g)^2$	96.7%
NiO	$(2p_{1/2})^2(2p_{3/2})^4(t_{2g})^5(e_g)^3$	1.8%
	$(2p_{1/2})^2(2p_{3/2})^4(t_{2g})^4(e_g)^4$	1.5%
LiNiO$_2$	$(2p_{1/2})^2(2p_{3/2})^4(t_{2g})^6(e_g)^1$	98.1%
low-spin	$(2p_{1/2})^2(2p_{3/2})^4(t_{2g})^5(e_g)^2$	0.4%
	$(2p_{1/2})^2(2p_{3/2})^4(t_{2g})^4(e_g)^3$	1.5%
LiNiO$_2$	$(2p_{1/2})^2(2p_{3/2})^4(t_{2g})^6(e_g)^1$	0.2%
high-spin	$(2p_{1/2})^2(2p_{3/2})^4(t_{2g})^5(e_g)^2$	96.6%
	$(2p_{1/2})^2(2p_{3/2})^4(t_{2g})^4(e_g)^3$	3.2%
	$(2p_{1/2})^2(2p_{3/2})^4(t_{2g})^6(e_g)^0$	96.7%
NiO$_2$	$(2p_{1/2})^2(2p_{3/2})^4(t_{2g})^5(e_g)^1$	1.8%
low-spin	$(2p_{1/2})^2(2p_{3/2})^4(t_{2g})^4(e_g)^2$	1.5%
	$(2p_{1/2})^2(2p_{3/2})^4(t_{2g})^3(e_g)^3$	0.0%
	$(2p_{1/2})^2(2p_{3/2})^4(t_{2g})^6(e_g)^0$	0.0%
NiO$_2$	$(2p_{1/2})^2(2p_{3/2})^4(t_{2g})^5(e_g)^1$	97.4%
middle-spin	$(2p_{1/2})^2(2p_{3/2})^4(t_{2g})^4(e_g)^2$	2.2%
	$(2p_{1/2})^2(2p_{3/2})^4(t_{2g})^3(e_g)^3$	0.4%
	$(2p_{1/2})^2(2p_{3/2})^4(t_{2g})^6(e_g)^0$	0.0%
NiO$_2$	$(2p_{1/2})^2(2p_{3/2})^4(t_{2g})^5(e_g)^1$	0.1%
high-spin	$(2p_{1/2})^2(2p_{3/2})^4(t_{2g})^4(e_g)^2$	99.6%
	$(2p_{1/2})^2(2p_{3/2})^4(t_{2g})^3(e_g)^3$	0.3%

Table 4.1: Compositions of each configuration in the many-electron wave function corresponding to the initial state of Ni $L_{2,3}$-edge NEXAFS / ELNES.

Core hole	Excited electron	Number of eigenstates	Number of dipole allowed eigenstates	
$g_{3/2u}(2p_{3/2})$	$g_{3/2g}(t_{2g}+e_g)$	32	16	$A_{1u}+A_{2u}+E_u$ $+2T_{1u}+2T_{2u}$
$g_{3/2u}(2p_{3/2})$	$e_{5/2g}(t_{2g})$	8	0	$E_u+T_{1u}+T_{2u}$
$e_{1/2u}(2p_{1/2})$	$g_{3/2g}(t_{2g}+e_g)$	16	8	$E_u+2T_{1u}+T_{2u}$
$e_{1/2u}(2p_{1/2})$	$e_{5/2g}(t_{2g})$	4	0	$A_{2u}+T_{2u}$

Table 4.2: Number of possible transitions and their irreducible representations for four different types of transitions in Ni $L_{2,3}$-edge NEXAFS of NiO_6^{10-} with O_h symmetry.

number of different ways to put a hole in the $2p_{3/2}$ and seven electrons to the $g_{3/2g}$ orbitals is $_4C_1 \times_8 C_7 = 32$, which include both of the two final configurations. Only the transition to $(2p_{1/2})^2(2p_{3/2})^3(t_{2g})^6(e_g)^3$ is allowed as an electric dipole transition. The allowed 16 transitions can be classified as $A_{1u}+A_{2u}+E_u+2T_{1u}+2T_{2u}$ under O_h point group symmetry. The number of transitions and their irreducible representations for the four different types of transitions are summarized in Table 4.2.

Figure 4.2 (a) shows all 60 of the many-electron eigenvalues of the final states using vertical bars. They are classified by colors according to their final configurations. For example, red bars correspond to final configurations of $(2p_{1/2})^2(2p_{3/2})^3(t_{2g})^6(e_g)^3$. Figure 4.2 (b) shows computed oscillator strength of the electric-dipole transition to each eigenstate with black bars. As explained in Table 4.1, the initial states are predominantly composed of $(2p_{1/2})^2(2p_{3/2})^4(t_{2g})^6(e_g)^2$. Therefore, the transitions to final configurations $(2p_{1/2})^2(2p_{3/2})^3(t_{2g})^6(e_g)^3$ [red bars in Fig. 4.2 (a)] and $(2p_{1/2})^1(2p_{3/2})^4(t_{2g})^6(e_g)^3$ [magenta bars in Fig. 4.2 (a)] dominate to the oscillator strengths of Ni $L_{2,3}$ NEXAFS because of the electric dipole selection rule. Figure 4.2 (c) summarizes compositions of those two kinds of final configurations, i.e., $(2p_{1/2})^2(2p_{3/2})^3(t_{2g})^6(e_g)^3$ [red bars in Fig. 4.2 (a)] and $(2p_{1/2})^1(2p_{3/2})^4(t_{2g})^6(e_g)^3$ [magenta bars in Fig. 4.2 (a)]. Theoretical spectrum of the Ni $L_{2,3}$ NEXAFS as shown in top panels was made by broadening the oscillator strengths

using Gaussian functions with the dispersion $\sigma = 0.4$ eV [or full width at half maximum (FWHM) = 0.94 eV]. The oscillator strengths are superposed on the theoretical spectrum with shortened black bars.

Using these diagrams, one can clearly interpret the origin of peaks in the theoretical spectrum. Peak a is composed of eigenstates that can be classified into A_{2u}, E_u, T_{1u}, and T_{2u}. Peak b can be ascribed predominantly to T_{1u}. This shows higher transition energy of peak b than peak a, because the eigenstate corresponding to peak b is a mixture of two configurations as shown in Fig. 4.1. As can be seen in Fig. 4.2 (a), 24% of the contribution is due to the $(2p_{1/2})^2(2p_{3/2})^3(t_{2g})^5(e_g)^4$ [green bars in Fig. 4.2 (a)]. This configuration corresponds to the two electrons excitation shown in Fig. 4.1 (b) and it is not allowed as an electric dipole transition. Although the component does not contribute to the oscillator strength, the mixing of the $t_{2g} \rightarrow e_g$ excitation with the $2p_{3/2} \rightarrow e_g$ excitation makes the transition energy higher than that without such mixing. The small peak c can be ascribed to T_{2u}, which is energetically much more expensive because the major contribution to this eigenstate is the two electrons excitation. The origin of peaks d to f can be interpreted in a similar manner.

LiNiO$_2$

In the case of LiNiO$_2$, the initial configuration is $(2p)^6(\phi_{3d})^7$. Two different spin configurations can be candidates for the initial configuration. One is low-spin configuration, which is mainly composed of $(2p_{1/2})^2(2p_{3/2})^4(t_{2g})^6(e_g)^1$ and the other is high-spin configuration, which is mainly composed of $(2p_{1/2})^2(2p_{3/2})^4(t_{2g})^5(e_g)^2$, as can be seen in Table 4.1. Many-electron calculations were carried out, and 270 final states for Ni $L_{2,3}$ NEXAFS were obtained as shown in Fig. 4.3 (a). They are distinguished by colors according to their final configurations. Since the NiO_6^{9-} cluster in LiNiO$_2$ shows D_{3d} symmetry, two irreducible representations, $E_{1/2u}$ and $E_{3/2u}$, appear in the final states. Depending on the choice of the initial configuration, the dipole transition probability is quite different. When the initial configuration is low spin, i.e., $(2p)^6(t_{2g})^6(e_g)^1$ configuration, only the transition to $(2p)^5(t_{2g})^6(e_g)^2$ is allowed. On the other hand, when the initial configuration is high spin, i.e., $(2p)^6(t_{2g})^5(e_g)^2$ configuration, transition can be allowed to either $(2p)^5(t_{2g})^6(e_g)^2$ or $(2p)^5(t_{2g})^5(e_g)^3$. The contributions from four final configurations are shown in Fig. 4.3. Theo-
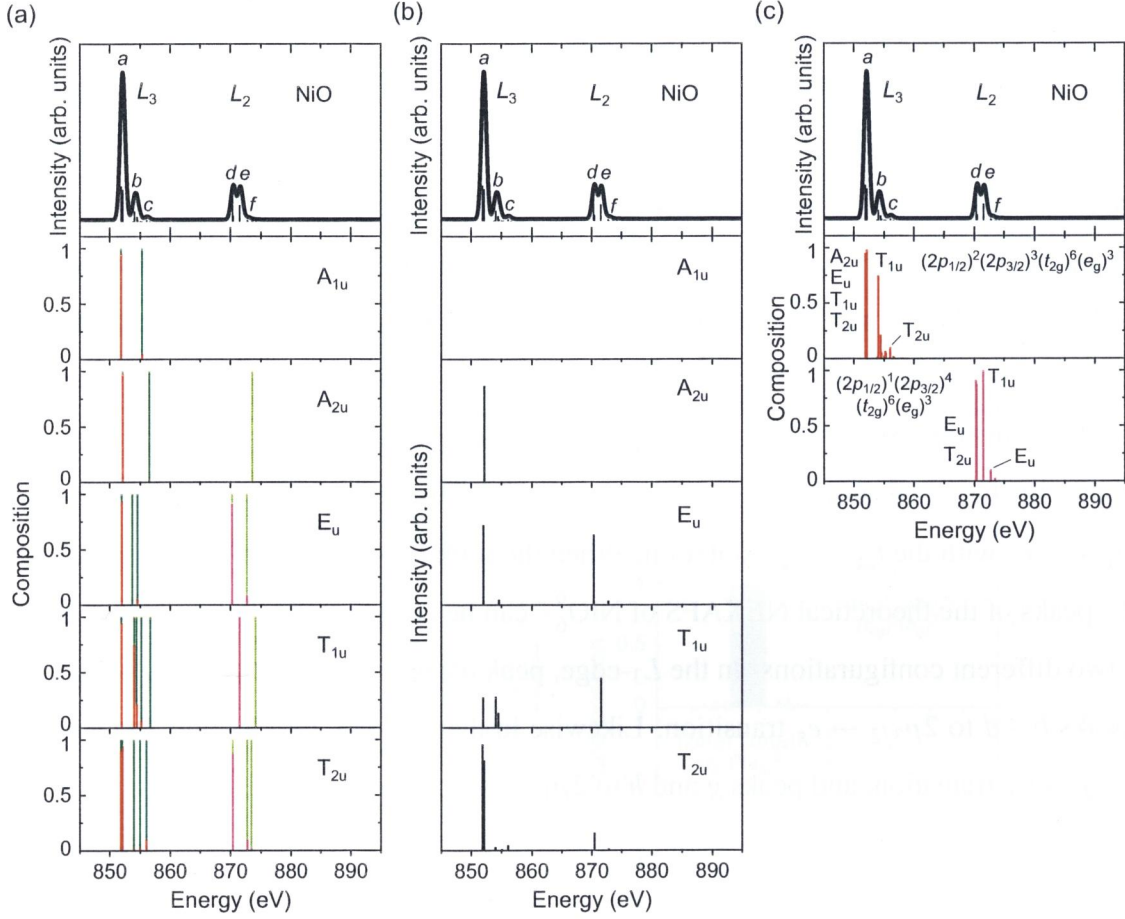
Figure 4.2: (a) Theoretical $L_{2,3}$-edge NEXAFS and ELNES for Ni(II) in NiO is shown in upper panel. Bars in upper panel shows the oscillator strengths for many-electron eigenstates. The following panels show the composition of final configurations for many-electron eigenstates in five symmetries. They are classified according to final configurations as distinguished by colors: red $(2p_{1/2})^2(2p_{3/2})^3(t_{2g})^6(e_g)^3$, green $(2p_{1/2})^2(2p_{3/2})^3(t_{2g})^5(e_g)^4$, magenta $(2p_{1/2})^1(2p_{3/2})^4(t_{2g})^6(e_g)^3$, and yellowish green $(2p_{1/2})^1(2p_{3/2})^4(t_{2g})^5(e_g)^4$. (b) Oscillator strengths for all final states in five symmetries. The lengths of bars were multiplied by 3 from that of the oscillator strengths superimposed on the theoretical spectrum (top panel) for easy visualization. (c) Compositions of final configurations for the dipole allowed transitions, i.e., $(2p_{1/2})^2(2p_{3/2})^3(t_{2g})^6(e_g)^3$ (red bars in a) and $(2p_{1/2})^1(2p_{3/2})^4(t_{2g})^6(e_g)^3$ (magenta bars in a).

retical spectrum of the Ni $L_{2,3}$ NEXAFS was made in the same way as in Fig. 4.2 with dispersion of $\sigma = 0.4$ eV. As can be found from these figures, peaks $a - c$ of the low-spin spectrum can be ascribed to the eigenstates that are predominantly composed of $(2p_{1/2})^2(2p_{3/2})^3(t_{2g})^6(e_g)^2$ [red bars in Fig. 4.3 (a)]. Hence, peaks $a - c$ can be translated as the $2p_{3/2} \rightarrow e_g$ excitation. Eigenstates that are responsible for the tiny peaks, d and e, at higher energies are predominantly composed of $(2p_{1/2})^2(2p_{3/2})^3(t_{2g})^5(e_g)^3$ [green bars in Fig. 4.3 (a)], which is dipole forbidden. They are located much higher in transition energy than peaks $a - c$ because of the mixture of the $t_{2g} \rightarrow e_g$ and $2p_{3/2} \rightarrow e_g$ excitations. A similar analysis can be applied to L_2-edge. Peaks $f - h$ are mainly due to the transition to $(2p_{1/2})^1(2p_{3/2})^4(t_{2g})^6(e_g)^2$ [magenta bars in Fig. 4.3 (a)]. Peaks i and j are higher in energy because their major component is a dipole-forbidden two-electron excitation of $2p_{1/2} \rightarrow e_g$ with the $t_{2g} \rightarrow e_g$ excitation. When the initial configuration is high-spin, both of L_3 and L_2 peaks of the theoretical NEXAFS of NiO_6^{9-} can be categorized into two groups originating from two different configurations. In the L_3-edge, peak a can be ascribed to $2p_{3/2} \rightarrow e_g$ transition, and peaks $b - d$ to $2p_{3/2} \rightarrow e_g$ transition. Likewise in the L_2-edge, peaks e and f can be ascribed to $2p_{1/2} \rightarrow t_{2g}$ transition, and peaks g and h to $2p_{1/2} \rightarrow e_g$ transition.

NiO$_2$

Results for NiO$_2$ using a NiO_6^{8-} cluster with D_{3d} symmetry are summarized in Fig. 4.4. Within the one-electron scheme, only two different spin configurations, i.e., high and low-spin, are possible since the initial configuration is $(2p)^6(\phi_{3d})^6$. On the other hand within the many-electron scheme, some other spin configurations can be taken as initial configurations. An example is a the middle-spin configuration, which is mainly composed $(2p_{1/2})^2(2p_{3/2})^3(t_{2g})^5(e_g)^1$ configuration. Eigenvalues for the 720 final states for Ni $L_{2,3}$ NEXAFS in the three irreducible representations were obtained by the present many-electron calculation. They are distinguished according to their final configurations, as shown in Fig. 4.4 (a). Similar to the other two systems, some mixtures among different configurations can be seen as the overlapping of colored areas. The contributions from the six final configurations are shown in Fig. 4.4 (b). Despite the presence of many final states, theoretical Ni $L_{2,3}$ NEXAFS looks simple when the initial state is low spin. It is composed of two strong peaks, b and e, with tiny satellite peaks. This is because only $(2p_{1/2})^2(2p_{3/2})^3(t_{2g})^6(e_g)^1$
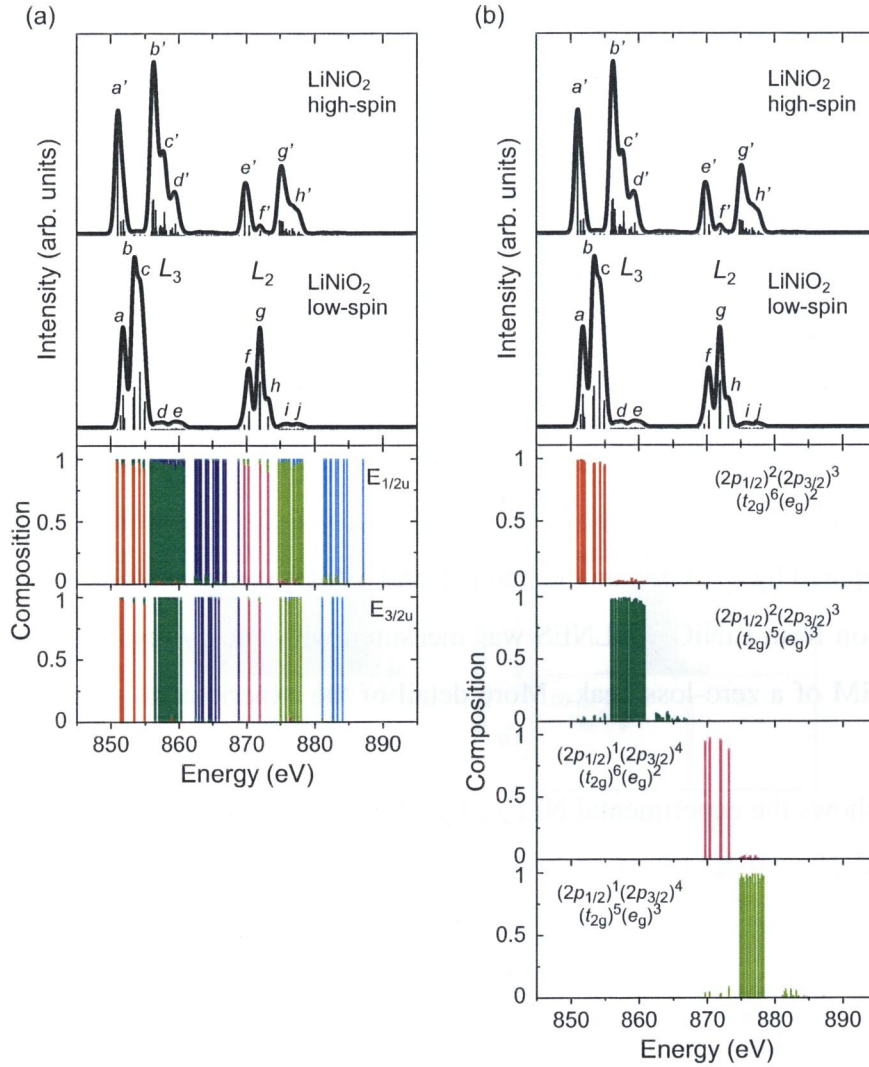
Figure 4.3: (a) Theoretical $L_{2,3}$-edge NEXAFS and ELNES for a low and high-spin states for Ni(III) in LiNiO$_2$ are shown in the upper two panels. The following panels show the composition of final configurations for many-electron eigenstates in $E_{1/2u}$ and $E_{3/2u}$ symmetries. They are classified according to final configurations as distinguished by colors: red $(2p_{1/2})^2(2p_{3/2})^3(t_{2g})^6(e_g)^2$, green $(2p_{1/2})^2(2p_{3/2})^3(t_{2g})^5(e_g)^3$, blue $(2p_{1/2})^2(2p_{3/2})^3(t_{2g})^4(e_g)^4$, magenta $(2p_{1/2})^1(2p_{3/2})^4(t_{2g})^6(e_g)^2$, yellowish green $(2p_{1/2})^1(2p_{3/2})^4(t_{2g})^5(e_g)^3$, and cyan $(2p_{1/2})^1(2p_{3/2})^4(t_{2g})^4(e_g)^4$. (b) Compositions of final configurations for the dipole-allowed transitions.

[red bars in Fig. 4.4 (a)] and $(2p_{1/2})^1(2p_{3/2})^4(t_{2g})^6(e_g)^1$ configurations [magenta bars in Fig. 4.4 (a)] are allowed as an electric dipole transition. On the other hand, two other calculations with different initial states produce completely different theoretical NEXAFS. (Theoretical NEXAFS from the middle-spin state is not shown in Fig. 4.4.) This clearly implies that the $L_{2,3}$ NEXAFS can be used to identify initial electronic states of Ni if reliable theoretical spectra or referential spectra are available.

Comparison to experimental spectra

In order to examine the adequacy of theoretical results obtained in the present study, we conducted ELNES experiments using transmission electron microscopy. Samples were commercial NiO powder, LiNiO₂ prepared by a solid-state method [7], and a NiO₂ sample obtained by electrochemical lithium extraction from LiNiO₂. ELNES was measured with energy resolution ranging from 0.8 to 1.0 eV FWHM of a zero-loss peak. More detail of the experimental procedure can be found elsewhere [14].

Figure 4.5 shows the experimental Ni $L_{2,3}$ ELNES of (a) NiO, (b) LiNiO₂, and (c) NiO₂. The experimental Ni $L_{2,3}$ NEXAFS of NiO with higher energy resolution is also shown below the ELNES for comparison. This spectrum was measured at BL25SU at SPring-8 (Hyogo, Japan), using the same sample as the ELNES measurement. As can be seen, not only the peak positions but also the spectral shapes of these three compounds are discernibly different. This clearly implies that electronic structures of Ni in the three compounds are quite different. Theoretical spectra of the three compounds showing best agreement to experimental spectra are displayed below the corresponding experimental spectra in Fig. 4.5. The energy scales of the theoretical spectra are translated in order to see the best matches with experimental spectra. Because the magnitude of chemical shift from NiO to NiO₂ is slightly overestimated, the magnitudes of translations are 1.9, 1.6, and 1.2 eV, for NiO, LiNiO₂ and NiO₂, respectively. In these theoretical spectra, low-spin states are chosen for LiNiO₂ and NiO₂ as initial states. Spectral shape of these two compounds cannot be explained with the other initial states. We can therefore conclude that the ground state of Ni atoms is Ni(II) in NiO as widely accepted, Ni(III) with low-spin state in LiNiO₂, and Ni(IV) with low-spin state in NiO₂. A remaining problem is a small overestimation of the chemical shift
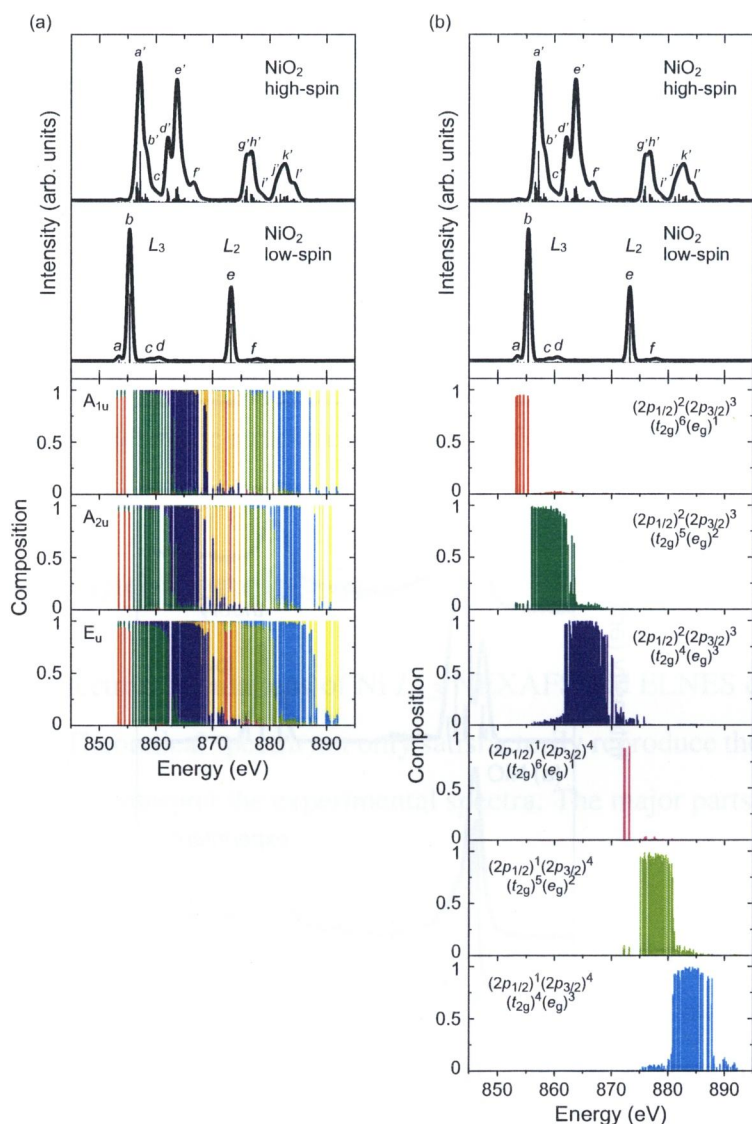
Figure 4.4: (a) Theoretical $L_{2,3}$-edge NEXAFS and ELNES for a low and high-spin states for Ni(IV) in NiO_2 are shown in the upper two panels. The following panels show the composition of final configurations for many-electron eigenstates in A_{1u}, A_{2u}, and E_u symmetries. They are classified according to final configurations as distinguished by colors: red $(2p_{1/2})^2(2p_{3/2})^3(t_{2g})^6(e_g)^1$, green $(2p_{1/2})^2(2p_{3/2})^3(t_{2g})^5(e_g)^2$, blue $(2p_{1/2})^2(2p_{3/2})^3(t_{2g})^4(e_g)^3$, orange $(2p_{1/2})^2(2p_{3/2})^3(t_{2g})^3(e_g)^4$, magenta $(2p_{1/2})^1(2p_{3/2})^4(t_{2g})^6(e_g)^1$, yellowish green $(2p_{1/2})^1(2p_{3/2})^4(t_{2g})^5(e_g)^2$, cyan $(2p_{1/2})^1(2p_{3/2})^4(t_{2g})^4(e_g)^3$, and yellow $(2p_{1/2})^1(2p_{3/2})^4(t_{2g})^3(e_g)^4$. (b) Compositions of final configurations for the dipole-allowed transitions.
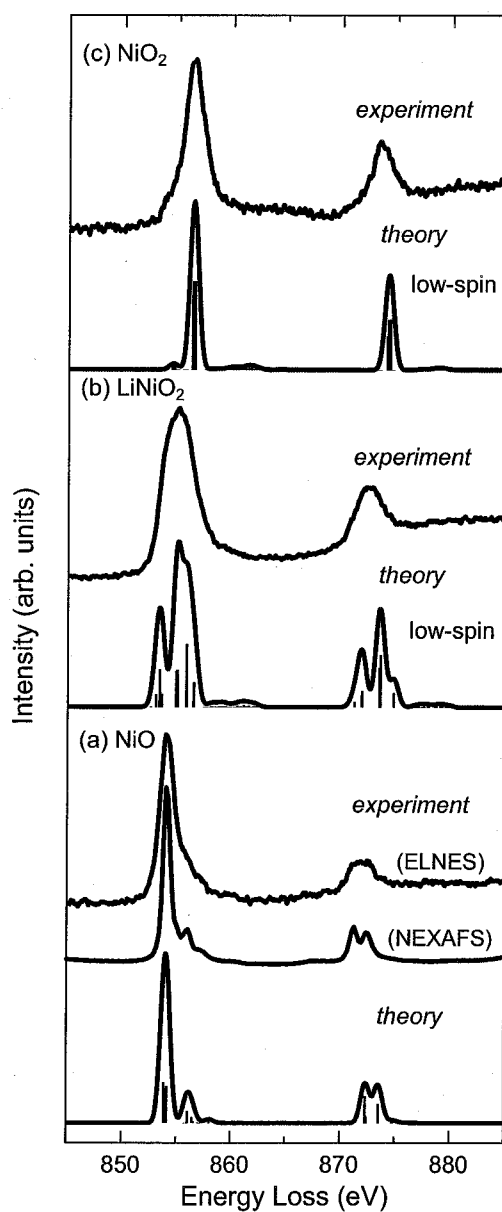
Figure 4.5: Experimental Ni L$_{2,3}$-edge ELNES of (a) NiO, (b) LiNiO$_2$, and (c) NiO$_2$ as compared to theoretical spectra. For NiO, Ni L$_{2,3}$ NEXAFS with a higher energy resolution is also shown to see detailed structures. For theoretical spectra of LiNiO$_2$ and NiO$_2$, low-spin states are chosen as initial states. The absolute transition energy of the theoretical spectrum of NiO, LiNiO$_2$, and NiO$_2$ are shifted by 1.9, 1.6, and 1.2 eV, respectively, in order to see best matches with experimental spectra.

from NiO to NiO_2 by 0.7 eV. This may be ascribed to the use of small clusters in the present calculations, which needs to be clarified in the future. Currently, larger calculations are prohibitively expensive.

Ni $L_{2,3}$ NEXAFS of NiO and $LiNiO_2$ was reported by Montoro *et al.* in 1999 [15]. They found that the NEXAFS of $LiNiO_2$ was similar to that of NiO and concluded that the Ni ions in both of $LiNiO_2$ and NiO were Ni(II). In the present work, ELNES of $LiNiO_2$ is clearly different from that of NiO. The origin of the discrepancy has been discussed in Ref. [14]. The spectra reported in Ref. [15] may reflect the electronic structure at the surface of the sample, but not the bulk.

4.4 Summary and Conclusions

First-principles many-electron calculations of Ni $L_{2,3}$ NEXAFS and ELNES of NiO, $LiNiO_2$, and NiO_2 have been made. Theoretical spectra not only satisfactorily reproduce the experimental spectra, but can also be used to interpret the experimental spectra. The major parts of the present study can be summarized as follows:

1. Relativistic four-component wave functions of molecular orbitals were obtained by solving Dirac equations within the local density approximation using model clusters of NiO_6^{m-}, where m is taken to be 10, 9, and 8 for NiO, $LiNiO_2$, and NiO_2, respectively.

2. Slater determinants composed of all Ni-$2p$ and $3d$ orbitals in NiO_6^{m-} clusters were constructed using the relativistic molecular orbitals. Many-Electron wave functions expressed by a linear combination of the Slater determinants were obtained by diagonalizing the many-electron Hamiltonian. The number of Slater determinants for the initial states was 45, 120, and 210 for NiO, $LiNiO_2$, and NiO_2, respectively. It was, respectively, 60, 270, and 720 for the final states. The eigenstates were analyzed in terms of symmetry and composition of electronic configurations.

3. The contributions of O-$2p$ orbitals through covalency can be automatically included without any other scheme, since the many-electron calculations were made using molecular orbitals

instead of atomic orbitals. This is very important for transition-metal oxides with high formal charges, such as Ni(III) and Ni(IV).

4. Theoretical NEXAFS and ELNES within the electric dipole approximation were obtained by calculating oscillator strengths from several initial states to all of final states. Differences because of the initial states were discussed. The origin of satellite peaks in these spectra was also discussed.

5. Experimental ELNES for the three compounds were satisfactorily reproduced by the present calculations, which unambiguously show that Ni atoms are Ni(III) with a low-spin state in LiNiO$_2$, and Ni(IV) with a low-spin state in NiO$_2$.

References

[1] M. Broussely, P. Biensan, and B. Simon, Electrochim. Acta **45**, 3 (1999).

[2] J. M. Tarascon and M. Armand, Nature **414**, 359 (2001).

[3] M. S. Whittingham, Chem. Rev. **104**, 4271 (2004).

[4] A. L. Ankudinov, A. I. Nesvizhskii, and J. J. Rehr, Phys. Rev. B **67**, 115120 (2003).

[5] P. Krüger and C. R. Natoli, Phys. Rev. B **70**, 245120 (2004).

[6] K. Ogasawara, T. Iwata, Y. Koyama, T. Ishii, I. Tanaka, and H. Adachi, Phys. Rev. B **64**, 115413 (2001).

[7] T. Ohzuku, A. Ueda, and M. Nagayama, J. Electrochem. Soc. **140**, 1862 (1993).

[8] C. Barrett and E. Evans, J. Am. Ceram. Soc. **47**, 533 (1964).

[9] A. Rósen, D. E. Ellis, H. Adachi, and F. W. Averill, J. Chem. Phys. **65**, 3629 (1976).

[10] T. Ishii, K. Ogasawara, H. Adachi, and I. Tanaka, J. Chem. Phys. **115**, 492 (2001).

[11] T. Ishii, M. G. Brik, and K. Ogasawara, J. Alloys Compd. **380**, 136 (2004).

[12] S. Watanabe and H. Kamimura, Mater. Sci. Eng. B **3**, 313 (1989).

[13] R. S. Mulliken, J. Chem. Phys. **23**, 1833 (1955).

[14] Y. Koyama, T. Mizoguchi, H. Ikeno, and I. Tanaka, J. Phys. Chem. B **109**, 10749 (2005).

[15] L. A. Montoro, M. Abbate, E. C. Almeida, and J. M. Rosolen, Chem. Phys. Lett. **309**, 14 (1999).

Chapter 5

Mn $L_{2,3}$-edge NEXAFS studies of Mn doped in Semiconductors

5.1 Introduction

Semiconductors doped with dilute magnetic elements, now referred to as diluted magnetic semi-conductors (DMS), have been extensively studied since the discovery of carrier-induced ferromag-netism in $In_{1-x}Mn_xAs$ [1, 2] and $Ga_{1-x}Mn_xAs$ [3]. However, they are ferromagnetic only at far below the room temperature. A lot of efforts have been devoted to explore systems with higher Curie temperature by changing both dopants and matrix semiconducting materials. The mean-field Zener model has been adopted to explain the ferromagnetism in these systems [4]. Based on the model, room temperature ferromagnetism in Mn-doped GaN and ZnO has been predicted [4]. Supporting this prediction, high T_C above room temperature has been attained in ZnO:Mn [5–7]. However, ferromagnetism with T_C below room temperature [8], paramagnetism [9], and spin-glass behavior [10] were also reported in this system. Additionally, a recent report on ZnO:Mn indicates that the precipitation of Mn results in the disappearance of ferromagnetism [5]. It was also pro-posed that the ferromagnetism appears only when an oxygen-vacancy-stabilized $Mn_{2-x}Zn_xO_{3-\delta}$ phase is present [11]. The reason for such scattering in experimental results can be ascribed to the lack of detailed information on local environment of Mn atoms in the host ZnO. Depending on the

processing conditions, many different scenarios can be made for Mn atoms. They may vary atomic sites, formal charge, nearest-neighbor coordination etc.

GaN:Mn with an extremely high Curie temperature are also reported [12, 13]. The mechanism of ferromagnetism in GaN:Mn has been discussed from a comparative view with GaAs:Mn [14–16]. Dietl *et al.* [17] proposed that the high temperature ferromagnetism in GaN:Mn can be explained within their mean-field Zener model, similar to the case of GaAs:Mn. This model is based on the idea that the Mn^{3+}/Mn^{2+} level is located within or near the valence band and holes are thereby introduced. Mn should be in the charge state of Mn^{2+}. The experimental result by Mn K-edge NEXAFS (near edge x-ray absorption fine structure) [18] was taken as evidence for Mn^{2+} in GaN:Mn. Mn-$L_{2,3}$ NEXAFS doped in GaN [19] seems to support the presence of Mn^{2+}. On the other hand, first principles calculations have predicted that the local electronic structure of Mn in GaN significantly differs from Mn in GaAs [20, 21]. A deep Mn^{3+}/Mn^{2+} level appears in the bandgap in GaN, while the Mn^{3+}/Mn^{2+} state in GaAs is shallow, making a significant overlap between Mn 3d and As 4p valence states. However, a recent first principles study failed to predict high temperature ferromagnetism in GaN:Mn [21]. A typical argument for the unexplained ferromagnetism has been formation of ferromagnetic clusters or segregations. Rao and Jena [22] proposed that the formation of Mn$_x$N type clusters brings about the ferromagnetism through first principles calculations. More recent calculations, however, suggested that such clustering decreases the T_C [23]. It is true that Pearton *et al.*[24] reported that Ga$_x$Mn$_y$ type crystalline secondary phases having T_C exceeding room temperature were found by x-ray diffraction (XRD) in GaN:Mn film (5% Mn) when grown under 'unoptimized' conditions. However, the formation of such clusters has never been verified by XRD in our ferromagnetic samples. The presence of nano-scale ferromagnetic inclusions cannot be ruled out only by the XRD result.

Very recently, the present author's group discovered the room temperature ferromagnetism in Mn-doped Ga$_2$O$_3$. Ga$_2$O$_3$ is known to show a few polymorphs, i.e., $\alpha, \beta, \gamma, \delta$, and ε [13]. They are different not only in their crystal space group but also in the coordination number (CN) of Ga ions. β-Ga$_2$O$_3$ is most commonly available monoclinic crystal, which shows the same number of CN = 4 and CN = 6 sites. γ-Ga$_2$O$_3$ shows a defective spinel structure that is analogous to γ-Al$_2$O$_3$. It also has both CN = 4 and CN = 6 sites. X-ray diffraction and electron diffraction analyses by

transmission electron microscopy (TEM) found that the Mn-doped film shows γ phase with spinel structure. However, local environment and electronic states of Mn atoms in γ-Ga_2O_3 have not yet known.

For the detailed understanding of the magnetic properties, it is essential to know the environment of the doped transition elements on an atomic scale. Near-edge x-ray absorption fine structure (NEXAFS) provides element-specific information of local environment of atoms. Samples for NEXAFS need not be bulk crystals. Nano-crystalline or amorphous materials can also be examined.

In the previous study, the present author's group have examined Mn K-edge NEXAFS of ZnO:Mn samples in order to examine the local environment on an atomic scale [25]. Polycrystalline samples (0.01 - 20at%Mn) and pulse-laser deposited (PLD) films (5at%Mn) on c-plane sapphire have been examined by the combination of experiments and first principles calculations. By x-ray diffraction, Mn was found to dissolve into ZnO up to 5at%Mn in polycrystalline samples sintered at 1623 K in air. Presence of Mn_3O_4 was apparent only for samples with higher Mn content. The c-axis of the ZnO film by the PLD was found to be parallel to the normal of the film. The film also exhibits a single crystalline phase. The Mn K-edge NEXAFS does not change in the range of Mn concentration from 0.01 to 5at%, which implies the absence of any Mn precipitates. First principles APW+lo calculations were made to interpret the experimental spectrum. When a model of substitutional Mn in ZnO with a core-holed supercell of 108 atom is used, the experimental spectrum including its orientation dependence is in good agreement to the theoretical spectrum. Absence of Mn_3O_4 components was also confirmed by the Mn-K NEXAFS. From the Mn K-edge NEXAFS analysis, we have concluded that Mn^{2+} is substitutionally present in ZnO up to 5 at%Mn without significant clustering or ordering.

The $L_{2,3}$-edge NEXAFS provides complimentary information to the K-edge NEXAFS because of the electric dipole selection rule. The K-edge NEXAFS provides information on Mn-p type orbitals. On the other hand, electronic states of Mn-$3d$ orbitals can be analyzed through the $L_{2,3}$ NEXAFS. The latter should be more important for discussion of the electronic mechanism behind the magnetism in DMS.

TM $L_{2,3}$-edge NEXAFS spectra can be calculated by DFT-CI method. As shown in Chap. 3

and 4, experimental spectra from many compounds having different d-electron numbers and coordination numbers have been successfully reproduced by explicitly dealing with electronic correlations only among $3d$ electrons and a $2p$ hole. On adopting this computational approach to the Mn $L_{2,3}$-edge NEXAFS of Mn oxides, we have recognized that the reproduction of the experimental spectra by theory is qualitatively satisfactory but not perfect. If one wants to use the Mn $L_{2,3}$-edge NEXAFS to characterize the local environment of Mn atoms, it should be able to distinguish not only different charged states but also different coordination numbers. The theoretical tool should have predictive performance of such information.

In this chapter, we have examined Mn $L_{2,3}$-edge NEXAFS of ZnO:Mn samples that have already been well characterized in our previous study. Then theoretical calculations using the many-electron approach with different levels of approximations have been conducted. We have eventually found that the experimental spectrum of the ZnO:Mn sample can be quantitatively well predicted by the present calculation to detail. Combining such elaborate theoretical calculations, one can distinguish Mn(II) with different coordination numbers. Then we have adopted the new method to identify the physical and chemical states of Mn atoms in GaN and Ga_2O_3.

5.2   Experimental Procedure

The ZnO:Mn, GaN:Mn and Ga_2O_3:Mn were used for samples of Mn $L_{2,3}$-edge NEXAFS measurements.

Samples are the same as that used in our previous study [25]. Polycrystalline specimens of ZnO:5at%Mn were fabricated by mixing of MnO_2 with ZnO powder followed by sintering in air at 1623 K for 3 h and cooling in air at 225 K/h. The ZnO-5at%Mn thin film was prepared by a pulsed laser deposition (PLD) using an excimer KrF* laser source (λ = 248 nm, τ = 25 ns) on Al_2O_3(0001) single crystal substrate, which was kept at 873 K during the deposition. The film thickness was approximately 100 nm.

GaN:Mn films in the present study were grown by molecular beam epitaxy using NH_3 as nitrogen source. The procedure is the same as those reported in earlier papers [12, 26]. Here we report results for thicker films such as 1 μm and higher Mn concentrations up to 8.2 at.% as

determined by electron probe microanalyser (EPMA). The XRD results show that these films are highly oriented along the c-axis of wurtzite structured GaN, and does not exhibit any crystalline secondary phases even in the 8.2 at.% Mn film.

Ga_2O_3:Mn thin films were prepared on Al_2O_3 (0001) single crystals by PLD method using an excimer KrF^* laser source. PLD targets with Mn were fabricated by mixing of commercially available high-purity powder of MnO_2 with Ga_2O_3 powder followed by sintering in air at 1623 K for 3 hour. The concentration of Mn of doped PLD sample was measured by energy dispersive x-ray spectroscopy equipped to a scanning electron microscope and a transmission electron microscope (TEM). Both of them found an identical result, i.e., 7 cation % of Mn. The phases and crystal structure of thin films were analyzed by means of XRD and TEM which revealed that Mn-doped β-Ga_2O_3 is epitaxially grown on the Al_2O_3 (0001) with orientation along β-Ga_2O_3 (111) direction [27].

Mn $L_{2,3}$-edge NEXAFS measurements of ZnO:Mn and GaN:Mn were performed on the ALS (Advanced Light Source, Berkeley) BL8.0.1 at room temperature. Data were acquired in total electron yield mode, measuring the photoelectron current emitted from the specimen surface by a ammeter connected to the sample holder. The energy calibration was made using the Mn $L_{2,3}$-edge of Mn_3O_4 as a standard. The photon energy resolution was set to 0.1 eV during the measurements. Mn $L_{2,3}$-edge NEXAFS of Mn-doped Ga_2O_3 were measured at BL11A in KEK-PF, Tsukuba, Japan using total electron yield method at room temperature. The photon energy resolution was set to 0.1 eV, and Mn_3O_4 was treated as an internal calibration standard.

5.3 Computational Procedure

Both ZnO and GaN host materials have the wurtzite type structure. Zn/Ga ions are four-fold coordinated by O/N ions in this structure. For the calculation of Mn $L_{2,3}$-edge NEXAFS, we assumed that the Mn ions are substituting Zn/Ga ions. Local atomic arrangement around the Mn dopant was optimized by the plane-wave psudo-potential method (CASTEP code) [28] using 72 atoms supercell as shown in Fig. 5.1 (a). Then the MnX_4^{m-} cluster models which are composed of a Mn dopant and nearest-neighbor X ions were constructed from optimized structures, where $X =$

host	ZnO	GaN		Ga$_2$O$_3$ (spinel)	
Formal charge of Mn	Mn(II)	Mn(II)	Mn(III)	Mn(II)	Mn(II)
Cluster model	MnO$_4^{6-}$	MnN$_4^{10-}$	MnN$_4^{9-}$	MnO$_4^{6-}$	MnO$_6^{10-}$
Point group	C_3	C_3	C_3	T_d	C_3
Mn-X(1) (nm)	0.2034	0.2077	0.1998	0.2045	0.2179
Mn-X(2) (nm)	0.2055	0.2081	0.2037		0.2186

Table 5.1: Formal charge of Mn, point group symmetry and atomic distance between central Mn and ligand $X = $ O, N of cluster models.

O, N for ZnO and GaN, respectively. The total number of electrons in the cluster was obtained from formal charges ions. In GaN:Mn system, we have considered both Mn(II) and Mn(III) impurities.

The γ-Ga$_2$O$_3$ has a defective spinel structure, in which the 1/9 of cation sites of perfect spinel are vacant. It this structure, Ga ions are located on both four-fold and six-fold coordinated site. Since Ga ions and vacancies are randomly arranged, it is difficult to construct a γ-Ga$_2$O$_3$ crystalline model. In the present work, we took MnGa$_2$O$_4$ spinel structure as a reference system that were optimized by a first-principles projector augmented wave method [29] using VASP code [30–32]. A normal spinel structure has all Mn(II) at the CN=4 site, which was used for the MnO$_4^{6-}$ model (Fig. 5.1 (b)). One of Mn in the 56-atoms unit cell was exchanged with a furthest Ga atom in order to make the atomic configuration of the MnO$_6^{10-}$ model (Fig. 5.1 (c)).

The cluster model used were summarized in Table 5.1. In order to take account of effective Madelung potential, an array of point charges was put at the external atomic sites of clusters using the method proposed by Evjen [33].

Firstly, fully relativistic molecular orbital (MO) calculations were carried out by solving Dirac equations with the local density approximation (LDA) using the code that was originally described in Ref. [34]. In this code, four-component relativistic MO are expressed as linear combination of atomic orbitals (LCAO). The numerically generated four-component relativistic atomic orbitals ($1s$–$4p$ for Mn and $1s$–$2p$ for O/N) were used as basis functions for MO.

After one-electron MO calculations of relativistic MO, the many-electron calculation were
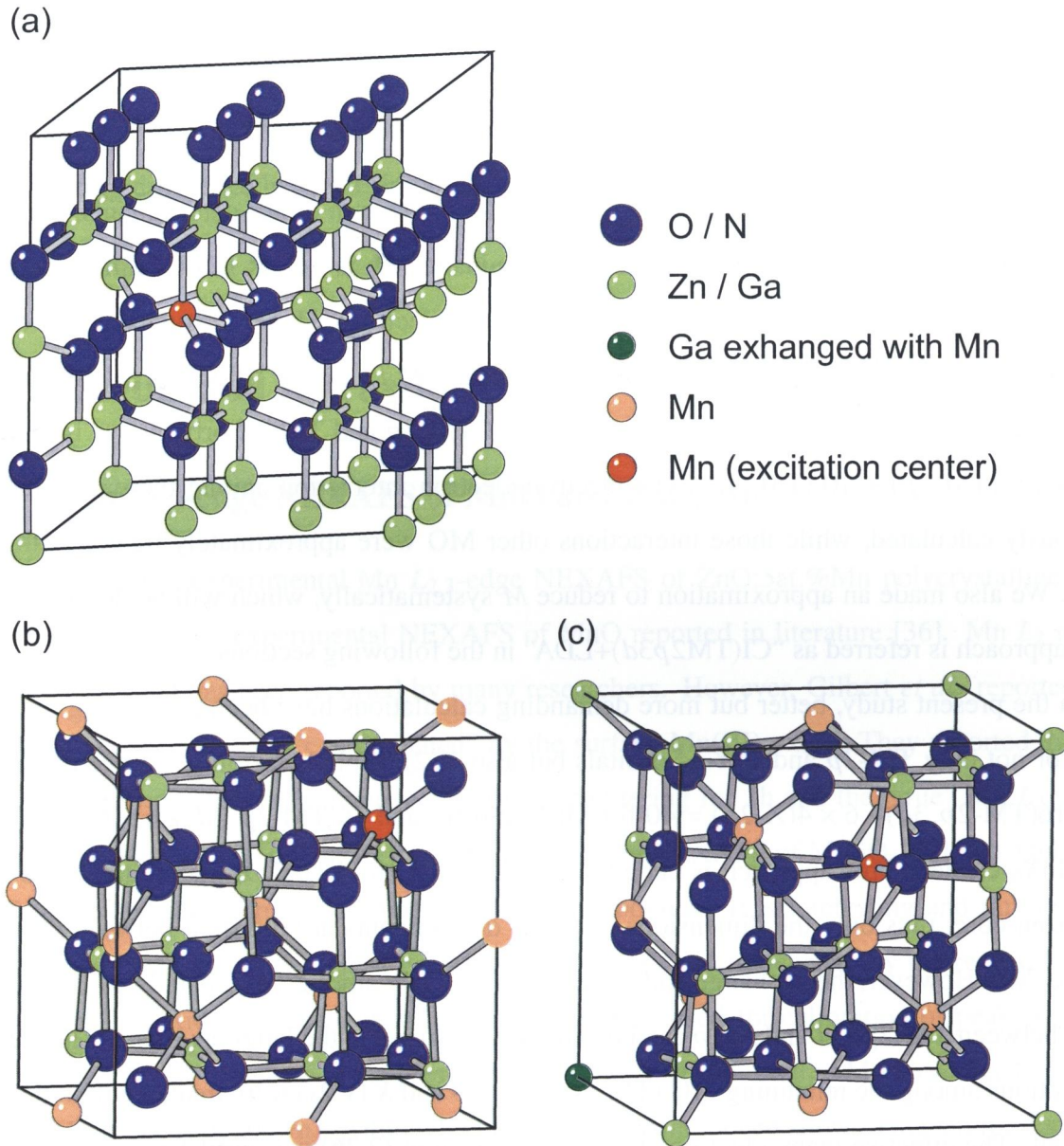
Figure 5.1: Atomic arrangement of (a) $(Zn_{31}MnO_{32})$ / $(Ga_{31}MnN_{32})$ supercell, (b) $Mn_8Ga_{16}O_{32}$ unit cell of $MnGa_2O_4$ normal spinel and (c) $(Mn_7Ga)(Ga_{15}Mn)O_{32}$ unit cell where one of Mn (red ball) was exchanged with a furthest Ga atom (dark green ball). Cluster models composed of excitation center Mn (red ball) and nearest-neighbor O / N atoms were constructed after geometry optimization.

carried out within the DFT-CI scheme. Many-electron wave functions were formed by linear combination of Slater determinants given by

$$\Psi_i = \sum_{p=1}^{M} C_{ip} \Phi_p \qquad (5.1)$$

where Φ_i is the i th many-electron wave function, Φ_p is the p th Slater determinants, and C_{ip} is coefficient. The maximum number of Slater determinants, M, is $_mC_n$ at full-CI limit where m is the number of MO for the cluster and n is the number of electrons. However, such calculations are prohibitively expensive when L is large. In our previous TM $L_{2,3}$-edge NEXAFS calculations, the MO were restricted to be those mainly composed of TM $2p$ and TM $3d$ orbitals. m is therefore 16, i.e., 6 (TM-$2p$) + 10 (TM-$3d$). The electron-electron interaction among these orbitals were rigorously calculated, while those interactions other MO were approximately treated within the LDA. We also made an approximation to reduce M systematically, which will be described later. This approach is referred as "CI(TM$2p3d$)+LDA" in the following sections.

In the present study, better but more demanding calculations have been done using the set of MO for not only TM-$2p$ and TM-$3d$ orbitals but also X-$2p$ orbitals forming valence bands, i.e., m is 16(TM-$2p$,$3d$)+ 6 × 4(X-$2p$) = 40 for MnX$_4$ cluster and 16(TM-$2p$,$3d$)+ 6 × 6(X-$2p$) = 52 for MnX$_6$ cluster. This approach is called "CI(TM$2p3d$-X$2p$)+LDA". X-$2p$ orbitals were taken as frozen core, thus only the dimensions of Slater determinants are different between these two approaches. However, the exchange and correlations not only among TM-$2p$ and TM-$3d$, but also those between TM-$2p$, $3d$ and X-$2p$ can be explicitly included in the latter approach. The electron interactions among the remaining MO (TM $1s, 2s, 3s, 3p$ and $X 1s, 2s$) were treated within the LDA as usual. The effective many-electron Hamiltonian given in (2.26) was used.The explicit form of v_0 was derived by Watanabe and Kamimura [35].

Mn $L_{2,3}$-edge NEXAFS of Mn(II) compound is due to the transitions from $(2p)^6(\phi_{3d})^5$ to $(2p)^5(\phi_{3d})^6$, where ϕ_{3d} denotes the MO mainly composed of Mn $3d$ orbitals. The number of the Slater determinants for $(2p)^6(\phi_{3d})^5$ is $252(=_6 C_6 \times_{10} C_5)$ and that for $(2p)^5(\phi_{3d})^6$ is $1260(=_6 C_5 \times_{10} C_6)$. Thus 1512 Slater determinants were used as bases for many-electron wave functions. For Mn(III) compound, the number of Slater determinants for $(2p)^6(\phi_{3d})^4$ is $210(=_6 C_6 \times_{10} C_4)$ and that for $(2p)^5(\phi_{3d})^5$ is $1512(=_6 C_5 \times_{10} C_5)$. 1722 Slater determinants were therefore

used. The same number of Slater integrals were used for "CI(TM$2p3d$)+LDA" and "CI(TM$2p3d$-X$2p$)+LDA" approaches.

The oscillator strength of the electric dipole transition averaged over all directions were calculated using eq. (2.31). The overestimation of absolute transition energy was corrected by taking orbital-energy difference between single-electron orbitals for the Slater's transition-state as a reference.

5.4 Results and Discussion

5.4.1 Mn $L_{2,3}$-edge NEXAFS of MnO and ZnO:Mn

Fig. 5.2 (a) shows experimental Mn $L_{2,3}$-edge NEXAFS of ZnO:5at.%Mn polycrystalline sample. It is compared to experimental NEXAFS of MnO reported in literature [36]. Mn $L_{2,3}$-edge NEXAFS of MnO has been reported by many researchers. However, Gilbert et al. reported that most of these spectra were "contaminated" by the surface Mn(III) oxides They reported that the surface Mn(III) oxides can be removed by Ar ion sputtering for 1h and the "true" Mn $L_{2,3}$-edge NEXAFS of MnO can be obtained. Its shape matches the NEXAFS of MnSO$_4$[37] and MnF$_2$[38] which are other octahedrally coordinated Mn(II) compounds. It is interesting and important to note that the position of the highest peak located at 640eV did not change by the removal of the surface Mn(III) oxide. It means that the peak top can be used for calibration of peak positions obtained in different samples. In the present study we have also measured Mn $L_{2,3}$-edge NEXAFS of a MnO sample (not shown). Although our MnO spectrum indeed shows a signature of surface Mn(III) oxide, we use the peak position of our MnO spectrum for calibration. As can be seen, these two spectra resemble to each other. However, careful inspection can find small differences as follows: 1) The shoulder peak A in the L_3 edge is higher in MnO. 2) Peaks C and D are look steeper in ZnO:Mn. 3) Separation of peaks E and F in the L_2 edge is clearer in ZnO:Mn. If one can reproduce such small differences, the theoretical calculation can be considered to have predictive performance. Then the combination of experiment and theoretical calculation can be used to identify local environment of Mn atoms.

Many-electron calculations were carried out with two different levels of approximation, i.e., "CI(Mn2p3d)+LDA" and "CI(Mn2p3d-O2p)+LDA". For the ZnO:Mn, a substitutional Mn(II) at a Zn site of ZnO was used. The configuration analysis results for many-electron calculation reveals that the $(2p_{1/2})^2(2p_{3/2})^4(e)^2(t_2)^3$ contributions is 97% for the initial state of Mn $L_{2,3}$-edge NEXAFS: this means that the initial state is dominated by the high-spin configurations. For MnO spectra, MnO$_6^{10-}$ cluster with octahedral symmetry was used. The $(2p_{1/2})^2(2p_{3/2})^4(t_{2g})^2(e_g)^3$ contribution is 99% for initial state which indicates that the initial state is also dominated by high-spin state. The lower panel of Fig. 5.2 (a) and (b) show theoretical NEXAFS by the many-electron approach for ZnO:Mn and MnO with "CI(Mn2p3d)+LDA" and "CI(Mn2p3d-O2p)+LDA" approaches. Spectral shapes of ZnO:Mn by two approaches look almost same. Tiny difference can be found only for the position and relative intensity of satellite peaks. Such difference by two approaches become more clear in case of MnO. The value of the those difference can be understood by comparing the theoretical spectra with experimental one. Experimental spectra are much better reproduced by the "CI(Mn2p3d-O2p)+LDA" approach. Differences between two samples in three points as described above are also very well reproduced when the "CI(Mn2p3d-O2p)+LDA" approach is used. Such a good agreement unambiguously implies that the Mn atoms in ZnO are present at the substitutional site with high-spin state making MnO$_4^{6-}$ units.

In non-cubic systems, orientation dependence of NEXAFS may provide information on anisotropic properties of crystals. In our previous study, clear orientation dependence was observed by Mn K-edge NEXAFS of wurtzite ZnO:5at%Mn thin film when measured with $c//E$ and $c \perp E$ geometry, where c and E are c-axis direction of the hexagonal crystal and electric field vector of the x-ray [25]. Theoretical calculations clearly reproduced the orientation dependence. The orientation dependence of Mn $L_{2,3}$-edge NEXAFS of the ZnO:5at%Mn thin film was also measured in the same manner. Results are shown in Fig. 5.3 together with the theoretical spectra by the "CI(Mn2p3d-O2p)+LDA" approach. As can be realized, there is no visible difference between two experimental spectra for two orientations. The same is true for the theoretical spectra. It may be almost impossible to find any orientation dependence of the Mn $L_{2,3}$-edge NEXAFS for Mn atoms substitutinally present in wurtzite ZnO.
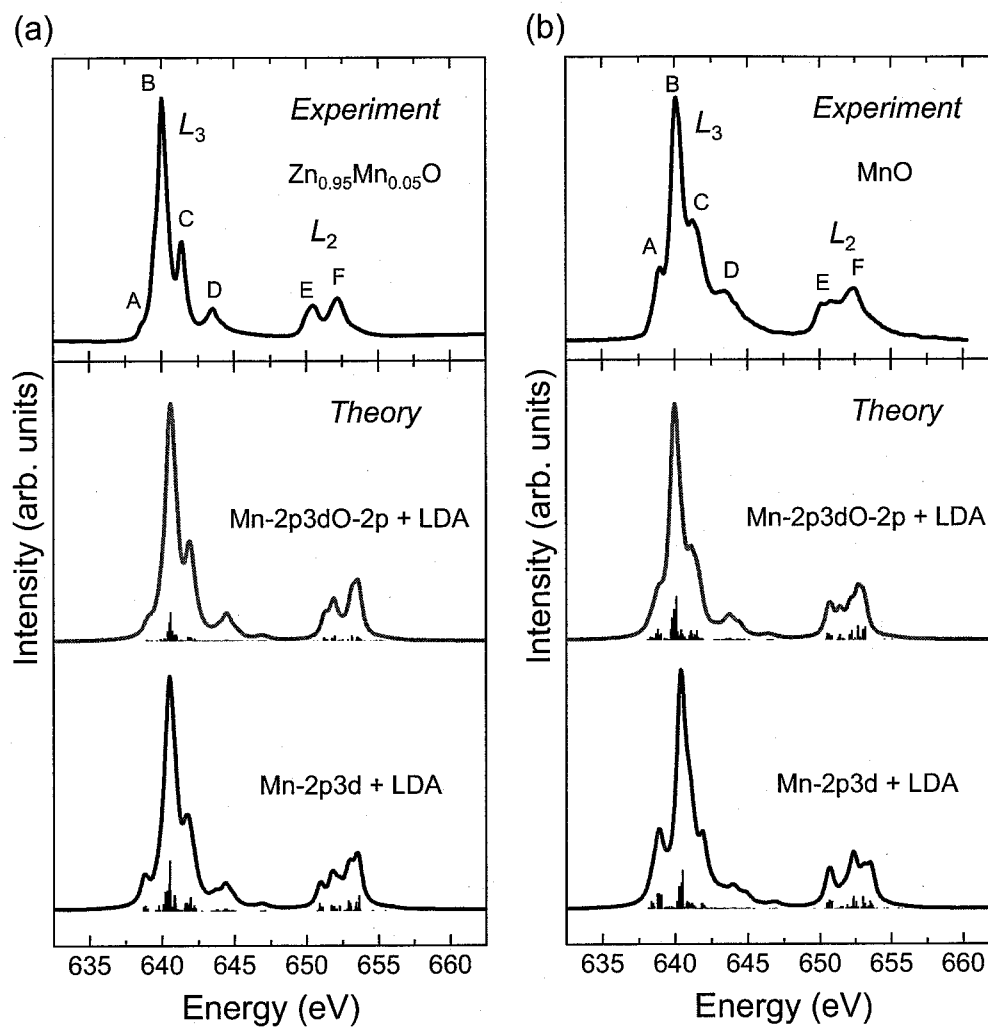
Figure 5.2: (a) Theoretical Mn $L_{2,3}$-edge NEXAFS of ZnO:Mn calculated by "CI(Mn$2p3d$)+LDA" approach (bottom) and "CI(Mn$2p3d$-O$2p$)+LDA" approach (middle) compared with experimental one (top). (b) Same as (a) but for MnO. Experimental spectrum of MnO is reprinted in part with permission from Ref. [36]. Copyrighted (2007) American Chemical Society.
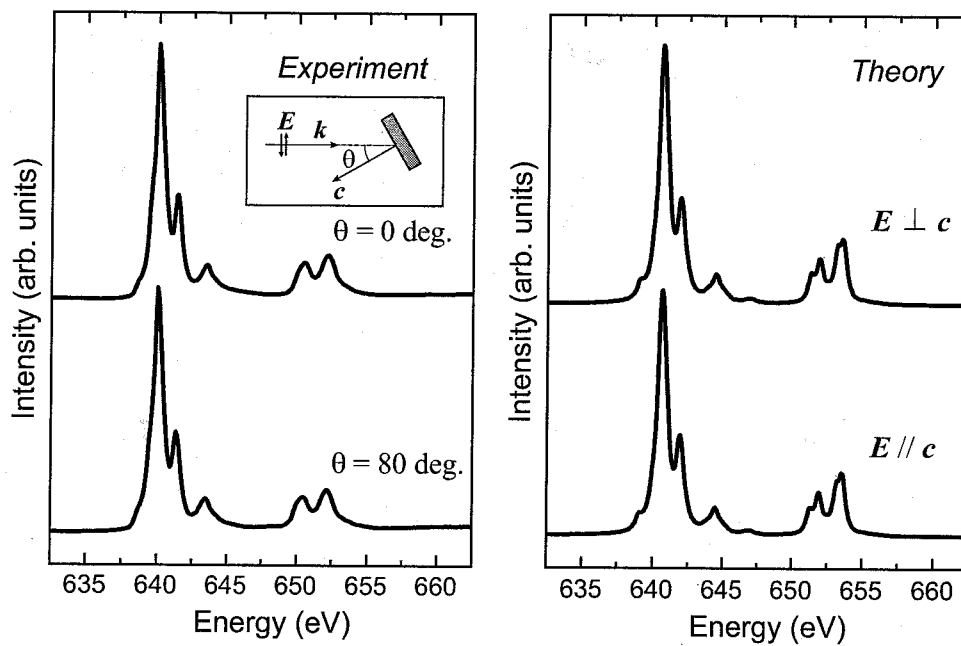
Figure 5.3: Orientation dependence of Mn $L_{2,3}$-edge NEXAFS of $Zn_{0.95}Mn_{0.05}O$ thin film. c and E are c-axis direction of the hexagonal crystal and electric field respectively. The inset in left panel shows the experimental geometry.

5.4.2   Mn $L_{2,3}$-edge NEXAFS of GaN:Mn

The Mn $L_{2,3}$-edge NEXAFS measurements were performed for GaN:Mn thin films with different Mn concentrations. All samples show ferromagnetism at room temperature. The shape of the spectrum is found to be independent of the Mn concentration. A typical spectrum shown in Fig. 5.4 is the same as that reported by Edmonds *et al.* [19] for GaN:3at%Mn. However, no detailed information on the properties of their sample was available. No interpretation of the spectrum was provided, either, except that the valence state of Mn is +2, based on fingerprints of some Mn compounds.

In the present study, we have applied the "CI(Mn$2p3d$-N$2p$)+LDA" approach for more detailed analysis of Mn $L_{2,3}$-edge NEXAFS. A Mn atoms is possibly trivalent in GaN, since the formal charge of a Ga atom in GaN is Ga(III). Hence, two different models which a Mn(II) and a Mn(III) atom substituting a Ga site of GaN were considered. MnN$_4^{10-}$ and MnN$_4^{9-}$ model were taken corresponding to Mn(II) and Mn(III), respectively. The lower panel of Fig. 5.4 shows the theoretical Mn(II) and Mn(III) $L_{2,3}$-edge NEXAFS in GaN by "CI(Mn$2p3d$-N$2p$)+LDA" approach. The results of configuration analysis for many-electron eigenstates revealed that the initial states of Mn $L_{2,3}$-edge NEXAFS are high-spin state in these two models. The initial state of Mn(II) in GaN predominantly composed of $(2p_{1/2})^2(2p_{3/2})^4(e)^2(t_2)^3$ configuration. The contributions of this configuration is more than 96%. In the case of Mn(III) in GaN, the $(2p_{1/2})^2(2p_{3/2})^4(e)^2(t_2)^2$ contributions is more than 98% for the initial state. The oscillator strength of electric dipole transitions from these initial states were calculated and broadened by Lorentzian functions with FWHM = 0.6eV to obtain theoretical spectra. Significant difference in spectral shapes can be found between these two theoretical spectra due to the difference of formal charge of Mn atoms. Chemical shift on L_3-edge are also clearly shown. Therefore, Mn(II) and Mn(III) in GaN can be recognized by taking these spectra as theoretical fingerprinting. Comparison of theoretical spectra with experimental ones shows that the majority of Mn atoms are substitutionally dissolved into GaN as Mn(II). Similar comparison has been made for Mn $L_{2,3}$ NEXAFS of ZnO:5at%Mn, that shows no ferromagnetism at room temperature, in Fig. 5.2 (a). Excellent agreement between experimental and theoretical spectra with Mn(II) can be seen in ZnO:Mn. A small but clear difference between

experimental spectra of ZnO:Mn and GaN:Mn is recognized at the small satellite peak as indicated by arrows in Fig. 5.4. This can be ascribed to the presence of the Mn(III) component only in GaN:Mn. Indeed, the experimental spectrum of GaN:Mn is better reproduced when 15% of Mn atoms are assumed to be in the +3 state. The difference between magnetic properties of ZnO:Mn and GaN:Mn can be ascribed to the presence of the Mn(III) component. The existence of Mn(III) in present samples were also confirmed by optical absorption spectra [39].

5.4.3 Mn $L_{2,3}$-edge NEXAFS of γ-Ga$_2$O$_3$:Mn

Fig. 5.5 shows the experimental Mn $L_{2,3}$-edge NEXAFS of ferromagnetic spinel Ga$_2$O$_3$:Mn thin film. The peak position of the present sample is the same as those of MnO and ZnO:Mn, implying that Mn(II) is dominant. The shoulder peak at the left-hand side of L_3-edge spectrum of MnO, labeled A in Fig. 5.2 (b), is absent in this sample as well as ZnO:Mn. As discussed above, Mn in the ZnO:Mn sample was identified to be substitutional at Zn site, showing CN of 4. This is in contrast to MnO with rocksalt structure with CN = 6. The experimental spectrum of this Ga$_2$O$_3$:Mn film is therefore suggestive of Mn(II) with CN = 4. In order to confirm the idea, many-electron calculations have been made using two clusters, i.e., MnO$_4^{6-}$ and MnO$_6^{10-}$, which correspond to Mn(II) with CN = 4 and CN = 6. Mn $L_{2,3}$-edge NEXAFS were calculated by "CI(Mn2p3d-O2p)+LDA" approach. Similar to the ZnO:Mn and MnO, the initial states of Mn $L_{2,3}$-edge spectra are high-spin state in both CN = 4 and CN = 6. The oscillator strength of electric dipole transitions were calculated. They were broadened by Lorentzian functions with FWHM = 0.6eV. The obtained spectra are shown in the lower panel of Fig. 5.5. As can be found by the comparison between theoretical and experimental spectra, Mn(II) in the spinel Ga$_2$O$_3$ is most likely present at the CN=4 site. This is quite natural, since MnGa$_2$O$_4$ is known to prefer a normal spinel structure [40].
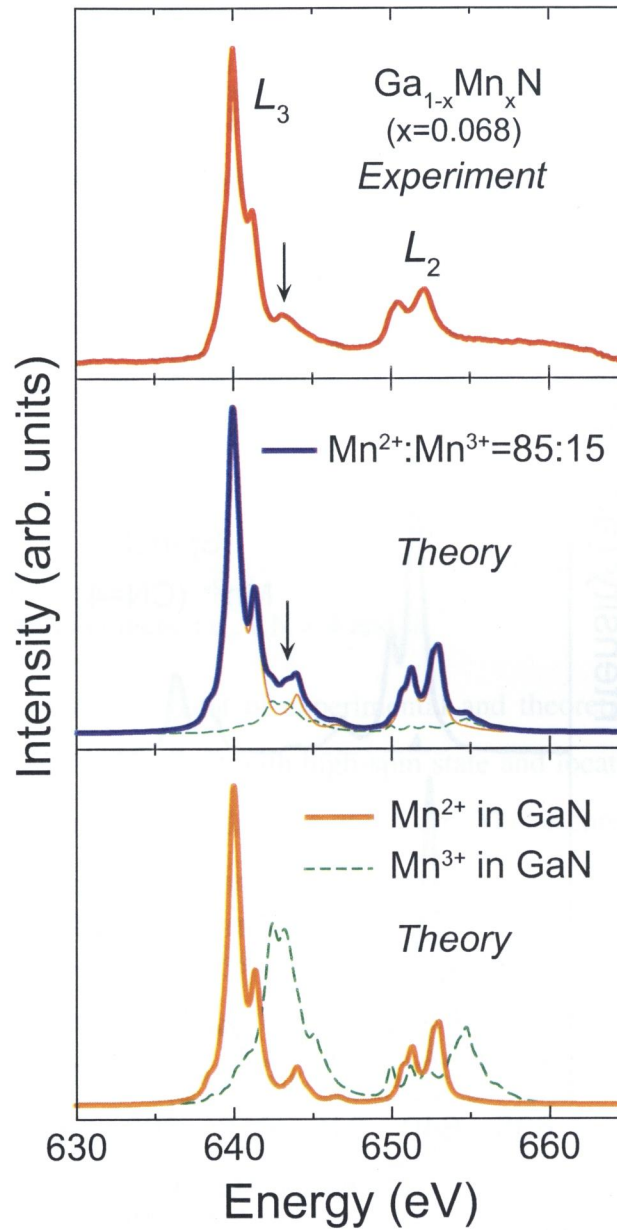
Figure 5.4: (a) Mn $L_{2,3}$-edge NEXAFS of Mn-doped (Mn 6.8%) thin film. The top panel shows an experimental spectrum. The bottom one presents calculated spectra for Mn^{2+} (orange) and Mn^{3+} (green) using the "Mn$2p3d$-N$2p$+LDA" approach. The middle one is composed of 15% of Mn(III) and 85% of Mn(II) calculated spectra, which shows the best agreement to the experimental spectrum.
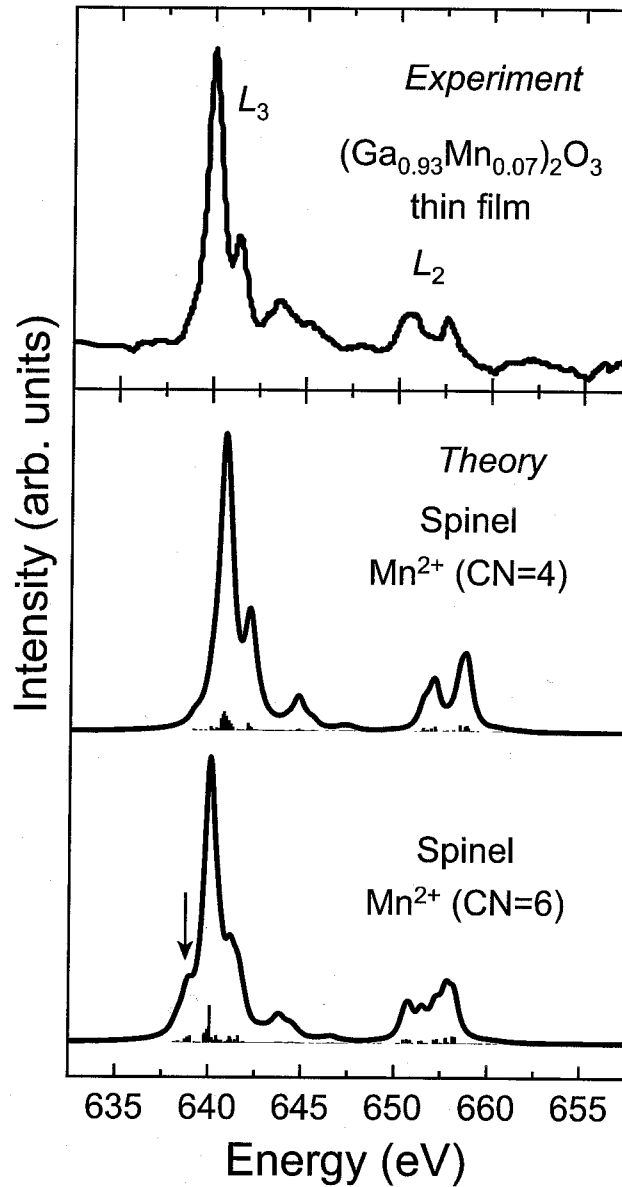
Figure 5.5: (upper panel) Experimental Mn $L_{2,3}$-edge NEXAFS of $(Ga_{0.93}Mn_{0.07})_2O_3$ thin film. (lower panel) Theoretical Mn $L_{2,3}$-edge NEXAFS of Mn^{2+} (CN=4) and Mn^{2+} (CN=6) in spinel $MnGa_2O_4$ calculated by "$Mn2p3d$-$O2p$+LDA" approaches. Solid bars in lower panel show many-electron eigenvalues and corresponding oscillator strengths. The arrows indicate the shoulder peak that is a signature of CN=6.

5.5 Conclusions

Local environment of Mn atoms doped in ZnO, GaN and Ga_2O_3 were investigated using Mn $L_{2,3}$-edge NEXAFS. First principles many-electron calculations of Mn $L_{2,3}$-edge NEXAFS in above three host semiconductors were made with increasing approximation levels. Major results can be summarized as follows:

1. Experimental spectra of MnO and ZnO:Mn are well reproduced by the many-electron calculations without any adjustable parameters. The agreement is better when the dimension of Slater determinants is increased to include O-$2p$ orbitals, i.e., the "CI(Mn$2p3d$-O$2p$)+LDA" approach than the "CI(Mn$2p3d$)+LDA" approach.

2. Using this method with predictive performance, one can clearly distinguish Mn(II) with different coordination numbers, i.e., CN = 4 and 6.

3. Judging from the good agreement of experimental and theoretical spectra, Mn atoms in ZnO:5at.%Mn sample are divalent with high-spin state and located at substitutional cation site of ZnO forming four-fold coordination of oxygen. This is consistent with the conclusion in our previous study by Mn K-edge NEXAFS.

4. Although ZnO forms hexagonal crystal, Mn $L_{2,3}$-edge NEXAFS shows little dependence on crystallographic orientation by experiment. This is also confirmed by theoretical calculations. This is contrary to the large dependence in the Mn K-edge NEXAFS.

5. Mn $L_{2,3}$-edge NEXAFS of GaN:Mn thin films which are ferromagnetic at room temperature were systematically measured. Spectral shape is independent of Mn concentration up to 8.2%.

6. Comparison of experimental and theoretical spectra of GaN:Mn shows that majority of Mn atoms are divalent with high-spin state and substitutionally located at Ga site of GaN forming four-fold coordination of nitrogen.

7. A small but clear difference between experimental spectra of ZnO:Mn and GaN:Mn is recognized at the small satellite peak on L_3-edge. Better reproduction of GaN:Mn spectra can

be obtained when 15% of Mn atoms are assumed to be in the trivalent state, which suggests the coexistence of Mn(II)/Mn(III) in GaN.

8. Experimental and theoretical Mn $L_{2,3}$-edge NEXAFS in spinel Ga_2O_3 revealed that Mn atoms are divalent with high-spin state. Most of Mn(II) atoms are located on the four-fold coordination site of oxygen, which is consistent the fact that Mn atoms prefers tetrahedral site in $MnGa_2O_4$ spinel structure.

References

[1] H. Munekata, H. Ohno, S. Vonmolnar, A. Segmüller, L. L. Chang, and L. Esaki, Phys. Rev. Lett. **63**, 1849 (1989).

[2] H. Ohno, H. Munekata, T. Penney, S. von Molnár, and L. L. Chang, Phys. Rev. Lett. **68**, 2664 (1992).

[3] H. Ohno, A. Shen, F. Matsukura, A. Oiwa, A. Endo, S. Katsumoto, and Y. Iye, Appl. Phys. Lett. **69**, 363 (1996).

[4] T. Dietl, H. Ohno, F. Matsukura, J. Cibert, and D. Ferrand, Science **287**, 1019 (2000).

[5] P. Sharma, A. Gupta, K. V. Rao, F. J. Owens, R. Sharma, R. Ahuja, J. M. O. Guillen, B. Johansson, and G. A. Gehring, Nat. Mater. **2**, 673 (2003).

[6] S.-W. Lim, M.-C. Jeong, M.-H. Ham, and J.-M. Myoung, Jpn. J. Appl. Phys., Part 2 **43**, L280 (2004).

[7] Y. W. Heo, M. P. Ivill, D. P. Norton, K. Ip, S. J. Pearton, J. G. Kelly, R. Rairigh, A. F. Hebard, and T. Steiner, Appl. Phys. Lett. **86**, 2292 (2004).

[8] S. W. Jung, S. J. An, G.-C. Yi, C. U. Jung, S.-I. Lee, and S. Cho, Appl. Phys. Lett. **80**, 4561 (2002).

[9] S. S. Kim, J. H. Moon, B.-T. Lee, O. S. Song, and J. H. Je, J. Appl. Phys. **95**, 454 (2005).

[10] T. Fukumura, Z. W. Jin, M. Kawasaki, T. Shono, T. Hasegawa, S. Koshihara, and H. Koinuma, Appl. Phys. Lett. **78**, 958 (2001).

[11] D. C. Kundaliya, S. B. Ogale, S. E. Lofland, S. Dhar, C. J. Metting, S. R. Shinde, Z. Ma, B. Varughese, K. Ramanujachary, L. Salamanca-Riba, et al., Nat. Mater. **3**, 709 (2004).

[12] S. Sonoda, S. Shimizua, T. Sasakib, Y. Yamamotob, and H. Hori, J. Cryst. Growth **237-239**, 1358 (2002).

[13] M. L. Reed, N. A. El-Masry, H. H. Stadelmaier, M. K. Ritums, M. J. Reed, C. A. Parker, J. C. Roberts, and S. M. Bedair, Appl. Phys. Lett. **79**, 3473 (2001).

[14] L. Kronik, M. Jain, and J. R. Chelikowsky, Phys. Rev. B **66**, 041203 (2002).

[15] E. Kulatov, H. Nakayama, H. Mariette, H. Ohta, and Y. A. Uspenskii, Phys. Rev. B **66**, 045203 (2002).

[16] B. Sanyal, O. Bengone, and S. Mirbt, Phys. Rev. B **68**, 205210 (2003).

[17] T. Dietl, F. Matsukura, and H. Ohno, Phys. Rev. B **66**, 033203 (2002).

[18] Y. L. Soo, G. Kioseoglou, S. Kim, S. Huang, Y. H. Kao, S. Kuwabara, S. Owa, T. Kondo, and H. Munekata, Appl. Phys. Lett. **79**, 3926 (2001).

[19] K. W. Edmonds, N. R. S. Farley, T. K. Johal, R. P. Campion, B. L. Gallagher, C. T. Foxon, and G. van der Laan, J. Appl. Phys. **95**, 7166 (2004).

[20] K. Sato and H. Katayama-Yoshida, Semicond. Sci. Technol. **17**, 367 (2002).

[21] K. Sato, W. Schweika, P. H. Dederichs, and H. Katayama-Yoshida, Phys. Rev. B **70**, 201202 (2004).

[22] B. K. Rao and P. Jena, Phys. Rev. Lett. **89**, 185504 (2002).

[23] L. M. Sandratskii, P. Bruno, and S. Mirbt, Phys. Rev. B **71**, 045210 (2005).

[24] S. J. Pearton, C. R. Abernathy, G. T. Thaler, R. M. Frazier, D. P. Norton, F. Ren, Y. D. Park, J. M. Zavada, I. A. Buyanova, W. M. Chen, et al., J. Phys.: Condens. Matter **16**, R209 (2004).

[25] M. Kunisu, F. Oba, H. Ikeno, I. Tanaka, and T. Yamamoto, Appl. Phys. Lett. **86**, 121902 (2005).

[26] H. Hori, S. Sonoda, T. Sasaki, Y. Yamamoto, S. Shimizu, K.-i. Suga, and K. Kindo, Phys. B **324**, 142 (2002).

[27] H. Hayashi, R. Huang, H. Ikeno, F. Oba, S. Yoshioka, I. Tanaka, and S. Sonoda, Appl. Phys. Lett. **89**, 181903 (2006).

[28] V. Milman, B. Winkler, J. A. White, C. J. Pickard, M. C. Payne, E. V. Akhmatskaya, and R. H. Nobes, Int. J. Quantum Chem. **77**, 895 (2000).

[29] P. E. Blöchl, Phys. Rev. B **50**, 17953 (1994).

[30] G. Kresse and J. Hafner, Phys. Rev. B **48**, 13115 (1993).

[31] G. Kresse and J. Furthmuller, Phys. Rev. B **54**, 11169 (1996).

[32] G. Kresse and J. Furthmuller, Comput. Mat. Sci. **6**, 15 (1996).

[33] H. M. Evjen, Phys. Rev. **39**, 675 (1932).

[34] A. Rósen, D. E. Ellis, H. Adachi, and F. W. Averill, J. Chem. Phys. **65**, 3629 (1976).

[35] S. Watanabe and H. Kamimura, Mater. Sci. Eng. B **3**, 313 (1989).

[36] B. Gilbert, B. H. Frazer, A. Belz, P. G. Conrad, K. H. Nealson, D. Haskel, J. C. Lang, G. Srajer, and G. De Stasio, J. Phys. Chem. A **107**, 2839 (2003).

[37] J. Rothe, E. M. Kneedler, K. Pecher, B. P. Tonner, K. H. Nealson, T. Grundl, W. Meyer-Ilse, and T. Warwick, J. Synchrotron Rad. **6**, 359 (1999).

[38] J. Kawai, Y. Mizutani, T. Sugimura, M. Sai, T. Higuchi, Y. Harada, Y. Ishiwata, A. Fukushima, M. Fujisawa, M. Watanabe, et al., Spectrochim. Acta B **55**, 1385 (2000).

[39] S. Sonoda, I. Tanaka, H. Ikeno, T. Yamamoto, F. Oba, T. Araki, Y. Yamamoto, K. Suga, Y. Nanishi, Y. Akasaka, et al., J. Phys.: Condens. Matter **18**, 4615 (2006).

[40] B. Boucher, A. G. Herpin, and A. Oles, J. Appl. Phys. **37**, 960 (1966).

Chapter 6

All Electron Relativistic Configuration Interaction Calculations for $3d$ $L_{2,3}$-edge NEXAFS

6.1 Introduction

The importance of transition metal (TM) $L_{2,3}$-edge NEXAFS has been recognized since the early time in the ELNES/XANES history. Chemical shifts and intensity ratio of $L_3/(L_2 + L_3)$ peaks, i.e., branching ratio, have been correlated to the valency and magnetic moment of the TM ions [1–6]. When spectral features specific to compounds are evident, they can be used to identify the local environment of the TM elements in a sample of interest. This is called the fingerprinting technique. However, the method relies entirely on empirical knowledge. It is useful only when good reference samples are abundantly available. We risk making a wrong interpretation unless a reliable non-empirical way to produce the spectra for a given atomic, electronic, and magnetic structures is established.

In previous three chapters, we applied the hybrid method of density functional theory and configuration interaction (DFT-CI) for $3d$ -TM $L_{2,3}$-edge NEXAFS calculations. First-principles molecular orbital calculations were made using model clusters. Electronic correlations among

$3d$ electrons and a $2p$ hole were rigorously calculated by taking all Slater determinants made by the molecular orbitals (MO). Experimental spectra from many compounds having different d-electron numbers and coordination numbers have been successfully reproduced without any empirical parameters. The agreement between experimental and theoretical spectra is better when the dimension of Slater determinants is increased to include ligand $2p$ orbitals, i.e., the electronic correlations between ligand $2p$ and $3d$ electrons or $2p$ core-hole are explicitly calculated. When comparing carefully, however, one can find the transition energy difference between L_3-edge and L_2-edge, which is mainly ascribed to the spin-orbit splitting in core $2p$ level, is overestimated in theoretical spectrum calculated by DFT-CI. For instance, In Mn $L_{2,3}$-edge NEXAFS of MnO, the magnitude of overestimation is 0.7 eV (See, Fig. 5.2). Such overestimation in DFT-CI method can be ascribed to the poor description of approximated potentials form other than Mn-$2p$, $3d$ and ligand $2p$ electrons especially in excited state. In this approach, the core-hole effects are not included to these potentials. Though core-hole effects should differ when a core-hole exist in $2p_{1/2}$ or $2p_{3/2}$, such difference does not taken into account to ensure the orthonormality of molecular orbitals (MO) for CI calculation. That causes the discrepancy in L_3-L_2 transition energy difference. Moreover, the magnitude of overestimation will change when different exchange-correlation potentials are chosen. Such potential dependencies makes this method less predictive especially for light transition metal $L_{2,3}$-edge NEXAFS, since it may change overlap between L_3-edge and L_2-edge and hence change spectral features. Therefore, more robust computational method, which is independent of choice of potentials and can include core-hole effects properly, is required.

Recently, we have developed all electron relativistic configuration interaction code based on 'no-pair' Hamiltonian given in (2.14) with $V_{ee} = 1/r_{ij}$ are taken as electron-electron interactions, which is usually referred as Dirac-Coulomb Hamiltonian. Electronic correlations among all electrons are rigorously calculated. Now the effective one-electron potentials are not included in many-electron Hamiltonian, and problems related to potential dependency can be avoided by this method.

In theoretical viewpoint, however, the relativistic effects on electron-electron interactions are not included in Dirac-Coulomb Hamiltonian. Coulomb interaction operator neither contains any relativistic interactions between electrons and nor Lorentz invariant are taken as electrons interaction. Hence this Hamiltonian is correct only to the order of α^0, where α denotes the fine structure

constant. The first relativistic correction to the Coulomb interaction is the Breit term [7, 8], which is the largest term next to the instantaneous Coulomb interaction in the quantum electrodynamics [9, 10], and its zero-frequency form given as

$$B(i,j) = -\frac{1}{2r_{ij}} \left\{ \boldsymbol{\alpha}_i \cdot \boldsymbol{\alpha}_j + \frac{(\boldsymbol{\alpha}_i \cdot \boldsymbol{r}_{ij})(\boldsymbol{\alpha}_j \cdot \boldsymbol{r}_{ij})}{r_{ij}^2} \right\}.$$ (6.1)

The Breit term contains the magnetic interactions introduced via the orbital and spin motions (which is also called Gaunt term [11]), and the retardation effect. Including Breit interactions into electron-electron interactions leads to the best description of Lorentz invariance in relativistic interactions, and increases accuracy of calculated fine structure splittings, inner-electron binding energy [12–15]. Because the Breit term is of the order of $(v/c)^2$ compared to the non-relativistic interaction term, the contribution of Breit term will increase as the average velocity of an electron v increase. Thus, Breit interaction becomes large in core electrons. The contribution of relativistic interactions will be larger on $2p_{1/2}$ than $2p_{3/2}$, since the averaged velocity of electrons are larger on $2p_{1/2}$, and result in the reduction of L_3-L_2 transition energy difference.

In this chapter, we apply all electron CI method based on 'no-pair' Dirac-Coulomb-Breit Hamiltonian to compute $L_{2,3}$-edge NEXAFS TM mono-oxide having rocksalt structure, i.e., CoO, FeO, MnO, and TiO, and investigate the effects of Breit interactions on NEXAFS spectra.

6.2　Computational Procedure

First-principles multi-electron calculations were made using model clusters composed of one TM ion or Ca ion and coordinating six oxide ions. The total number of electrons in the cluster was obtained from formal charges. Therefore the clusters can be expressed as TMO_6^{10-}. Atomic positions were obtained from the experimental crystal structures. Lattice constants are summarized in Table 6.1. In order to take account of effective Madelung potential, an array of point charges was put at the external atomic sites of clusters using the method proposed by Evjen [16]. First, fully relativistic molecular orbital calculations were carried out by solving Dirac equations with the local density approximation (LDA) using the code that was originally described in Ref. [17]. In this code, four-component relativistic MO are expressed as linear combination of atomic orbitals

(LCAO). The numerically generated four-component relativistic atomic orbitals ($1s$–$4p$ for TM and Ca and $1s$–$2p$ for O, total 96) were used as basis functions for MO.

After the one-electron calculations of relativistic MO, all electron configuration interaction (CI) calculations were performed taking 'no-pair' Dirac-Coulomb-Breit Hamiltonian. Breit interaction was included as a first order perturbation. Many-electron wave functions were formed by linear combination of Slater determinants. In order to reduce the number of Slater determinants, only metal $2p$ orbitals and MO mainly composed of metal $3d$ atomic orbitals are taken as active space, i.e., only the configuration obtained by changing the occupation in this space were used to expand many-electron wave functions.

The number of Slater determinants are summarized in Table 6.1. For example in MnO, the transitions from $(Mn2p)^6(\phi_{Mn3d})^5$ to $(Mn2p)^2(\phi_{Mn3d})^6$ are responsible for Mn $L_{2,3}$-edge NEXAFS, where ϕ_{Mn3d} denotes the MO mainly composed of Mn-$3d$ orbitals. The number of the Slater determinants for $(Mn2p)^6(\phi_{Mn3d})^5$ is $252(=_6C_6 \times_{10}C_5)$ and that for $(Mn2p)^2(\phi_{3d})^6$ is $1260(=_6C_5 \times_{10}C_6)$. Thus 1512 Slater determinants were used as bases for many-electron wave functions. The rest of configurations included in $(Mn2p)^4(\phi_{Mn3d})^7$ $(Mn2p)^3(\phi_{Mn3d})^8$, $(Mn2p)^2(\phi_{Mn3d})^9$, and $(Mn2p)^1(\phi_{Mn3d})^{10}$ were not considered. Thus the number of Slater determinants was reduced from $_{96}C_{83}$ in full-CI to 1512, which allows us to perform the calculations within an acceptable computational time. In quantum chemistry terminology, this truncation method of Slater determinants is called restricted active space (RAS) CI [18]. The six metal $2p$ orbitals were classified in RAS I where at least five electrons were occupied. Ten MO mainly composed of metal $3d$ orbitals were classified into RAS II, where no restriction for occupation in this class. MO mainly composed of metal $4sp$ were taken as virtual orbitals, i.e, deleted from CI calculations, and other MO were taken as frozen core. Exchange and correlation interactions between metal $2p$, $3d$ electrons and frozen core electrons are explicitly included in this method. Correlations among frozen core electrons are neglected but they are expected to be much smaller than those among metal $2p$, $3d$ electrons in present case.

The oscillator strength of the electric dipole transition averaged over all directions were calculated using eq. (2.31). The overestimation of absolute transition energy was corrected by taking orbital-energy difference between single-electron orbitals for the Slater's transition-state as a ref-

	CoO	FeO	MnO	TiO
Formal number of d electrons	d^7	d^6	d^5	d^2
Lattice constant (nm)	0.4252	0.4236	0.4442	0.4177
Number of Initial	120	210	252	45
Slater Final	270	720	1260	720
determinants Total	390	930	1512	765

Table 6.1: Lattice constants, formal number of d electrons and number of Slater determinants for TM $L_{2,3}$-edge NEXAFS of TM mono-oxides

erence. Theoretical spectrum was made by broadening the oscillator strengths using Lorentzian functions.

6.3 Results and Discussion

6.3.1 TM $L_{2,3}$-edge NEXAFS and Branching Ratio

Fig. 6.1 and Fig. 6.2 shows theoretical spectra of four compounds in comparison with the experimental spectra taken from Refs. [19, 20]. Experimental data for TiO is not available in literature by the authors' best efforts. The solid bars drawn with theoretical spectra indicate the oscillator strength computed by eq. (2.31). They are broadened by Lorentzian functions with FWHM = 0.6 eV for CoO, FeO, MnO and FWHM = 0.8 eV for TiO to obtain theoretical spectra. Theoretical spectra show good agreements with experimental one. Relative intensity and position of subpeaks are well reproduced, except the small underestimation of L_3-L_2 energy separation on FeO and MnO. Separation of the L_3 and L_2 peaks decreases with the decrease in atomic number of TM, which can be ascribed to weaker spin-orbit coupling. At the same time, the intensity ratio of $L_3/(L_2 + L_3)$, i.e., the branching ratio decreases. Theoretical branching ratios are shown in Fig. 6.3. In order to obtain a branching ratio that can be compared to experimental spectra, the

CoO	$(2p_{1/2})^2(2p_{3/2})^4(t_{2g})^5(e_g)^2$	87.8%
	$(2p_{1/2})^2(2p_{3/2})^4(t_{2g})^4(e_g)^3$	12.1%
FeO	$(2p_{1/2})^2(2p_{3/2})^4(t_{2g})^4(e_g)^2$	99.3%
	$(2p_{1/2})^2(2p_{3/2})^4(t_{2g})^3(e_g)^3$	0.3%
MnO	$(2p_{1/2})^2(2p_{3/2})^4(t_{2g})^3(e_g)^2$	99.3%
	$(2p_{1/2})^2(2p_{3/2})^4(t_{2g})^4(e_g)^1$	0.5%
TiO	$(2p_{1/2})^2(2p_{3/2})^4(t_{2g})^2(e_g)^0$	96.0%
	$(2p_{1/2})^2(2p_{3/2})^4(t_{2g})^1(e_g)^1$	4.0%

Table 6.2: Compositions of the two dominant configurations in the many-electron wave functions based on Dirac-Coulomb-Breit Hamiltonian that corresponds to the initial state of TM $L_{2,3}$-edge NEXAFS. Only one configuration contribute to the initial state of Ca $L_{2,3}$-edge NEXAFS.

theoretical spectra were fitted to two Lorentzian functions. The peak area obtained in this way was used as the intensities of L_2 and L_3 peaks.

The origin of peaks in theoretical spectra can be discussed through analyses of many-electron eigenstates. First, results for initial states are discussed. In the one-electron scheme, an initial state can be described by a single Slater determinant. In the many-electron scheme, on the other hand, an initial state is described by the linear combination of multiple Slater determinants. Then the mixture of multiple configurations or CI can be taken into account to describe the initial state more accurately. Considering the orthonormality of the Slater determinants, the composition of the p th Slater determinant in the i th eigenstate is simply given by $|C_{ip}|^2$ where C_{ip} is a expansion. The contributions from two dominant configurations to the initial state are listed in Table 6.2. As can be seen, the composition of $(2p_{1/2})^2(2p_{3/2})^4(t_{2g})^2(e_g)^0$ configuration is 96.0% for the initial state of TiO. Note that the 72 frozen core MO which mainly composed of TM-$1s, 2s, 3s, 3p$, O-$1s$ or $2s$ are fully occupied, but not explicitly shown for simplicity. The predominance of one configuration exceeds 99 also for MnO and FeO. However it is only 87.8% in CoO, which means that the CI are significant in CoO. The use of one electron scheme leads to a large error in such a case even for the initial state. For the present NEXAFS calculations we have used the many-electron scheme

and all configurations have been adopted to describe the initial state. In all there compounds, the predominant configuration for the initial state is "high spin state" in the one-electron terminology. This is in good agreement to the experimental results.

Many final states contribute to theoretical NEXAFS. For example the number of final states is 720 for TiO and 1260 for MnO as can be seen in Table 6.1. This is the reason for the presence of widely spread multiplet structures in the spectra. The final states can be classified into different configurations as shown in lower panels of Fig. 6.1 and 6.2. In TiO for example, only electronic transitions to $(2p_{1/2})^2(2p_{3/2})^3(t_{2g})^3(e_g)^0$ and $(2p_{1/2})^2(2p_{3/2})^3(t_{2g})^2(e_g)^1$ are allowed by electric dipole selection rule to make the L_3-edge transition assuming that the initial state is only composed of $(2p_{1/2})^2(2p_{3/2})^4(t_{2g})^2(e_g)^0$ contribution. Two contributions, $(2p_{1/2})^2(2p_{3/2})^3(t_{2g})^3(e_g)^0$ and $(2p_{1/2})^2(2p_{3/2})^3(t_{2g})^2(e_g)^1$, overlap in the same energy range significantly. Therefore it is not possible to assign experimental peaks according to the electronic configuration. The same is true for the other compounds. The subpeaks originate entirely from the multiplet effects.

It is important to note that the final states responsible for L_3 and L_2 peaks overlap in the energy range between 455 to 465 eV in TiO. This is the reason why the branching ratio in TiO is much smaller than the statistically averaged value of $2/(2 + 1) = 0.667$ that occurs when neither L_3-L_2 overlap nor many-electron correlations and the spin-orbit coupling in $3d$ orbitals are present. Smaller but not negligible overlap between L_3 and L_2 peaks can be found in MnO in the energy around 650 eV.

The branching ratio obtained in the present study is compared with theoretical values obtained by van der Laan *et al.* in 1991 using an atomic multiplet program for an isolated ion embedded in the crystal field of octahedral symmetry [4]. They have adopted empirical parameters to include crystal field splitting and covalency. The present result agrees well with their values for "high spin" configurations that were obtained by fitting to experimental spectra. The present calculations can produce almost the same results without any empirical parameters.
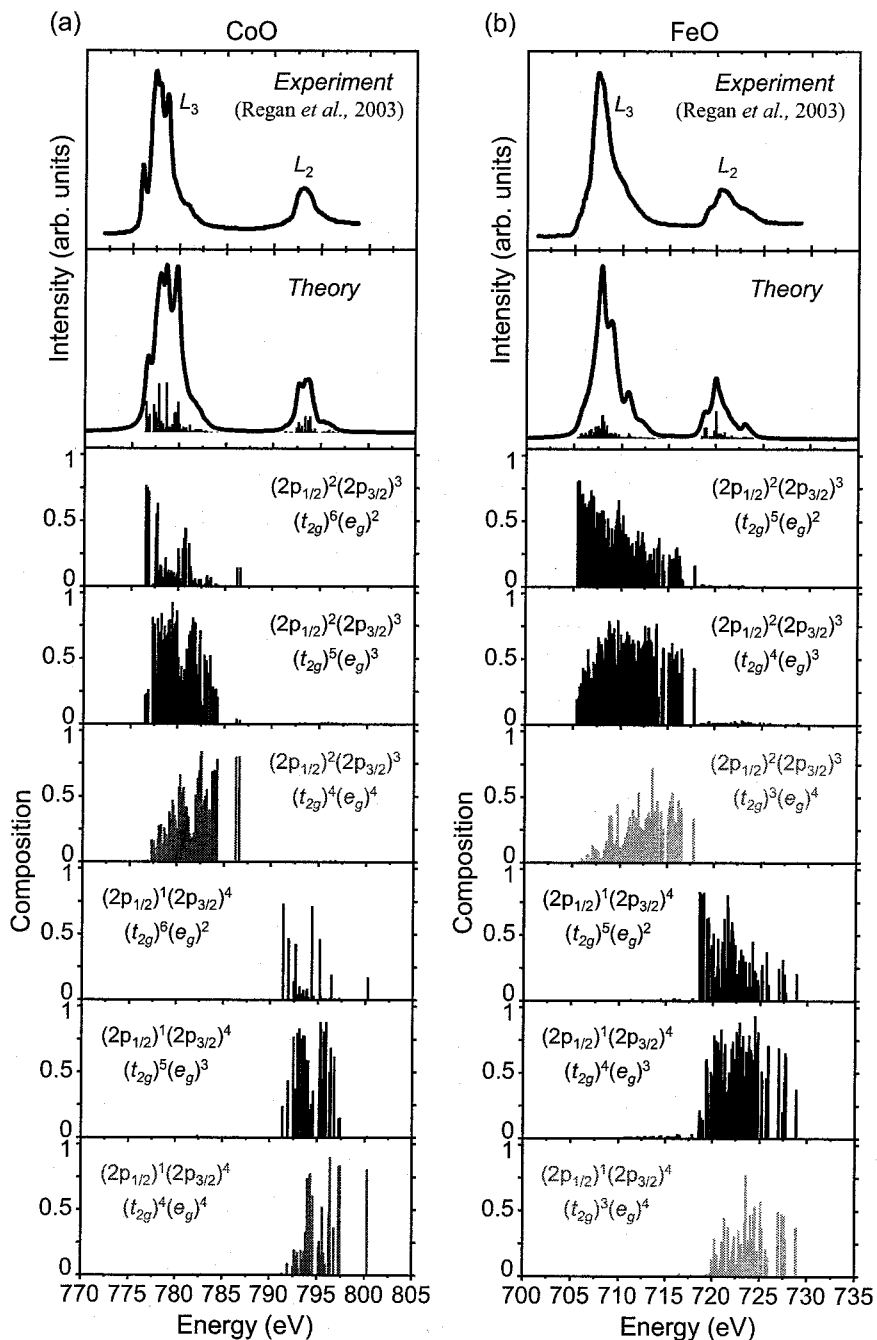
Figure 6.1: Theoretical TM $L_{2,3}$-edge NEXAFS of (a) CoO and (b) FeO compared with experimental spectra adapted with permission from Ref. [19] (Copyrighted (2006) American Physical Society). Solid bars in the upper panel show the oscillator strengths for the many-electron eigenstates. The following panels show the composition of final configurations for the many-electron eigenstates. The transitions to the final configurations drawn in light gray lines have little contribution to the oscillator strength of $L_{2,3}$-edge NEXAFS.
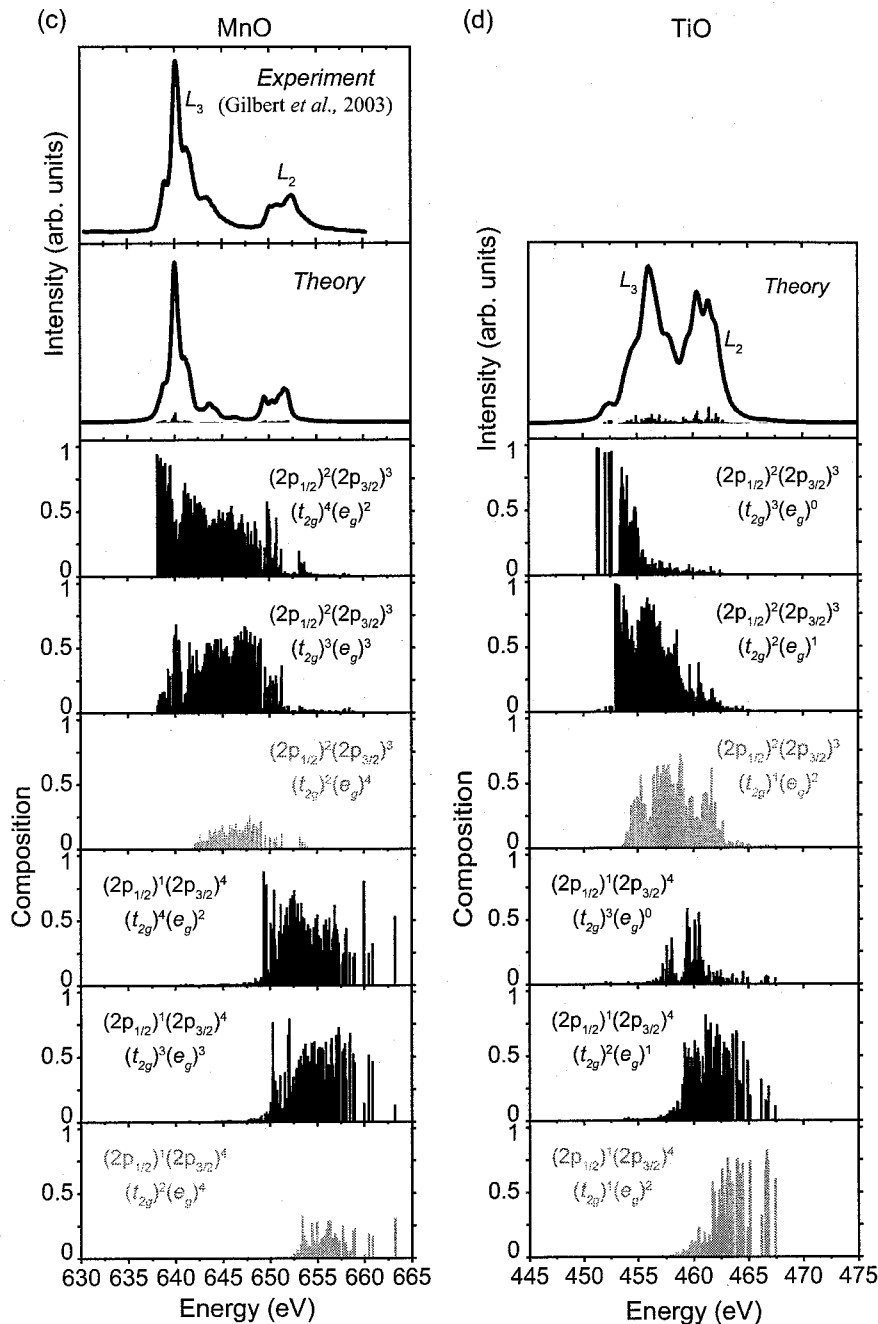
Figure 6.2: Theoretical TM $L_{2,3}$-edge NEXAFS of (c) MnO and (d) TiO. Experimental Mn $L_{2,3}$-edge NEXAFS of MnO, reprinted in part with permission from Ref. [20] (Copyrighted (2007) American Chemical Society), is shown for comparison. Solid bars in the upper panel show the oscillator strengths for the many-electron eigenstates. The following panels show the composition of final configurations for the many-electron eigenstates. The transitions to the final configurations drawn in gray lines have little contribution to the oscillator strength of $L_{2,3}$-edge NEXAFS.
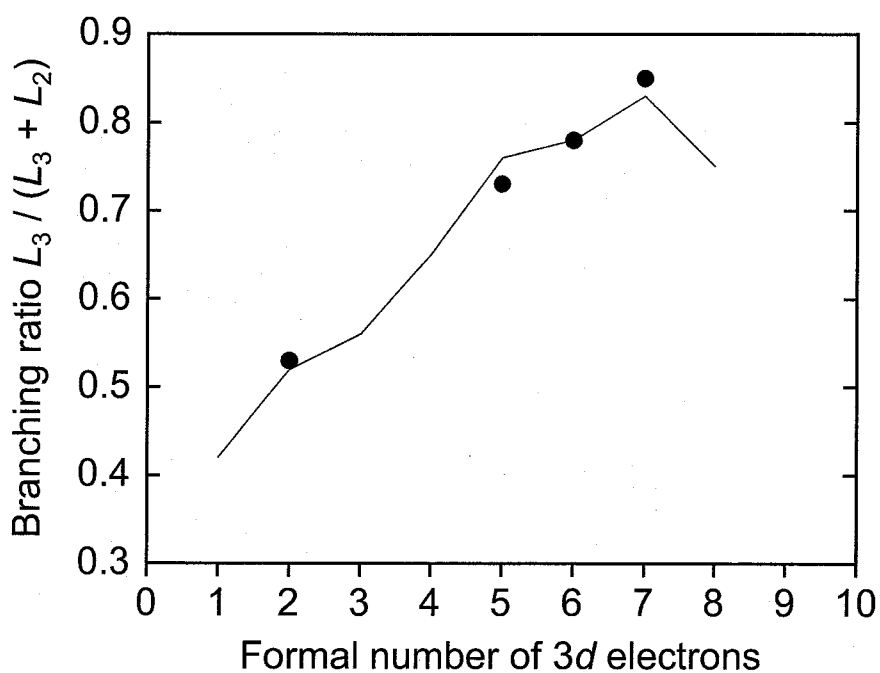
Figure 6.3: Branching ratio, $L_3/(L_3 + L_2)$, against the formal number of $3d$ electrons. The calculated values are shown with full circles. Solid line shows the theoretical branching ratio by a crystal-field atomic multiplet program for high spin state reported in literature [4].

6.3.2 Effects of Breit Interactions on $L_{2,3}$-edge NEXAFS

In order to directly observe the effects of Breit interactions on spectral shape, we have perform CI calculations based on Dirac-Coulomb Hamiltonian (DC) and have calculated TM $L_{2,3}$-edge NEXAFS of those four TM mono-oxides. Results are summarized in Fig. 6.4. Experimental and theoretical spectra based on Dirac-Coulomb-Breit Hamiltonian (DCB) shown in Fig. 6.4 are the same as Fig. 6.1 and 6.2. Theoretical spectra are shifted to align the main peak of L_3-edge in experimental spectra, except for TiO. Two theoretical spectra of CoO show the almost same shapes when comparing L_3-edge and L_2-edge individually. There are little difference of branching ratio. Clear difference can be found in the L_3-L_2 transition energy difference. Co L_2-edge is located on relatively higher energy region when using Dirac-Coulomb Hamiltonian. The same is true for FeO and MnO. For TiO situation is slightly different. The energy separation between Ti L_3-edge and L_2-edge also decreases by including Breit term, which leads to the larger overlap between L_3-edge and L_2-edge region. As a result, the spectral shape by DCB differs from that by DC and branching ratio become larger in DCB result. Comparing with experimental spectra, DCB results slightly underestimate the L_3-L_2 energy separation in FeO and MnO, that will be discussed at the end of this section.

The contribution of Breit interaction term on many-electron eigenvalue can be evaluated by

$$E_k^{\mathrm{Breit}} = \left\langle \Psi_k \left| \sum_{i=1}^{n} \sum_{j<i} B(i,j) \right| \Psi_k \right\rangle \tag{6.2}$$

where Ψ_k is k th many-electron wave function and $B(i,j)$ is Breit interaction operator. The contribution of Coulomb interaction term on k th many-electron eigenvalue E_k^{Coulomb} can be evaluated by similar expression by replacing $B(i,j)$ to $1/r_{ij}$ in (6.2). Table 6.3 summarizes E_i^{Coulomb} and E_i^{Breit} value of TMO$_6^{m-}$ clusters corresponding to initial state of TM $L_{2,3}$-edge NEXAFS. As can be seen, both Coulomb and Breit term decreases with the decrease of atomic number of TM. Breit interaction term has positive contribution to many-electron eigenvalue as well as Coulomb interaction term, but the magnitude is about $10^{-4}(\sim \alpha^2)$ times of Coulomb interaction.

Similar evaluation have made for many-electron eigenstates corresponding to final states of $L_{2,3}$-edge NEXAFS. Fig. 6.5 and 6.6 show the difference of Coulomb and Breit interaction energy between the initial and final states of TM $L_{2,3}$-edge NEXAFS spectra of four TM mono-oxides,
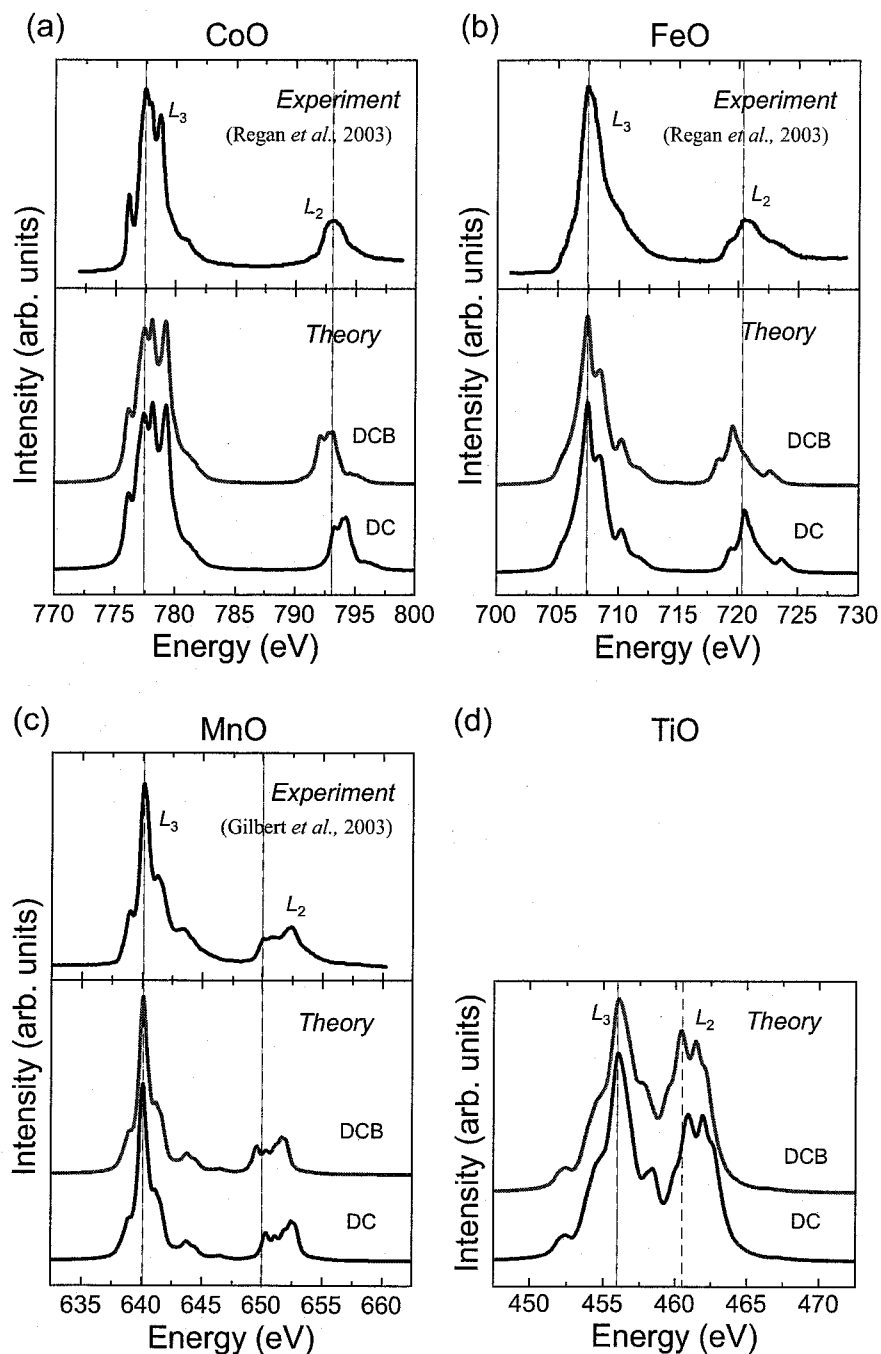
Figure 6.4: Theoretical cation $L_{2,3}$-edge NEXAFS of (a) CoO, (b) FeO, (c) MnO and (d) TiO, calculated by all electron CI using Dirac-Coulomb (DC) Hamiltonian and Dirac-Coulomb-Breit (DCB) Hamiltonian. Experimental spectra adapted with permission from Ref. [19] (Copyrighted (2006) American Physical Society) and Ref. [20] (Copyrighted (2007) American Chemical Society) are also shown for comparison except for TiO.
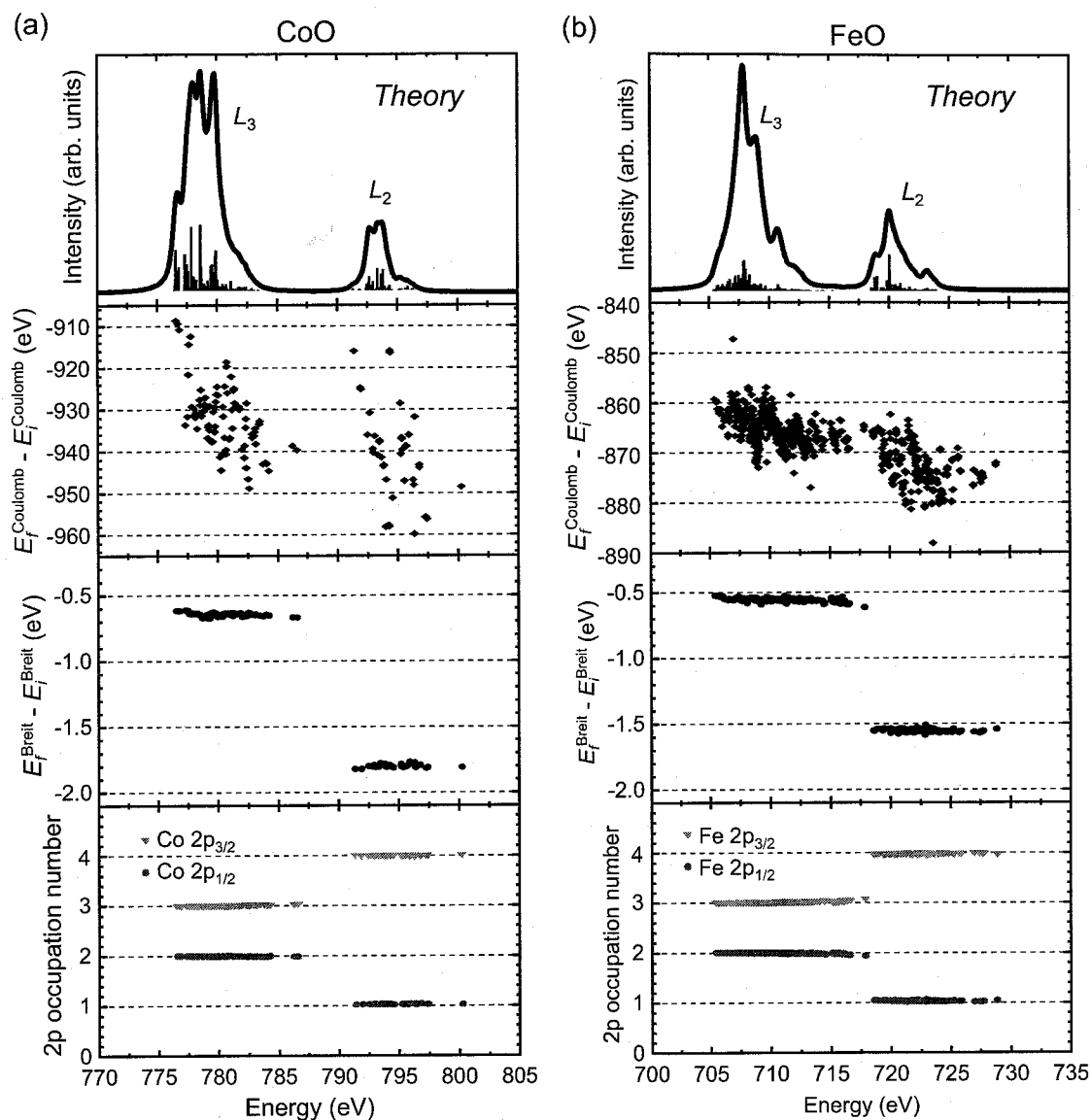
Figure 6.5: (upper) TM $L_{2,3}$-edge NEXAFS of (a) CoO and (b) FeO. (2nd upper) Difference of Coulomb interaction energy between initial and final states of TM $L_{2,3}$-edge NEXAFS ($E_f^{\text{Coulomb}} - E_i^{\text{Coulomb}}$). (2nd lower) Difference of Breit interaction energy between initial and final states of TM $L_{2,3}$-edge NEXAFS ($E_f^{\text{Breit}} - E_i^{\text{Breit}}$). (lower) Expectation values of occupation number of TM-$2p_{1/2}$ and TM-$2p_{3/2}$ orbitals at the final states of TM $L_{2,3}$-edge NEXAFS.
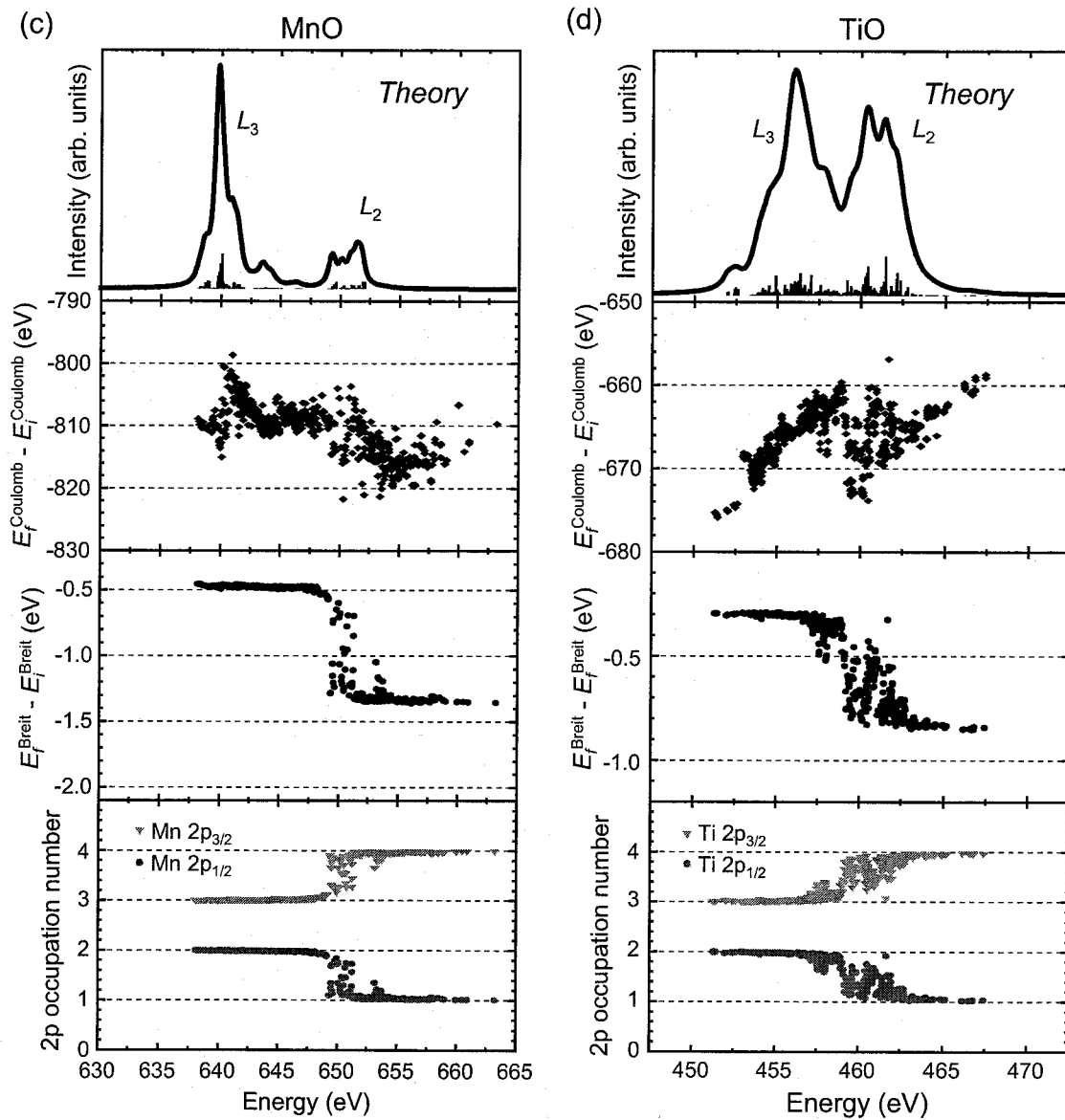
Figure 6.6: Same as Fig. 6.5 but for (c) MnO and (d) TiO.

		E_i^{Coulomb} (eV)	E_i^{Breit} (eV)
CoO	(d^7)	37171.66	7.22
FeO	(d^6)	35186.34	6.30
MnO	(d^5)	33099.54	5.46
TiO	(d^2)	29583.02	3.47

Table 6.3: Contribution of Coulomb and Breit interaction term to many-electron eigenvalue of TMO_6^{m-} cluster corresponding to initial state of TM $L_{2,3}$-edge NEXAFS

i.e., $E_f^{\text{Coulomb}} - E_i^{\text{Coulomb}}$ and $E_f^{\text{Breit}} - E_i^{\text{Breit}}$, compared with theoretical spectra. These diagrams mean the contribution of Coulomb interactions and Breit interactions to transition energy of $L_{2,3}$-edge NEXAFS. Wide scattering of Coulomb interaction can be found in all compounds, which can be ascribed to the strong electronic correlation among TM-$2p$ and $3d$ electrons and result in the multiplet structures on $L_{2,3}$-edge spectra. Contrary, the Breit interaction energy have almost same value in L_3-edge region or in L_2-edge region individually in CoO and FeO. The Breit energy is 1.2 eV and 1.0 eV smaller in L_2-edge than L_3-edge for CoO and FeO, respectively, which explains the decrease of L_3-L_2 energy separation in NEXAFS spectra with little modification of L_3, L_2 spectral shapes in Fig. 6.1. In MnO, $E_f^{\text{Breit}} - E_i^{\text{Breit}}$ values tend to gradually decrease around 650 eV, where overlap between L_3-edge and L_2-edge exist. The same tendency can be found in the energy range between 455 to 465 eV in TiO. The maximum difference of $E_f^{\text{Breit}} - E_i^{\text{Breit}}$ is 0.9 and 0.6 eV for MnO and TiO, which corresponds to the decrease of L_3-L_2 energy separation in Fig. 6.2.

Such behavior of Breit energy can be explained by the occupation number of TM-$2p$ orbitals. The expectation values of occupation number of i th orbital at k th many-electron eigenstate can be evaluated as

$$\left\langle \Psi_k \left| a_i^\dagger a_i \right| \Psi_k \right\rangle = \sum_p \sum_q C_{kp}^* C_{kq} \left\langle \Phi_p \left| a_i^\dagger a_i \right| \Phi_q \right\rangle \tag{6.3}$$

where Φ_p is p th Slater determinant and $a_i^\dagger$ (a_i) are creation (annihilation) operator acting on i th orbital. The bottom panel of Fig. 6.5 and 6.6 shows the expectation values of occupation number of TM-$2p_{1/2}$ and $2p_{3/2}$ orbitals at final states of $L_{2,3}$-edge spectra. The direct correlation can be found between $E_f^{\text{Breit}} - E_i^{\text{Breit}}$ values and the occupation number of TM-$2p_{1/2}$ $(2p_{3/2})$, which

clearly indicate that only Breit interactions among TM-$2p$ electrons affect the relative positions of L_3 and L_2 peaks. In other words, the Breit interactions between TM-$2p$ and $3d$ electrons and among TM-$3d$ electrons are negligibly small in TM $L_{2,3}$-edge NEXAFS of $3d$ TM oxides.

Now, we would like to mention about the small underestimation of L_3-L_2 energy separation in theoretical spectra. This may be ascribed to the omission of electron-electron interactions higher than α^3 and the use of small clusters in the present calculations, which needs to be clarified in the future. Currently, calculations with larger clusters including higher order perturbations are prohibitively expensive.

6.4   Conclusions

All electron relativistic configuration interaction calculations of TM $L_{2,3}$-edge NEXAFS of CoO, FeO, MnO and TiO have been made based on 'no-pair' Dirac-Coulomb-Breit Hamiltonian. The effects of Breit interaction term on TM $L_{2,3}$-edge spectra have been discussed. Major results of this paper can be summarized as follows:

1. Theoretical spectra for MnO, FeO and CoO satisfactory reproduced experimental spectra. Although experimental spectrum for TiO is not available in literature to the authors' best knowledge, we can expect that the agreement for TiO is excellent as well.

2. Initial states of four compounds were described by a linear combination of multiple Slater determinants. Dominant initial configurations for four compounds are "high spin" ones, which is consistent to experimental data. However, the second largest contribution for the initial state of CoO was found to be as large as 12.1%, which means that the one-electron scheme leads to a significant error even for the initial state (Table 6.2).

3. Final states were classified into a few configurations. Significant overlaps in different configurations prevented us from peak assignments according to their configurations. Subpeaks originate entirely from multiplet effects in all of four compounds (Fig. 6.1 and 6.2).

4. The branching ratio increases with the atomic number of TM. The trend agrees to that by

van der Laan and Thole [4] obtained by an atomic multiplet program for an isolated ion embedded in the crystal field of octahedral symmetry (Fig. 6.3).

5. Breit interaction term decreases the L_3-L_2 energy separation of TM $L_{2,3}$-edge NEXAFS with little modification of L_3, L_2 spectral shapes in CoO, FeO and MnO. In TiO, the overlap between L_3, L_2 peaks enlarged with small changes in spectral shape and branching ratio (Fig. 6.4).

6. Breit interactions have positive contribution to the many-electron eigenvalues as well as Coulomb interactions. The magnitudes of Breit interactions energy is 4 th order smaller than that of Coulomb interactions (Table 6.3).

7. Wide range scattering of Coulomb interactions energy is found at the final states of TM $L_{2,3}$-edge NEXAFS that leads to the multiplet structures in $L_{2,3}$-edge spectra. On the other hand, Breit interactions energy have almost unique value correspond to L_3 and L_2 peaks, respectively, except the energy region where overlaps between L_3 and L_2 peaks exist. The Breit interactions energy is larger in L_3-edge than L_2-ege peaks which result in the decrease of L_3-L_2 energy separation (Fig. 6.5 and 6.6).

8. Direct correlation between Breit interaction energy and the occupation number of TM-$2p_{1/2}$ or TM-$2p_{3/2}$ orbitals, which clearly indicate only the Breit interactions among core $2p$ electrons affect the $L_{2,3}$-edge spectra of $3d$ TM oxides (Fig. 6.5 and 6.6).

References

[1] D. H. Pearson, B. Fultz, and C. C. Ahn, Appl. Phys. Lett. **53**, 1405 (1988).

[2] B. T. Thole and G. van der Laan, Phys. Rev. B **38**, 3158 (1988).

[3] J. H. Paterson and O. L. Krivanek, Ultramicroscopy **32**, 319 (1990).

[4] G. van der Laan and B. T. Thole, Phys. Rev. B **43**, 13401 (1991).

[5] H. Kurata and C. Colliex, Phys. Rev. B **48**, 2102 (1993).

[6] M. Koshino, H. Kurata, S. Isoda, and T. Kobayashi, Micron **31**, 373 (2000).

[7] G. Breit, Phys. Rev. **34**, 375 (1929).

[8] G. Breit, Phys. Rev. **39**, 616 (1932).

[9] J. Sucher, Phys. Rev. A **22**, 348 (1980).

[10] M. H. Mittleman, Phys. Rev. A **24**, 1167 (1981).

[11] J. A. Gaunt, Proc. R. Soc. London Ser. A **122**, 513 (1929).

[12] J. B. Mann and W. R. Johnson, Phys. Rev. A **4**, 41 (1971).

[13] M. H. Chen, B. Crasemann, and H. Mark, Phys. Rev. A **25**, 391 (1982).

[14] M. H. Chen, K. T. Cheng, and W. R. Johnson, Phys. Rev. A **47**, 3692 (1993).

[15] Y. Ishikawa, H. M. Quiney, and G. L. Malli, Phys. Rev. A **43**, 3270 (1991).

[16] H. M. Evjen, Phys. Rev. **39**, 675 (1932).

[17] A. Rósen, D. E. Ellis, H. Adachi, and F. W. Averill, J. Chem. Phys. **65**, 3629 (1976).

[18] J. Olsen, B. O. Roos, P. Jørgensen, and H. J. A. Jensen, J. Chem. Phys. **89**, 2185 (1988).

[19] T. J. Regan, H. Ohldag, C. Stamm, F. Nolting, J. Lüning, J. Stöhr, and R. L. White, Phys. Rev. B **64**, 214422 (2001).

[20] B. Gilbert, B. H. Frazer, A. Belz, P. G. Conrad, K. H. Nealson, D. Haskel, J. C. Lang, G. Srajer, and G. De Stasio, J. Phys. Chem. A **107**, 2839 (2003).

Chapter 7

Summary and Conclusions

In this thesis, first principles many-electron methods with various level of approximations have been developed and applied to compute $3d$ transition metal (TM) $L_{2,3}$-edge NEXAFS / ELNES. Chemical states and local structures of TM atoms in various $3d$ transition metal compounds were investigated by combining experiments and those theoretical calculations. The origin of subpeaks appearing in experimental spectra were discussed in theoretical approach.

In chapter 3 and 4, the hybrid method of density functional theory (DFT) and configuration interaction (CI) method have been applied to calculate TM $L_{2,3}$-edge NEXAFS. Relativistic molecular orbitals calculations were carried out by solving Dirac equations with density functional theory. CI calculations were made using the molecular orbitals mainly composed of TM-$2p$ and TM-$3d$ orbitals. The contributions of O-$2p$ orbitals through covalency can be automatically included without any other scheme by using molecular orbitals instead of atomic orbitals. This is very important for transition-metal oxides with high formal charges.

In chapter 3. Fe-$L_{2,3}$ XANES of FeO (Fe(II)), LaFeO$_3$ (Fe(III)) and SrFeO$_3$ (Fe(IV)) have been calculated in order to demonstrate the usefulness of DFT-CI method for the chemical state analysis. Experimental NEXAFS spectra of three compounds were satisfactorily reproduced by the theoretical spectra obtained for (FeO$_6$)$^{m-}$ clusters in octahedral symmetry. Chemical shifts between compounds were quantitatively reproduced as well. Configuration analysis of CI was systematically made in order to analyze the origin of differences in spectral shapes.

In chapter 4, this method was applied to the Ni $L_{2,3}$ NEXAFS of three kinds of nickel oxides,

i.e., NiO, $LiNiO_2$, and NiO_2 (Li-extracted $LiNiO_2$). $LiNiO_2$ have been studied as a cathode material of lithium batteries, but the change of electronic structure of Ni ions by insertion/extraction of lithium ion has been not fully understood. Model clusters of NiO_6^{m-} were used, where m is taken to be 10, 9, and 8 for NiO, $LiNiO_2$, and NiO_2, respectively. Theoretical NEXAFS and ELNES within the electric dipole approximation were obtained by calculating oscillator strengths from several initial states with different spin configuration to all of final states. Depending on the choice of initial state configuration, dipole transition probability is quite different because selection rule completely changes. The origin of satellite peaks in these spectra was also discussed through configuration analysis. Experimental ELNES for the three compounds were satisfactorily reproduced by the present calculations, which unambiguously show that Ni atoms are Ni(III) with a low-spin state in $LiNiO_2$, and Ni(IV) with a low-spin state in NiO_2.

In chapter 5, we have investigated the local environment of Mn atoms doped in semiconductors using Mn $L_{2,3}$-edge NEXAFS, which is essential to understand mechanism of ferromagnetism in diluted magnetic semiconductors (DMS). First, we have examined Mn $L_{2,3}$-edge NEXAFS of ZnO:Mn samples that have already been well characterized in our previous Mn K-edge NEXAFS study. First principles many-electron calculations of Mn $L_{2,3}$-edge NEXAFS in MnO (CN = 6) and ZnO:Mn (CN = 4) were made by two different level of approximations, i.e., "CI(Mn$2p3d$)+LDA" approach which was the same approach used in chapter 3 and 4, and "CI(Mn$2p3d$-O$2p$)+LDA" approach in which the dimension of Slater determinants was increased to include O-$2p$ orbitals. Better agreement between experimental and theoretical spectra were obtained by latter approach. Mn(II) with different coordination numbers, i.e., CN = 4 and 6, can be clearly distinguished by using this method. Judging from the good agreement of experimental and theoretical spectra, Mn atoms in ZnO:5at.%Mn samples are substituting Zn site of wurtzite ZnO, which is consistent with the conclusion in our previous study by Mn K-edge NEXAFS. The angular dependence of Mn $L_{2,3}$-edge NEXAFS of ZnO:Mn thin film was also investigated. Although ZnO forms hexagonal crystal, little dependence on crystallographic orientation was shown by both experiment and theoretical calculations. This is contrary to the large dependence in the Mn K-edge NEXAFS. Using the new theoretical approach with predictive performance, we have investigated the local environment of Mn atoms in GaN:Mn thin films which show ferromagnetism at room temperature. Mn

$L_{2,3}$-edge NEXAFS of GaN:Mn thin films were systematically measured. No spectral change can be detected up to 8.2% Mn concentration. Many-electron calculations were performed using two different models which a Mn(II) and a Mn(III) atom substituting a Ga site of GaN. MnN_4^{10-} and MnN_4^{9-} cluster model were taken corresponding to Mn(II) and Mn(III), respectively. Comparison of experimental and theoretical spectra of GaN:Mn showed that majority of Mn atoms are divalent and substitutionally located at Ga site of GaN. A small but clear difference between experimental spectra of ZnO:Mn and GaN:Mn was recognized at the small satellite peak on L_3-edge. The agreement between experimental and theoretical spectra of GaN:Mn is better when 15% of Mn atoms are assumed to be in the trivalent state. This result suggests the coexistence of Mn(II)/Mn(III) in GaN. The same analysis was carried out for Mn doped Ga_2O_3 thin film. This sample has a defective spinel structure and show ferromagnetism at room temperature. The peak position of experimental Mn $L_{2,3}$-edge NEXAFS of this sample was the same as those of MnO and ZnO:Mn, which implied that Mn(II) was dominant. Mn $L_{2,3}$-edge NEXAFS were calculated using MnO_4^{6-} and MnO_6^{10-}, which correspond to Mn(II) with CN=4 and CN=6. Experimental and theoretical spectra revealed that most of Mn(II) atoms are located on the four-fold coordination site of oxygen. This result is consistent the fact that Mn atoms prefers tetrahedral site in $MnGa_2O_4$ spinel structure. By using TM $L_{2,3}$-edge NEXAFS in conjunction with present non-empirical many-electron calculations, one can obtain the direct information of TM-$3d$ state. Such type of analysis must be an important and powerful tool to identify the physical and chemical properties of transition metal atoms DMSs.

In chapter 6, all electron configuration interaction method have been developed and applied to TM $L_{2,3}$-edge NEXAFS of four kind of TM mono-oxides with rocksalt structure, i.e, CoO, FeO, MnO and TiO. Electronic correlations among all electrons in TMO_6 clusters were rigorously calculated. Problems related to the approximated exchange-correlation potential can be avoided by this method. The Breit interaction, which is the first relativistic correction to the Coulomb interaction derived from quantum electrodynamics (QED), was included to obtain the more accurate description of relativistic many-electron Hamiltonian. Theoretical spectra for MnO, FeO and CoO satisfactory reproduced experimental spectra. Configuration analysis for initial stats of TM $L_{2,3}$-edge revealed that dominant initial configurations for four compounds are "high spin" ones, which

is consistent to experimental data. In CoO, the second largest contribution for the initial state as large as 12.1%, which indicates that the one-electron scheme leads to a significant error even for the initial state. Significant overlaps in different configurations were found on final stats. We cannot assign experimental peaks according to the electronic configuration. Subpeaks originate entirely from multiplet effects in all of four compounds. The branching ratio increases with the atomic number of TM. The trend agrees to that by van der Laan and Thole obtained by crystal field multiplet calculations under octahedral symmetry.

The effects of Breit interactions on TM $L_{2,3}$-edge NEXAFS spectra were discussed. Breit interactions have positive contribution to the many-electron eigenvalues as well as Coulomb interactions, but its magnitude is 4 th order smaller. Reflecting the strong multiplet effects on TM $L_{2,3}$-edge NEXAFS, large scattering of Coulomb interactions energy were found at final states, while Breit interactions energy had almost unique value correspond to L_3 and L_2 peaks, respectively. This energy is larger in L_3-edge than L_2-ege peaks which result in the decrease of L_3-L_2 energy separation. Breit interactions energy gradually decreased where overlaps between L_3 and L_2 peaks exist in MnO and TiO. Direct correlation between Breit interaction energy and the occupation number of TM-$2p_{1/2}$ or TM-$2p_{3/2}$ orbitals, that clearly indicate only the Breit interactions among core $2p$ electrons affect the $L_{2,3}$-edge spectra of $3d$ TM oxides. The shapes of L_3 and L_2 peaks individually were hardly affected by the inclusion of Breit term in CoO, FeO and MnO. In TiO, the overlap between L_3, L_2 peaks enlarged with small changes in spectral shape and branching ratio. This result suggests that the relativistic correlation of electron-electron interactions should be important to discuss the detailed structure of TM $L_{2,3}$-edge spectra especially for light $3d$ transition metal compounds.

These studies in this thesis confirmed that the new theoretical method has predictive performance of various TM $L_{2,3}$-edge NEXAFS without any empirical parameters. This method can be used for the TM ions coordinated by ligand ions of arbitrary symmetry in general. This is in contrast to an atomic multiplet program which can be practically used for high symmetry systems and requires many fitting parameters to reproduce experimental spectra. NEXAFS/ELNES from probe atoms in unusual environment, such as surface adsorbants, dopants/segregants at grain boundary

etc, can be also analyzed by present method. We expect that the combination of experiment and theoretical calculations by the present method is an important and powerful characterization tool of transition metal atoms, and helpful for the development of new materials.

Acknowledgement